

# Compressive Holography

by

Se Hoon Lim

Department of Electrical and Computer Engineering  
Duke University

Date: \_\_\_\_\_

Approved:

---

David J. Brady, Supervisor

---

David R. Smith

---

Jungsang Kim

---

Rebecca Willett

---

Adam Wax

Dissertation submitted in partial fulfillment of the requirements for the degree of  
Doctor of Philosophy in the Department of Electrical and Computer Engineering  
in the Graduate School of Duke University  
2012

## ABSTRACT

Compressive Holography

by

Se Hoon Lim

Department of Electrical and Computer Engineering  
Duke University

Date: \_\_\_\_\_

Approved:

---

David J. Brady, Supervisor

---

David R. Smith

---

Jungsang Kim

---

Rebecca Willett

---

Adam Wax

An abstract of a dissertation submitted in partial fulfillment of the requirements for  
the degree of Doctor of Philosophy in the Department of Electrical and Computer  
Engineering  
in the Graduate School of Duke University  
2012

Copyright © 2012 by Se Hoon Lim  
All rights reserved except the rights granted by the  
Creative Commons Attribution-Noncommercial Licence

# Abstract

Compressive holography estimates images from incomplete data by using sparsity priors. Compressive holography combines digital holography and compressive sensing. Digital holography consists of computational image estimation from data captured by an electronic focal plane array. Compressive sensing enables accurate data reconstruction by prior knowledge on desired signal. Computational and optical co-design optimally supports compressive holography in the joint computational and optical domain. This dissertation explores two examples of compressive holography : estimation of 3D tomographic images from 2D data and estimation of images from under sampled apertures.

Compressive holography achieves single shot holographic tomography using de-compressive inference. In general, 3D image reconstruction suffers from under-determined measurements with a 2D detector. Specifically, single shot holographic tomography shows the uniqueness problem in the axial direction because the inversion is ill-posed. Compressive sensing alleviates the ill-posed problem by enforcing some sparsity constraints. Holographic tomography is applied for video-rate microscopic imaging and diffuse object imaging. In diffuse object imaging, sparsity priors are not valid in coherent image basis due to speckle. So incoherent image estimation is designed to hold the sparsity in incoherent image basis by support of multiple speckle realizations.

High pixel count holography achieves high resolution and wide field-of-view imag-

ing. Coherent aperture synthesis can be one method to increase the aperture size of a detector. Scanning-based synthetic aperture confronts a multivariable global optimization problem due to time-space measurement errors. A hierarchical estimation strategy divides the global problem into multiple local problems with support of computational and optical co-design. Compressive sparse aperture holography can be another method. Compressive sparse sampling collects most of significant field information with a small fill factor because object scattered fields are locally redundant. Incoherent image estimation is adopted for the expanded modulation transfer function and compressive reconstruction.

To my family and friends.

# Contents

<b>Abstract</b>	<b>iv</b>
<b>List of Tables</b>	<b>ix</b>
<b>List of Figures</b>	<b>x</b>
<b>Acknowledgements</b>	<b>xii</b>
<b>1 Overview</b>	<b>1</b>
<b>2 Compressive Holography</b>	<b>4</b>
2.1 Introduction . . . . .	4
2.2 The Procedure of Compressive Holography . . . . .	7
2.3 Field Propagation . . . . .	8
2.4 Compressive sensing . . . . .	13
<b>3 Holographic Tomography</b>	<b>16</b>
3.1 Computational Design . . . . .	16
3.2 Sampling and Processing w/ Simulation . . . . .	20
3.3 Dandelion Project . . . . .	23
3.3.1 Optical design and experimental results . . . . .	23
3.4 Micro-Bead Project . . . . .	27
3.5 Water Flea Project . . . . .	30
3.5.1 Microscopic holographic tomography . . . . .	30
3.5.2 Optical design and experimental results . . . . .	32

<b>4 Holographic Tomography of Diffuse Objects</b>	<b>38</b>
4.1 Computational Design . . . . .	38
4.2 Sampling and Processing w/ Simulation . . . . .	42
4.3 Diffuse Object Project . . . . .	45
4.3.1 Optical design and experimental results . . . . .	45
<b>5 High Pixel Count Holography</b>	<b>52</b>
5.1 Scanning-based Synthetic Aperture Holography . . . . .	52
5.1.1 Introduction . . . . .	52
5.1.2 Problem formulation . . . . .	55
5.1.3 Computational design . . . . .	59
5.1.4 Optical design . . . . .	64
5.1.5 Processes and results . . . . .	69
5.2 Sparse Aperture Holography . . . . .	76
5.2.1 Introduction . . . . .	76
5.2.2 The feasibility of sparse aperture holography . . . . .	78
5.2.3 Sampling and processing w/ simulation . . . . .	79
<b>6 Conclusions</b>	<b>83</b>
6.1 Summary of Results . . . . .	84
6.2 Future of Compressive Holography . . . . .	85
<b>A Aliasing Analysis</b>	<b>87</b>
<b>B Resolution Analysis</b>	<b>89</b>
<b>C Matlab Codes</b>	<b>91</b>
<b>Bibliography</b>	<b>106</b>
<b>Biography</b>	<b>111</b>

# List of Tables

5.1	The estimated parameters of the detector registration errors and the reference field errors for the WA hologram synthesis. . . . .	75
5.2	The Chebychev coefficients for the reference field discrepancy. . . . .	76

# List of Figures

2.1	Incoherent imaging vs. coherent imaging . . . . .	5
2.2	Comparison of field propagations . . . . .	13
2.3	Illustration of compressive sensing . . . . .	15
3.1	Gabor hologram geometry. . . . .	17
3.2	Simulations for holographic tomography . . . . .	21
3.3	Experimental apparatus. . . . .	23
3.4	Dandelion parachutes reconstruction . . . . .	25
3.5	Microscopic object setup . . . . .	27
3.6	Multiple beads reconstruction . . . . .	28
3.7	Transverse slices of tomographic reconstruction . . . . .	29
3.8	A schematic of the compressive holographic microscope. . . . .	30
3.9	Experimental setup . . . . .	32
3.10	Raw image of a Gabor hologram. . . . .	33
3.11	A comparison of reconstructions at chosen axial positions . . . . .	34
3.12	A comparison of the magnified tails . . . . .	35
3.13	A 3D visualization of the compressive holography reconstruction. . . . .	37
3.14	A 2D representation of 3D datacube using the range colormap . . . . .	37
4.1	Incoherent image estimation . . . . .	41
4.2	Simulations for diffuse object tomography . . . . .	44
4.3	Experimental setup . . . . .	46

4.4	Conventional reconstruction . . . . .	47
4.5	Compressive reconstruction . . . . .	48
4.6	Compressive reconstruction with regularization parameters . . . . .	49
4.7	Ladybug experiment . . . . .	50
5.1	Schematic for image-based synthetic aperture holography . . . . .	55
5.2	Flow chart of the error estimation processes . . . . .	60
5.3	Experimental setup . . . . .	65
5.4	Piston phase correlation in two distant cameras . . . . .	68
5.5	Evolution of estimation effects on the guiding features image . . . . .	70
5.6	Resolution improvement to the number of hologram patches in the guiding features . . . . .	72
5.7	Full FOV image with $63.4 \times 63.4$ mm aperture . . . . .	73
5.8	The images of the AF targets in the depth imaging experiment . . . . .	74
5.9	The image of the CPU chip . . . . .	75
5.10	The monitored piston phase variation of scanned 144 hologram patches. . . . .	76
5.11	Coherent and incoherent bandpasses in sparse aperture design . . . . .	77
5.12	Feasibility of sparse aperture holography . . . . .	78
5.13	Point-based sparse aperture holography . . . . .	81
5.14	Patch-based sparse aperture holography . . . . .	82
B.1	Resolution and bandwidth . . . . .	90

# Acknowledgements

I have many people to thank for both the opportunity to study at Duke and the great experiences I have had here. My family has been supportive of my endeavors over the years. While at Duke it has been a pleasure to work with Dr. David J. Brady, whose guidance and creative ideas have been very crucial in my development as an independent researcher. Some other colleagues at Duke who I have learned much from include Kerkil Choi, Joonku Hahn, and Dan Marks. Our discussions and lunch meetings kept me from staying back. The many other members of the DISP group have made it a great group to be a part of – Steve Feller, Nathan Hagens, Renu John, Leah Goldsmith, Kalyani Krishnamurthy, Amarpreet Chawla, Scott Maccain, Mohan Shankar, Andrew Portnoy, Nan Zheng, Christy Fernandez, Ashwin Wagadarikar, David Kittle, Alexander Mrozack, Ken MacCabe, Kai Hui, Evan Chen, Andrew Holgrem, Alireza Samani, Tsung-Han Tsai, and Zhongxi Wang.

# 1

## Overview

This dissertation presents holographic tomography and sparse aperture holography as demonstrations of compressive holography. Compressive holography is supported by computational and optical co-design in solving high dimensional imaging problems. Individual chapters are structured by mathematical forms for computational design, simulations for data sampling and processing, and experiments for optical design and result. To aid understanding, Matlab codes are presented in appendices for the simulation parts.

Compressive holography infers high-resolution object features from a small number of discrete holographic measurements by exploiting the sparseness of the object of interest in an appropriate sparsity basis. Compressive holography may be applied to reconstruct three-dimensional (3D) images from two-dimensional (2D) measurements or to reconstruct 2D images from sparse apertures. Compressive holography combines the previous researches of compressive sensing and digital holography. Chapter 2 introduces the following fundamental ideas on compressive holography : (1) the procedure of compressive holography, (2) digital propagation of holographic fields, and (3) compressive sensing .

Compressive holography then covers as examples 3D tomography from a 2D hologram, diffuse object estimation from diverse speckle realizations, and 2D image reconstruction from a sparse aperture. Holographic tomography differs from radar and other coherent imaging systems only in the need to filter the signal from the reference in isolating the coherent field from irradiance data. Traditionally, this isolation is done by putting the holographic signal on a spatial or temporal sideband [1]. As demonstrated in Chapter 3, however, constrained nonlinear estimators can isolate the holographic image from reference and background from in-line holographic data. The coherent image estimation method is simulated with 3D object reconstruction from 2D holograms. In experiments, two dandelion parachutes in 3D space are tomographically reconstructed from 2D hologram with 8 mm axial resolution and 10.4  $\mu\text{m}$  transverse resolution. In micro-scale imaging, 3D distribution of 1  $\mu\text{m}$  size beads are obtained by using a microscopic objective lens. Without any optical lens, video-rate tomographic image acquisition of two live water fleas is also demonstrated with 60  $\mu\text{m}$  axial resolution and 5.2  $\mu\text{m}$  transverse resolution.

Chapter 4 describes a method that enables decompressive estimation of incoherent images from digital holographic data. Incoherent image estimation is discussed because if the scattering phase is random (e.g. if speckle is present) then holographic images may not be sparse in the conventional compressive sensing sense. However, the underlying scattering amplitude (e.g. the incoherent image) is generally sparse. Tomographic imaging for diffuse objects is simulated with a Matlab code, imposing sparsity constraints on the incoherent image. The computational design is experimentally supported with multiple speckled realizations.

Chapter 5 studies high pixel count holography for wide field-of-view and diffraction-limited resolution imaging. Since digital holography does not rely on an optical lens system, the resolution and the field of view are determined by an aperture size. The resolution and the field of view are inversely and linearly proportional to the aper-

ture size, respectively. This chapter contains two sections describing scanning-based synthetic aperture holography and sparse aperture holography. High pixel count apertures for digital holography may be synthesized by scanning smaller aperture detector arrays. A major challenge in scanned systems is characterization and compensation for registration errors in the detector array position and pitch and for phase instability between the reference and object field. A secondary sensor is designed to monitor phase and image-based registration parameter estimators to demonstrate near diffraction-limited resolution from a 63.4 mm aperture synthesized by scanning a 5.28 mm subaperture over 144 transverse positions.

Plus, Section 5.2 presents sparse aperture holography as an alternative method for high pixel count imaging. Since the incoherent image estimation takes advantage of expanded modulation transfer function (MTF) support, compressive reconstruction mitigates the incomplete measurements of sparse aperture. The feasibility of the sparse aperture approach is tested by using compressive sampling on the scanned synthetic aperture hologram. In simulation, the effect of incoherent image estimation is shown for compressive sparse aperture holography.

# 2

## Compressive Holography

### 2.1 Introduction

Digital holography is the capture of coherent fields scattered from objects on electronic photometric sensors [2]. Holography was originally proposed by Dennis Gabor [3] for lensless imaging process. Holography obtains the phase information of scattered fields by recording interference patterns generated by two coherent beams – an object beam and a reference beam. The hologram of interference patterns contains the phase information in intensity variations, which is known as interferometry [4]. In reconstruction, interferometry produces the relative phase of scattered fields to the reference beam. In hologram recording, digital holography replaced conventional photographic films with electronic sensors. Since the advancement of electronic measurement, wavefront reconstruction is computationally performed in discrete signal domain. The wavefront is reconstructed by propagating the scattered fields in diffraction models. Digital holography is illustratively compared to the incoherent capture in Fig. 2.1. While the incoherent capture needs an optical lens for wavefront reconstruction, digital holography reconstructs the wavefront from the

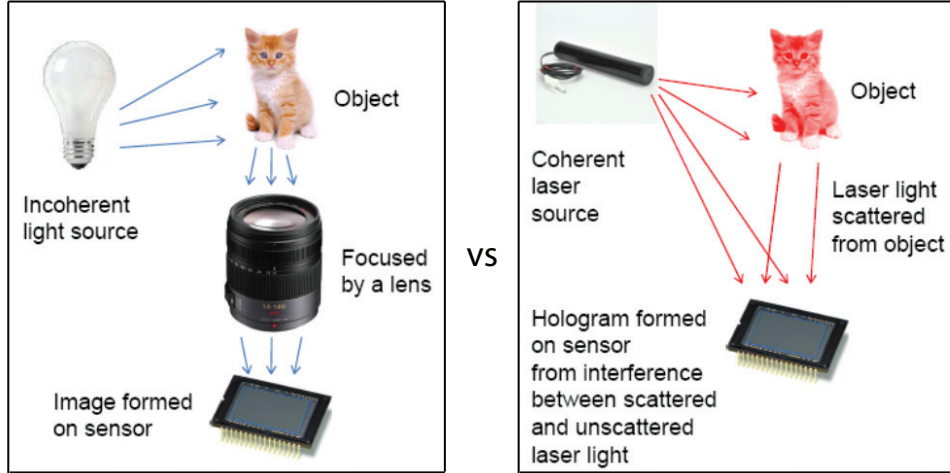


FIGURE 2.1: Incoherent imaging vs. coherent imaging : coherent imaging does not need an optical lens for focal measurement.

phase information of interferometric measurement.

These digitized holograms may yield information about these objects including shape, reflectivity, and acoustic or mechanical deflections. Digital processing allows an almost unlimited flexibility to process sampled holographic data to discern features. Recently, the method of compressive sensing [5, 6] has been developed to determine the complex features of objects using relatively few measurements. Rather than assuming that objects may contain arbitrary features, most of which are unlikely to occur, compressive sensing imposes *a priori* constraints that the object possesses only a small number of a large set of predefined features, and identifies these features from the data. Many objects of interest in holography satisfy such sparsity constraints, including three-dimensional parts/elements which may be largely contiguous and also possess much empty space, and two-dimensional images which may have large contiguous regions. Compressive holography advantageously combines compressive sensing with digital holography so that two-dimensional holograms or sparse aperture holograms may be used to infer object properties that would be otherwise undetermined.

Applying compressive and feature-specific priors to optical imaging is an area of increasingly intensive study. Numerous designs for feature specific [7] and compressive [8] optical imagers have been developed over the past decade. Several studies have extended these approaches to digital holography. Zhang *et al.* used linear [9] and nonlinear [10] inverse algorithms to reconstruct sections of 3D images. Our group has completed several studies of compressive holographic tomography [11, 12], millimeter wave holography [13] and diffuse holography [14]. Denis *et al.* have also applied sparsity constraints in holographic imaging [15]. Fournier *et al.* theoretically estimated single point resolution in compressive holographic tomography [16]. Marim *et al.* decompressively reconstructed a 2D microscopic image with fewer measurements [17, 18]. Rivenson *et al.* suggested variable sub-sampling scheme for compressive Fresnel holography [19], and demonstrated compressive measurement for multiple view projection incoherent holography [20]. Xu *et al.* adopted the compressive holographic tomography technique [11] to filter the object signal in inline coherent anti-Stokes Raman scattering holography [21]. Xu *et al.* effectively reduced the number of measurements in THz imaging [22]. In a broader scope, Coskun *et al.* compressively decoded sparse objects' distribution in lensless wide-field fluorescent imaging [23]. Suzen *et al.* used sparsifying basis to improve reconstructions with under-sampled data in diffuse optical tomography [24]. Given that both computational imaging and compressive sensing are rapidly evolving, it is certain that great advances for these fields are to come.

The common themes of this previous work are first, that image estimation using sparsity priors is useful in holography and second, that co-design of nonlinear estimators with sampling strategies and geometries may yield significant improvements. While these basic themes may be applied to a very wide diversity of holographic systems, the basic advantage that they convey are summarized by the idea that compressive measurement delivers more signal values with fewer measurements. For

this advantage to have value, one must assume a cost or feasibility model that inhibits complete measurement. The simplest such models arise in 3D estimation from 2D data (Chapter 3), in which case complete sampling is not physically possible in a single time step, and 2D or 3D estimation from sparse apertures (Chapter 5), in which case complete sampling is not economically desirable.

## 2.2 The Procedure of Compressive Holography

To apply compressive sensing to digital holography, one must first determine the features in the object that are likely to be present so that compressive inference methods may be applied. The object vector which describes these features to be reconstructed is expressed as a linear sum of a set of overcomplete dictionary vectors. A sparse reconstruction of the object means that only a small number of these dictionary vectors are used for any given reconstruction of an object. Examples of the dictionary vectors include the canonical basis for groups of point-like objects, total variation (TV) constraints for objects with few edges and large uniform regions, wavelet bases, and the Fourier basis. There are restrictions about the “coherence” [25] between the measurements and the object basis that limit the fidelity of the reconstructions, namely, whether or not the correct dictionary elements are inferred to be present in the object vector.

A digital holography setup typically comprises these parts: a source of coherent light such as a laser, an object to test, and an electronic photometric sensor. Light is scattered from the object to test and falls on the sensor plane. Often an interferometer such as a Michelson or Mach-Zehnder setup is used to create a reference beam to be interfered on the sensor. Typical geometries used for digital holography include Gabor in-line holography and Leith-Upatnieks (LU) off-axis holography. Because only the intensity of the interference between the reference and object-scattered fields is measured, there is an ambiguity in the object field often called the conjugate

field or image. The choice of geometry is often dictated by the acceptable ambiguity.

One or more holograms may be acquired, perhaps moving the object or sensor between each acquisition. This data is processed to produce a reconstruction of the object using a given dictionary. Determining which dictionary elements and the magnitudes of their weights is typically achieved by basis pursuit or  $\ell_1$  minimization with a least-squares fit to the data. There are many algorithms for solving basis pursuit and  $\ell_1$  minimization problems. For example, TwIST is applied in much of the work detailed here because of its flexibility and simplicity. To apply these algorithms, a numerical simulation of the hologram formation process is used so that the data may be fit to successive candidate objects. This simulation usually includes a means of digital propagation that models the diffraction of fields through space. Digital holography differs from radar in that the transverse scale of these fields may span  $10^3 - 10^5$  wavelengths. Because of the computation and storage required to propagate wide area fields often encountered in compressive holography, we have included details on this step.

### 2.3 Field Propagation

Digital holography numerically backpropagates the scattered field by using a field propagation model [26]. Because the propagation is performed in discrete domain, the field propagation model must sample the field at a rate to avoid aliasing, yet not overly increase computational and storage costs. In general the propagated object field is given by the Rayleigh-Sommerfeld diffraction formula [4]. Under the paraxial approximation in optics, the object field is simplified to the model of Fresnel approximation method (FAM),

$$E_o(x, y) = \frac{ke^{jkz}}{j2\pi z} e^{j\frac{k}{2z}(x^2+y^2)} \iint dudve^{-j\frac{k}{2z}(2xu+2yv)} E_s(u, v) e^{j\frac{k}{2z}(u^2+v^2)}, \quad (2.1)$$

where spatial coordinates  $(x, y)$  and  $(u, v)$  respectively indicate the object plane and the detector plane. Note that  $k$  is the wavenumber,  $\lambda$  is the wavelength, and  $z$  is the propagation distance in the optical axis.

In the discrete measurement, the pixel resolution  $\delta x$  and the field of view (FOV)  $\Delta x$  are expressed by [27]

$$\delta x = \frac{\lambda z}{N \delta u}, \quad (2.2)$$

$$\Delta x = \frac{\lambda z}{\delta u}, \quad (2.3)$$

where  $N$  is the number of detector pixels.  $\delta x$  and  $\Delta x$  follow the Fourier relationship between the object domain  $x$  and the detection domain  $u$ . They are functions of a scaling factor  $\lambda z$  so the propagation distance  $z$  is a critical parameter to consider for processing design. The computational simplicity of FAM arises in that the FAM uses a single 2D Fourier transform for backpropagation. Note that the validity of FAM is only guaranteed for paraxial imaging.

The angular spectrum method (ASM) has a different analytical derivation without any approximation. The object field  $E_o(u, v)$  is considered as a 2D convolution of the scattered field  $E_s(x, y)$  and a backpropagation kernel. By using the convolution theorem in Fourier analysis, the ASM is

$$E_o(x, y) = \frac{1}{(2\pi)^2} \iint du dv e^{-j(k_u u + k_v v)} E_s(u, v) \iint dk_u dk_v e^{jz\sqrt{k^2 - k_u^2 - k_v^2}} e^{j(k_u x + k_v y)}, \quad (2.4)$$

where the term  $e^{jz\sqrt{k^2 - k_u^2 - k_v^2}}$  is the transfer function that is Fourier transformed from the point spread function [28].

Due to the difference of analytical forms, the ASM has the different pixel resolu-

tion and FOV [29].

$$\delta x = \delta u, \quad (2.5)$$

$$\Delta x = N\delta u, \quad (2.6)$$

where  $\delta x$  and  $\Delta x$  of ASM are independent to the propagation distance  $z$ , different from those of FAM. The computational complication of ASM happens due to the two 2D Fourier transforms for backpropagation. Compared to the FAM, the computational size increases linearly proportional to  $z$  because the ASM does not have the scaling factor. Thus, the ASM is theoretically more accurate than the FAM. However, its computational load is problematic in far field imaging.

To overcome the storage and computational burdens of ASM but preserve its accuracy, we propose the Fresnel Scaled Angular Spectrum Method (FSASM). The propagated field, as in the FAM, is expressed as  $E_o(x, y) = S(x, y) \frac{ke^{jkz}}{j2\pi z} e^{j\frac{k}{2z}(x^2+y^2)}$ , with  $S(x, y)$  being a slowly-varying function multiplied by a spherical wave. This may be substituted into Eq. (2.4) and the order of integration changed:

$$S(x, y) = \frac{jze^{-jkz}}{2\pi k} \iint du dv e^{-j(k_u u + k_v v)} E_s(u, v) \iint dk_u dk_v e^{jz\sqrt{k^2 - k_u^2 - k_v^2}} e^{j(k_u x + k_v y)} e^{-j\frac{k}{2z}(x^2+y^2)}. \quad (2.7)$$

We define  $\tilde{S}(k_x, k_y) = \iint dx dy e^{-j(k_x x + k_y y)} S(x, y)$  and insert it to find

$$\tilde{S}(k_x, k_y) = \frac{jze^{-jkz}}{2\pi k} \iint du dv e^{-j(k_u u + k_v v)} E_s(u, v) \iint dk_u dk_v e^{jz\sqrt{k^2 - k_u^2 - k_v^2}} \iint dx dy e^{-j(k_x x + k_y y)} e^{j(k_u x + k_v y)} e^{-j\frac{k}{2z}(x^2+y^2)}. \quad (2.8)$$

The inner integral is evaluated as

$$\tilde{S}(k_x, k_y) = \frac{jze^{-jkz}}{2\pi k} \iint du dv e^{-j(k_u u + k_v v)} E_s(u, v) \iint dk_u dk_v e^{jz\sqrt{k^2 - k_u^2 - k_v^2}} \left[ \frac{-2\pi jz}{k} e^{j\frac{z}{2k}[(k_u - k_x)^2 + (k_v - k_y)^2]} \right]. \quad (2.9)$$

To continue, we separate the exponential kernel  $e^{jz\sqrt{k^2 - k_u^2 - k_v^2}} = e^{jzR(k_u, k_v)} e^{jkz} e^{-j\frac{z}{2k}(k_u^2 + k_v^2)}$  with  $R(k_u, k_v) = \sqrt{k^2 - k_u^2 - k_v^2} - k + (k_u^2 + k_v^2)/2k$ . This transforms the convolution integral into two successive convolutions, one of which applies the fourth and

higher-order terms of the angular spectrum kernel, and the second of which applies the second-order Fresnel diffraction term which is implemented by the conventional FAM. The FSASM is a modified FAM which pre-corrects the FAM for the fourth-order and higher terms missing from the FAM before applying the FAM. Inserting this separated kernel and cancelling terms, the result is

$$\tilde{S}(k_x, k_y) = \frac{z^2}{k^2} e^{j\frac{z}{2k}(k_x^2 + k_y^2)} \iint du dv e^{-j(k_u u + k_v v)} E_s(u, v) \\ \iint dk_u dk_v e^{jzR(k_u, k_v)} e^{-j\frac{z}{k}(k_u k_x + k_v k_y)}. \quad (2.10)$$

Reinserting  $E_o(x, y)$  and rearranging again, the result is

$$E_o(x, y) = \frac{ze^{jkz}}{j(2\pi)^2} e^{j\frac{k}{2z}(x^2 + y^2)} \iint dk_x dk_y e^{j(k_x x + k_y y)} e^{j\frac{z}{2k}(k_x^2 + k_y^2)} D(k_x, k_y), \\ \text{with} \\ D(k_x, k_y) = \frac{1}{(2\pi)^2} \iint dk_u dk_v e^{-j\frac{k_u z}{k} k_x - j\frac{k_v z}{k} k_y} e^{jzR(k_u, k_v)} [\iint du' dv' e^{-j(k_u u' + k_v v')} E_s(u', v')]. \quad (2.11)$$

To transform the outer integral into a Fresnel diffraction integral, we substitute  $u = -\frac{k_x z}{k}$  and  $v = -\frac{k_y z}{k}$ :

$$E_o(x, y) = \frac{ke^{jkz}}{j2\pi z} e^{j\frac{k}{2z}(x^2 + y^2)} \iint dk_x dk_y e^{-j\frac{z}{z}(ux + vy)} e^{j\frac{k}{2z}(u^2 + v^2)} D(u, v), \\ \text{with} \\ D(u, v) = \frac{1}{(2\pi)^2} \iint dk_u dk_v e^{j(k_u u + k_v v)} e^{jzR(k_u, k_v)} [\iint du' dv' e^{-j(k_u u' + k_v v')} E_s(u', v')]. \quad (2.12)$$

This is the desired result. Note that no approximations have been made from deriving the FSASM from the ASM. The diffraction calculation has been divided into two parts. The first part is to calculate the field  $D(u, v)$  that is corrected for fourth-order and higher terms of the diffraction kernel. As shown above, this is accomplished using the ASM in the calculation of  $D(u, v)$  with the kernel  $e^{jzR(k_u, k_v)}$  rather than  $e^{jz\sqrt{k^2 - k_u^2 - k_v^2}}$ . The second step is to apply the FAM to the corrected data  $D(u, v)$  in the calculation of  $E_o(x, y)$ . This allows the rescaling inherent to the FAM so that the sampling rate may be increased and therefore the computational burden decreased.

The limitation of the FSASM is that the convolution in the calculation of  $D(u, v)$  increases the support of  $D(u, v)$  relative to  $E_s(u, v)$  increasing  $N$  in Eq. (2.2) and therefore a smaller sampling rate  $\delta x$  is required. The sampling of the kernel  $e^{jzR(k_u, k_v)}$  in the frequency domain is aliased for a sufficiently large  $z$  unless the support of  $D(u, v)$  is increased. If the support of  $D(u, v)$  is permitted only to double compared to  $E_s(u, v)$  so that  $\delta x$  is halved, then  $z < \frac{2N\delta u^4}{\lambda^3}$ . In practice this estimate, like the conditions governing the use of the FAM, may be overly stringent as the higher-order oscillatory terms tend to cancel more readily. While the FSASM is exact, its computational burden may become overly great with large  $z$  as the ASM does. Unlike the ASM, the limitation ultimately lies in the approximation of the rapidly-varying component of the field, the spherical wave, by a quadratic approximation given by the FAM.

Both the ASM and the FSASM are compared by using off-axis hologram data in Fig. 2.2. A point object was experimentally interfered by a spherical reference field at 2 m range. Fig. 2.2(a) shows  $200 \times 200$  pixel image from original  $1944 \times 1944$  pixel image for the phase of object scattered field. We propagate the scattered field back to the object plane by using two propagation methods. Fig. 2.2(b) shows  $1944 \times 1944$  pixel image for the backpropagation with the ASM. The point object occupies approximately 135 pixels in diameter by using the FWHM criterion. Since the pixel resolution is equivalent to the pixel pitch in the ASM, Eq. (2.5), the point size is estimated to  $297 \mu\text{m}$  approximately. Fig. 2.2(c) shows  $29 \times 29$  pixel image for the backpropagation with the FSASM. Since the Fresnel scaling factor is applied to the FSASM, the pixel resolution is  $296 \mu\text{m}$  corresponding to the object size of the ASM. For a given aperture size, the effective pixel resolution is determined by the Fraunhofer formular [4]. Thus, the FSASM does not suffer from the upsampled data unlike the ASM. The FSASM achieves 575.4 mm FOV, however, the ASM does only 4.3 mm due to the upsampled resolution.

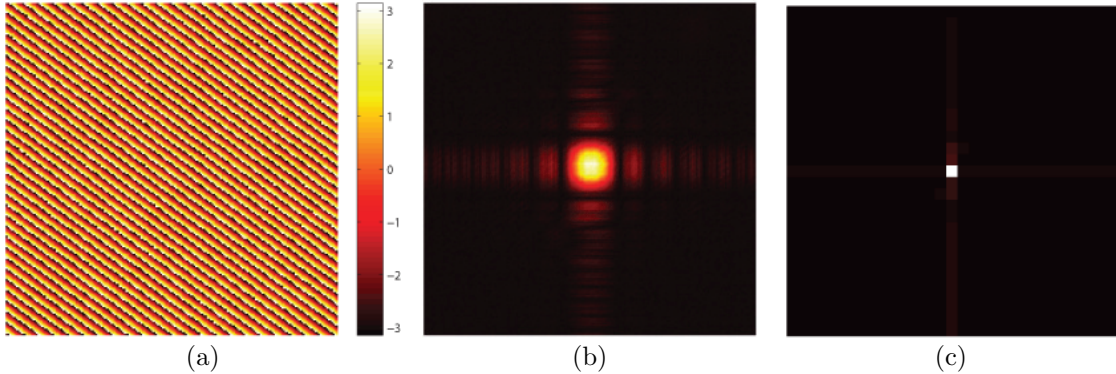


FIGURE 2.2: Comparison of field propagations : (a) phase of object scattered field, (b) backpropagation w/ ASM, and (c) backpropagation w/ FSASM.

## 2.4 Compressive sensing

Shannon's sampling theorem states that a band-limited signal can be exactly reconstructed from discrete measurements as long as it is sampled at twice its maximum frequency (Nyquist rate). It is generally true but it can be too strict when it comes to sparse data in a certain basis. Compressive sensing theory claims that highly accurate reconstruction is possible with fewer measurements than the number of unknowns provided (1) the signal of interest is sparse in some basis, that is, the signal can be expressed by a linear combination of very few basis vectors and (2) the measurement matrix that maps the signal to its observations, satisfies the restricted isometry properties (RIP) [25,30]. Let an  $S$ -sparse signal be defined by a signal that has only  $S$  nonzero components and  $(N - S)$  coefficients that are exactly zero. A matrix  $H \in R^{M \times N}$  satisfies  $S$ -RIP with constant  $\delta_S \in (0, 1)$  for any  $S$ -sparse signal  $f$  if

$$(1 - \delta_S)\|f_T\|_2^2 \leq \|H_T f_T\|_2^2 \leq (1 + \delta_S)\|f_T\|_2^2, \quad (2.13)$$

where  $T$  denotes the set of indices on which the  $S$ -sparse signal is supported, and  $\|\cdot\|_2$  denotes the Euclidean norm. This implies that the submatrix  $H_T$  of  $H$ , composed of  $S$  columns of  $H$ , mostly retains the Euclidean length of  $S$ -sparse signal forming a

nearly isometric transformation. This also implies that the condition number of the  $S$ -column sub-matrix  $H_T$  is near 1 (in fact in the range of  $[1 - \delta_S, 1 + \delta_S]$ ), which consequently ensures that any  $S$ -column sub-matrix  $H_T$  is well-conditioned.

In many applications, the input signal might be sparse in some basis  $\Psi$ , which is not necessarily the canonical basis. Compressive sensing theory requires that the sparsity basis and the measurement (sensing) matrix be incoherent in such circumstances. The coherence measure  $\mu_1(H, \Psi)$  is defined by

$$\mu_1(H, \Psi) = \sqrt{N} \max_{\substack{1 \leq m \leq M \\ 1 \leq n \leq N}} |\langle h_m, \psi_n \rangle|, \quad (2.14)$$

where  $h_m$  and  $\psi_n$  denote the  $m$ -th row of  $H$  and the  $n$ -th column of  $\Psi$ , respectively. Candés *et al.* [5] and Donoho [6] showed that if  $f$  is  $S$ -sparse in  $\Psi$ , and  $M$  satisfies

$$M \geq C \cdot \mu_1^2(H, \Psi) \cdot S \cdot \log N, \quad (2.15)$$

then an accurate reconstruction can be obtained with high probability by solving

$$\theta = \arg \min_{\theta} \|\theta\|_1 \text{ such that } g = Hf = H\Psi\theta, \quad (2.16)$$

where  $\|\theta\|_1 = \sum_i |\theta_i|$ . In Eq. (2.15), the smaller  $\mu_1$  is, the more accurate the reconstruction would be for the same  $M$ .

Figure 2.3 conceptually illustrates the compressive sensing theory. Possible solutions are drawn in the space defined by proper basis. Decompressive reconstruction searches a point intersecting the possible solutions and the measurement plane. The point sparsely represents the measurement solution in the space.

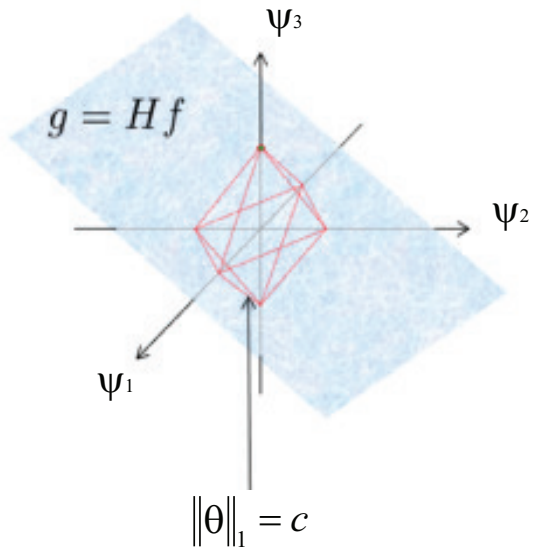


FIGURE 2.3: Illustration of compressive sensing : the red color lines indicate possible solutions satisfying the sparsity constraint, and the blue plane indicates the measurement.

# 3

## Holographic Tomography

Digital holography is not regarded as a 3D tomographic imaging technique because 3D object estimation from coherent scattering data is ill-posed [31]. To solve the ill-posed problem, tomographic imaging traditionally recorded holograms of objects illuminated by a sequence of plane waves. The method, in turn, forms the basis of diffraction tomography [32]. In compressive holography, decompressive inference enables 3D tomography from a single 2D digital hologram instead of multiple holograms. While holographic tomography is ill-posed, using sparsity priors and nonlinear estimators may alleviate the limit of single shot tomography.

### 3.1 Computational Design

This section builds the mathematical model for holographic tomography. To be able to apply linear field propagation models such as the FAM, ASM, and FSASM, one must determine the fields to be propagated from the intensity of the holograms. In the reconstruction process, algorithmic filtering replaces the conventional holographic methods. The hologram intensity  $I(u, v)$  is expressed by interfering scattered field  $E_s(u, v)$  and reference field  $R(u, v)$  in Fig. 3.1.

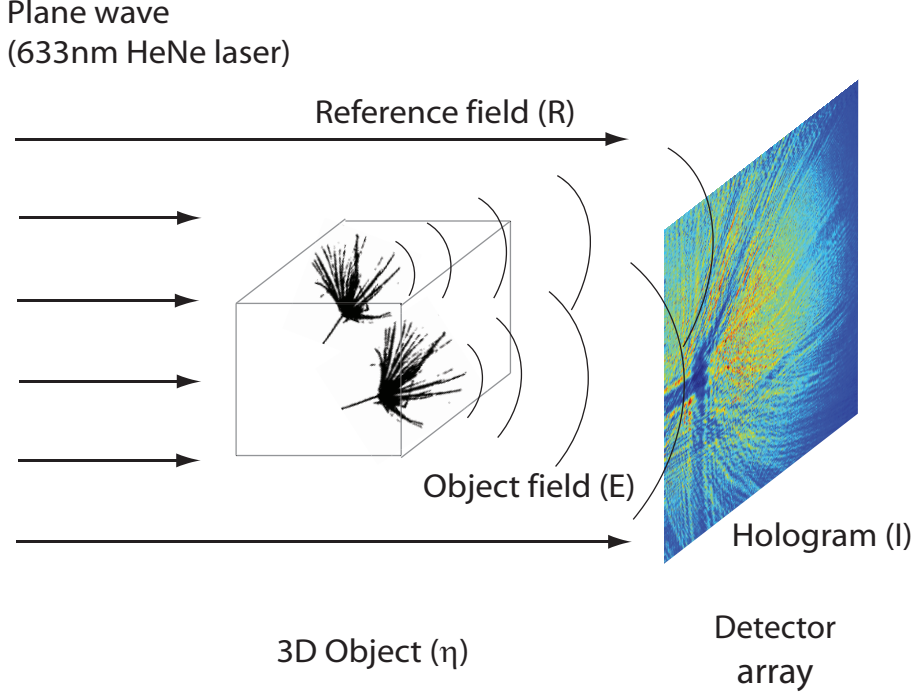


FIGURE 3.1: Gabor hologram geometry.

$$I(u, v) = |R(u, v) + E_s(u, v)|^2, \quad (3.1)$$

$$= |R(u, v)|^2 + |E_s(u, v)|^2 \quad (3.2)$$

$$+ R^*(u, v)E_s(u, v) + R(u, v)E_s^*(u, v),$$

where the superscript ‘\*’ denotes a complex conjugate and  $(u, v)$  indicates the spatial coordinates. The squared field term  $|E_s(u, v)|^2$  produces the autocorrelation term in the Fourier domain. The conjugate term  $R(u, v)E_s^*(u, v)$  also produces the twin image in the reconstruction.

Gabor holography possesses an ambiguity due to the squared-field term and the conjugate term due to the in-line geometry [3]. If the object is known to be far from the sensor plane, this ambiguity can be partially removed by filtering the scattered field axially to remove the conjugate and squared-field terms. In Gabor holography, the term  $|R(u, v)|^2$  is simply a constant, hence the effect of  $|R(u, v)|^2$  can be removed by eliminating the constant term at the origin in the Fourier trans-

form of the interference irradiance measurements  $I(u, v)$ . Since we simply assume  $R(u, v)$  is 1, we may proceed with  $R^*(u, v)E_s(u, v) + R(u, v)E_s^*(u, v) + |E_s(u, v)|^2 = 2\text{Re}\{E_s(u, v)\} + |E_s(u, v)|^2 = 2\text{Re}\{E_s(u, v)\} + e(u, v)$ .

The scattered field  $E_s$  is defined under the Born approximation as

$$E_s(u, v) = \iiint dx dy dz \eta(x, y, z) h(u - x, v - y, z), \quad (3.3)$$

where  $h$  is the point spread function [28] and  $\eta$  is the scattering potential of 3D object. Note the sample spacings are  $\Delta_x = \Delta_y = \Delta$  and the sampling pitch is  $\Delta_z$  in the  $z$ -axis. Also, the number of pixels along each dimension of the detector is  $N$ . The discrete model of scattered field can be expressed by using the ASM,

$$E_{n_1 n_2} = \mathcal{F}_{2D}^{-1} \left\{ \sum_l \hat{\eta}_{m_1 m_2 l} e^{ikl\Delta_z} e^{il\Delta_z \sqrt{k^2 - m_1^2 \Delta_k^2 - m_2^2 \Delta_k^2}} \right\}, \quad (3.4)$$

where  $e^{ikl\Delta_z}$  indicates the phase delay of individual slices in the 3D datacube and  $\hat{\eta}_{m_1 m_2 l}$  is the Fourier transform of discrete scattering potential  $\eta_{m_1 m_2 l} = \eta(m_1 \Delta, m_2 \Delta, l \Delta_z)$ .

A linear transformation of the holographic measurement is expressed by using Eq. (3.4),

$$\bar{g} = G_{2D} Q B f, \quad (3.5)$$

where  $B = \text{bldiag}(F_{2D}, F_{2D}, \dots, F_{2D})$  with  $F_{2D}$  being the matrix representing the 2D DFT whose size is  $(N_x \times N_y) \times (N_x \times N_y)$  and ‘‘bldiag’’ denoting the block diagonal matrix,  $Q = [P_1 P_2 \cdots P_{N_z}]$  with  $[P_l]_{m_1 m_2} = e^{ikl\Delta_z} e^{il\Delta_z \sqrt{k^2 - m_1^2 \Delta_k^2 - m_2^2 \Delta_k^2}}$ ;  $[P_l]_{m_1 m_2}$  represents the element of the matrix  $P_l$  at the intersection of the row  $m_1$  and the column  $m_2$ , and  $G_{2D}$  represents the 2D inverse DFT matrix. The Gabor hologram measurement may be simplified by

$$g = 2\text{Re}\{\bar{g}\} = 2\text{Re}\{G_{2D} Q B f\} = 2\text{Re}\{H f\} + q + n, \quad (3.6)$$

where  $g \in \mathbb{R}^{N_x \times N_y}$  represents the Gabor hologram from which the constant term is removed, and  $q$  and  $n$  denote vectorized  $|E(x, y)|^2$  and additive noise, respectively.

The nonlinear term  $q$  is filtered in the measurement plane since the reconstruction algorithm propagates only diffraction patterns. The conjugate term is also filtered by confining the estimation to only the one side of the measurement plane (i.e.,  $z \geq 0$ ). In this manner, we may effectively isolate most of the errors that result from the Gabor hologram.

The linear transformation model, Eq. (3.6), is inverted by decompressive inference by either selecting a basis, typically a particular wavelet basis, on which  $f$  may be assumed to be sparse or by enforcing a sparsity constraint on the total variation, as defined by Rudin *et al.* [33], of  $f$ . We choose the second approach here and estimate  $f$  as

$$\hat{f} = \arg \min_f \|f\|_{TV} \text{ such that } g = Hf, \quad (3.7)$$

where  $\|f\|_{TV}$  is defined by

$$\|f_k\|_{TV} = \sum_k \sum_{n_1} \sum_{n_2} |\nabla(f_k)_{n_1, n_2}|, \quad (3.8)$$

where  $f_k$  denotes a 2D plane of the 3D object datacube. We adapt the two-step iterative shrinkage/thresholding (TwIST) algorithm [34] to solve this optimization problem. The TwIST algorithm is a nonlinear two-step iterative version of iterative shrinkage/thresholding (IST) algorithm to improve the convergence rate. The algorithm minimizes an objective function to solve linear inversion problems with a non-quadratic regularizer such as TV. The objective function is regularized by the non-quadratic term to overcome the ill-posed nature of the linear transformation.

### 3.2 Sampling and Processing w/ Simulation

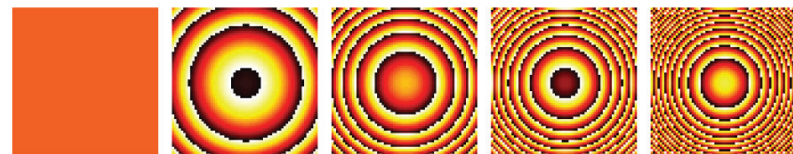
As a numerical example, we consider single shot holographic tomography by using the reconstruction model of Section 3.1. The volume reconstruction from a single 2D hologram is ill-posed, however, the insufficient measurement problem can be mitigated by imposing sparsity constraints on the reconstructed volume. With the total variation constraints, structure is localized in space because the total variation is minimized when the fewest edges are present in the reconstruction [35].

The simulation code is composed of six functional blocks as presented in Appendix C. In the Parameters block, a Gabor holographic measurement is designed at a wavelength of  $0.633 \mu\text{m}$ . We generate a 3D datacube composed of  $64 \times 64 \times 5$  pixels in the object space. The pixel pitch is designed considering the aliasing analysis in Appendix B. The maximum phase variation of the angular spectrum is less than  $\pi$ , using the aliasing analysis with a pixel pitch of  $30 \mu\text{m}$ . The effective aperture size of the hologram measurement is determined by the size of the object features, so the space resolutions are given by  $\Delta_x \approx w$  and  $\Delta_z \approx 4w^2/\lambda$  [11]. Assuming a cross section of about 2 pixels (e.g.  $60 \mu\text{m}$ ), the axial resolution achieves about 23 mm in reconstruction.

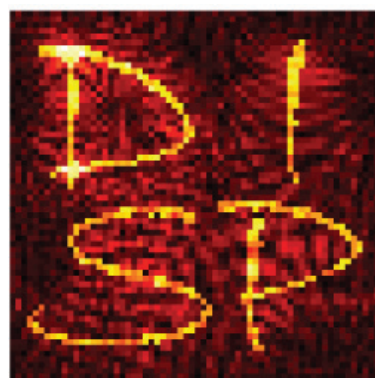
In the Object Generation block, 2D objects such as alphabet letters are axially distributed as shown in Fig. 3.2(a). Note the axial coordinate goes from the left ( $z = 0$ ) to the right ( $z = 92\text{mm}$ ) and the first object plane ( $z = 0$ ) is the measurement plane. In the Propagation Kernel block, angular spectrums for individual slices are defined depending on the propagation distances. Since this simulation is performed in near-field imaging, the ASM, Eq. (3.4), numerically propagates the object field to the measurement plane. We use a plane wave for the object illumination, thus, the illumination field is simply set to one. Fig. 3.2(b) shows phases of the propagation kernels in the datacube.



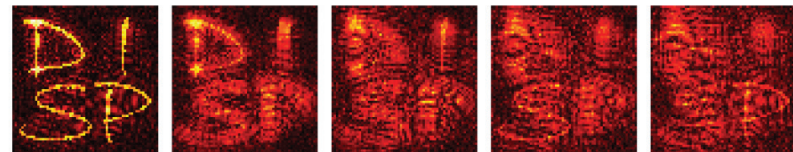
(a)



(b)



(c)



(d)



(e)

FIGURE 3.2: Simulations for holographic tomography : (a) 3D object, (b) phase of transfer functions, (c) scattered field, (d) backpropagation, and (e) compressive reconstruction.

In the Field Measurement and Backpropagation block, propagated fields are linearly summed in the measurement plane as shown in Fig. 3.2(c). To demonstrate algorithmic field filtering, the squared fields  $q$ , Eq. (3.6) of objects are added to the propagated fields. Then, the measurement fields are propagated back to the original object planes by using adjoint propagation kernels. The backpropagation of a Gabor hologram is an ill-posed inverse problem so the individual slices suffer from out-of-focus images from the other slices in Fig. 3.2(d).

In the Propagation Operator block, we define forward and backward propagation operators. Here the backward propagation is the adjoint operation of the forward propagation. Since Gabor holography generates only real values in Eq. (3.6), both propagations take only real values of propagated fields in the measurement plane.

In the TwIST Algorithm block, the object estimate is iteratively updated under sparse constraint on a TV basis. The TwIST algorithm is composed of a least square minimization term and a TV-based denoising term. The two terms are regularized by the parameter  $\tau$  in the algorithm. Also, the number of iterations is a critical parameter to stably converge to the solution. Since the TV-based denoising term is not defined in a complex domain, the real and imaginary parts are independently processed in a vectorized form. The vectorized data of measured fields are plugged into the linear inverse model of iterative method. Fig. 3.2(e) shows the decompressive reconstruction using the TwIST algorithm. The decompressive reconstruction is superior to the backpropagation since the out-of-focus images are effectively removed. The object field is filtered in 3D space by holding the squared field in the measurement plane. This reconstruction model can be applied to single shot tomography by replacing the measured fields with a real Gabor measurement.

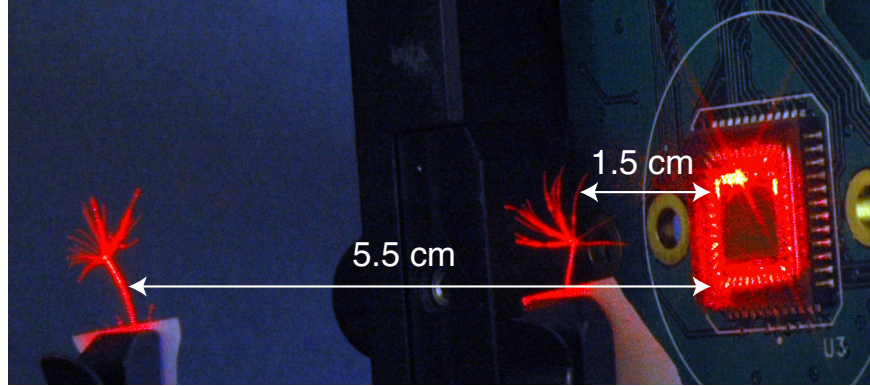


FIGURE 3.3: Experimental apparatus.

### 3.3 Dandelion Project

Compressive holography demonstrates the feasibility of single shot tomography in Gabor geometry. The compressive reconstruction algorithm pushes scattered energy into the proper spatial locations, while holding the squared terms back to the measurement plane. In the result, two dandelion parachutes are successfully reconstructed in 3D datacube by using compressive holographic tomography.

#### 3.3.1 Optical design and experimental results

This project is proposed to show feasible performance of the compressive reconstruction process. So optical process is minimally used for the feasibility in regard to computational and optical co-design. As illustrated in Fig. 3.3, we illuminated two seed parachutes of common dandelions (*taraxacum*) with a collimated, spatially filtered Helium-Neon (HeNe) laser of 632.8 nm wavelength. The two objects are axially placed 1.5 cm and 5.5 cm away from the detector array, respectively.

The light scattered from the object and the collimated beam, which served as the reference beam, overlapped on a Lumenera LU100  $1280 \times 1040$  pixel focal plane array with pixel pitch of  $5.2 \mu\text{m}$ . We cropped the array of measurements to a  $1024 \times 1024$  array, which is then downsampled to a  $512 \times 512$  array using B-spline functions. The measurement vector  $g$  is then zero-padded on all four sides to create a  $712 \times 712$

array to avoid the artifact of the circular convolution caused by using FFT. For our simulations, the matrix  $H$  has the size of  $(712 \times 712) \times (712 \times 712 \times 10)$  with 10 being the number of object planes that can be changed by adjusting the related parameter.

Fig. 3.4(b) and 3.4(c) are photographs of the two seed parachutes. The illumination and scattered fields were captured in the Gabor hologram shown in Fig. 3.4(a). Fig. 3.4(d) is the 3D datacube estimated from the Gabor recording by the TV-minimization algorithm. The stem and the petals, representing the high-frequency features in the image, are reconstructed clearly. In addition, the axial locations of two parachutes are accurately estimated. We conjecture that the errors in some planes are mainly reconstruction errors and the effects of noise, and they occur because of the rather insufficient number of measurements. Fig. 3.4(e) shows the backpropagated field that is obtained by numerically backpropagating the hologram using the propagation kernel  $h$  in Eq. (3.3) [4]. In contrast to the reconstruction in Fig. 3.4(d), the backpropagated field shows out-of-focus features obscuring the object features of the two parachutes.

Optical measurement over a finite aperture is bandlimited. The band volume is the support in the 3D Fourier space of  $\eta(x', y', z')$  for sampling  $E(x, y)$  over a finite aperture (see Appendix B). Spatial resolution in imaging systems is assumed to be inversely proportional to the limits of the band volume, which yields transverse resolution  $\Delta_x = \lambda z / D$  for objects at range  $z$  observed over aperture  $D$  and the axial resolution is  $\Delta_z = \lambda(2z)^2 / D^2$  [11]. The effective aperture size  $D$  for a Gabor hologram is determined by size of the object feature. A feature of cross section  $w$  produces a diffraction pattern with cross section  $D \approx \lambda z / w$ . This implies that  $\Delta_x \approx w$  and  $\Delta_z \approx 4w^2 / \lambda$ . The dependence of axial resolution on feature size is the result of the “missing cone” in the paraxial band volume [28]. The missing cone may be removed by recording holograms along multiple axes. We anticipate, for example, that object features of approximately  $100\mu\text{m}$  cross section will be observed under visible light

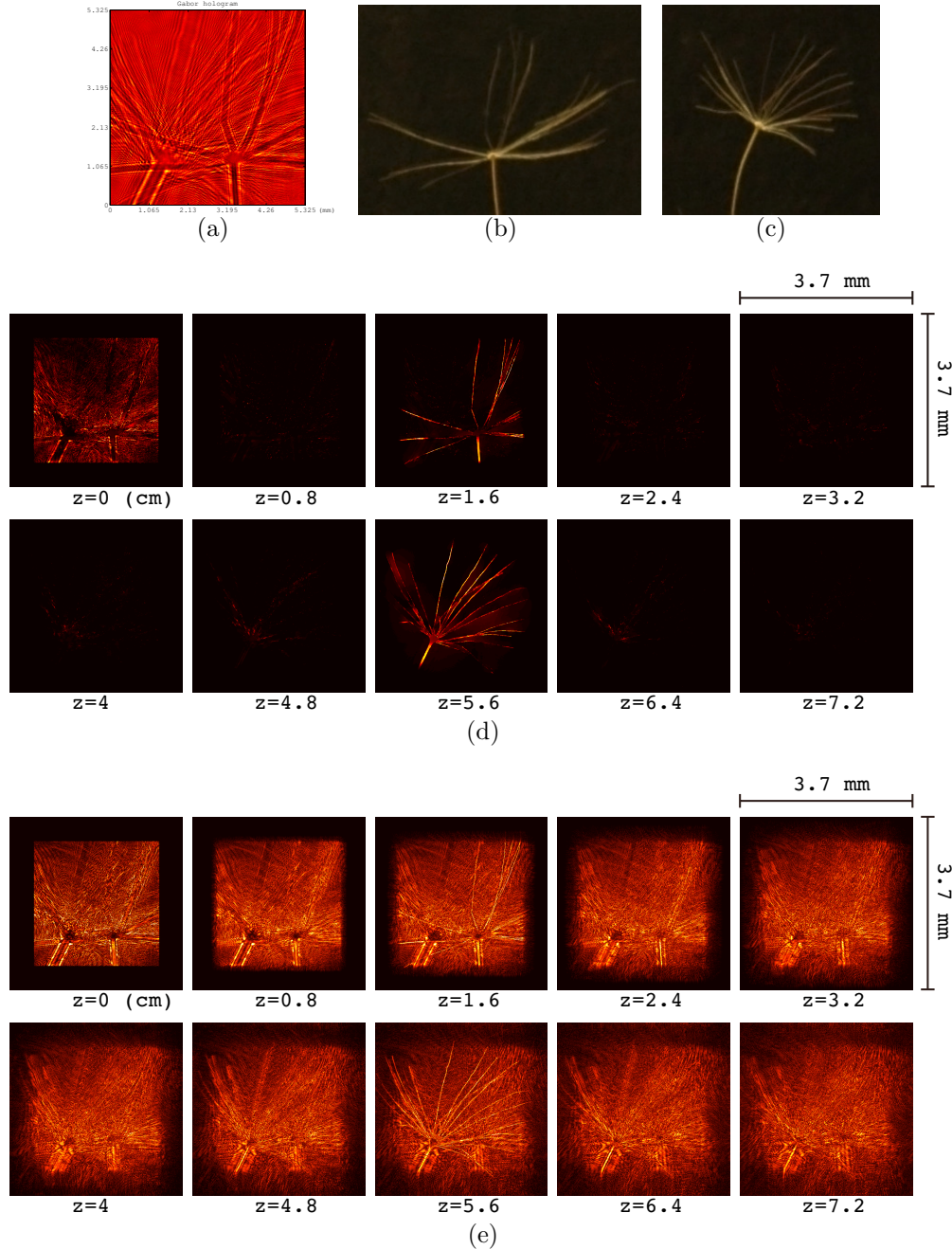


FIGURE 3.4: (a) Raw Gabor hologram for seed parachutes of taraxacum arranged as in Fig. 3.3, (b) and (c) photographs of the individual objects, (d) transverse slices at various ranges of the tomographic reconstruction of the 3D data volume containing both objects, and (e) transverse slices at various ranges of the backpropagated (numerical refocusing) field.

with approximately 1 cm axial resolution.

The algorithm iteratively finds the proper weight of each object plane on the basis of diffraction pattern correlation. Since the squared field  $e$  has nothing to do with the diffraction patterns, the reconstruction error caused by  $e$  tends to remain in the detector plane  $z = 0$ . In this way, we effectively remove the effect of the squared field (zero-order) term in the reconstructions. In the experiment, our results show that we can obtain a 3D datacube with  $10.4 \mu\text{m}$  transverse resolution and 0.8 cm axial resolution reconstructed from a single 2D hologram. This demonstrates the main advantages of compressive holography. 2D holographic measurement naturally encodes 3D object data and decompressive inference can infer multidimensional object from lower dimensional data.

### 3.4 Micro-Bead Project

Compressive holographic tomography is applied to microscopic imaging for micro-bead samples. A microscopic objective lens can be inserted in the object beam of LU holography to magnify the microscopic features of the samples. In the optical design, LU holography is adopted because optical process in the object beam can be independent to the reference beam. The 3D distribution of micro-bead samples are reconstructed by using compressive holographic tomography.

A Mach-Zehnder setup was used to implement LU holography with a 633 nm HeNe laser as shown in Fig. 3.5. A spatially filtered beam was collimated by a 1-inch f/2 lens, and split into the object and the reference beams. In the object arm, a 0.65 NA microscopic objective lens was used to image 1  $\mu\text{m}$  size beads. To limit the bandwidth of the autocorrelation term, the bandwidth of object scattered fields was optically low-pass filtered in the Fourier space. 2D holographic data was recorded on a PointGrey 1624  $\times$  1224 pixels focal plane array with a pixel pitch of 4.4  $\mu\text{m}$ . In the optical design, a single measurement achieves the resolutions of  $\Delta_x = 0.5 \mu\text{m}$  and  $\Delta_z = 3 \mu\text{m}$  with 0.65 NA (see Appendix B).

The reconstructed datacube of the multiple beads is visualized in the 3D space

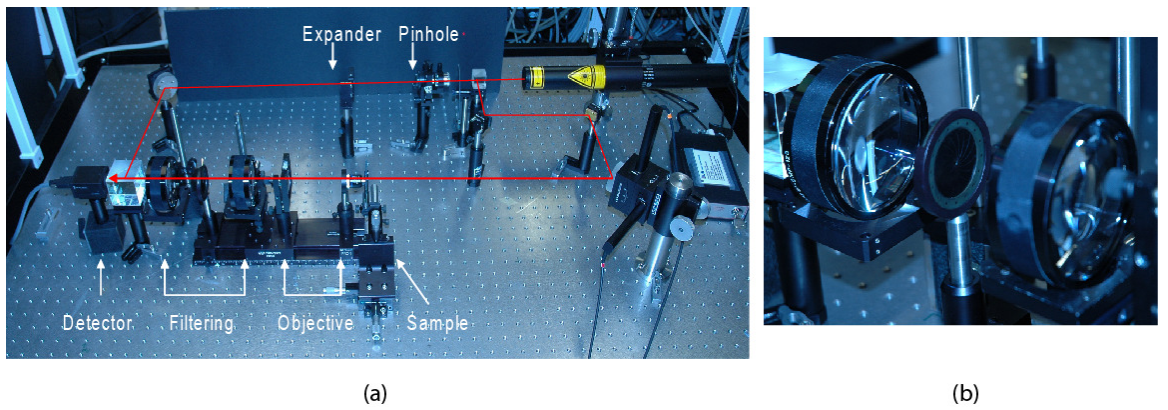
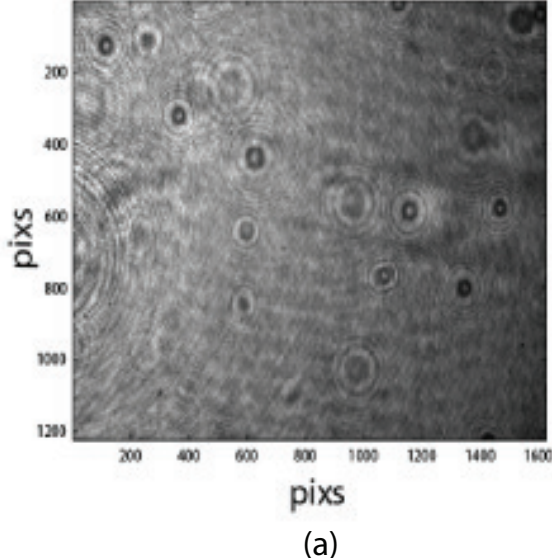


FIGURE 3.5: Microscopic object setup: (a) experimental setup and (b) optical low-pass filtering in Fourier domain.



(a)



(b)

FIGURE 3.6: Multiple beads reconstruction: (a) 2D holographic measurement, and (b) reconstructed datacube

using the Avizo software as shown in Fig. 3.6 (b). In the 3D visualization, the longitudinal dimension is scaled 10 times larger than the transverse dimension. The results show that compressive holography can reconstruct the 3D object datacube from the 2D hologram data. Fig. 3.7 shows the transverse slices of the reconstructed datacube and the backpropagated fields. The axial resolution is  $1 \mu\text{m}$  and the trans-

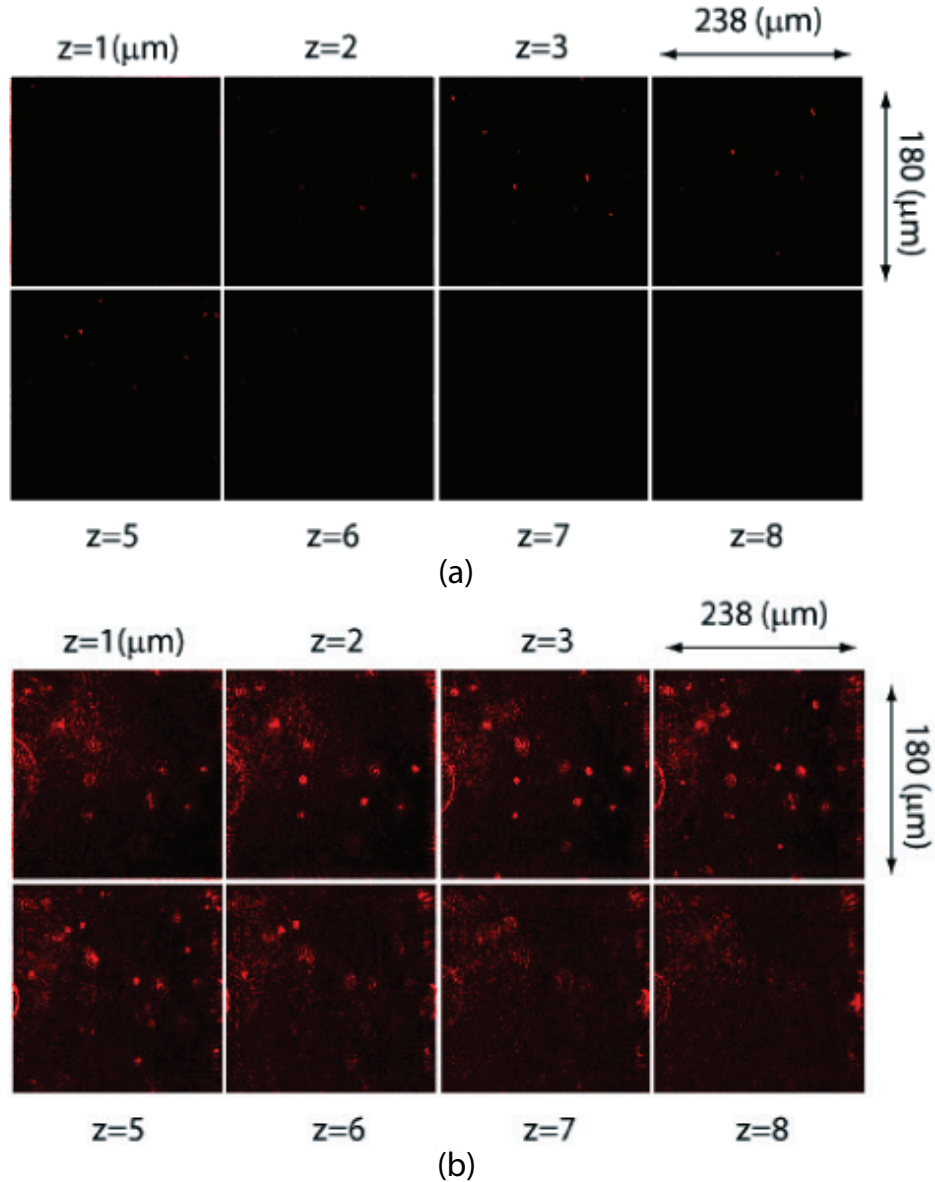


FIGURE 3.7: Transverse slices of tomographic reconstruction : (a) compressive reconstruction, and (b) backpropagated fields.

verse slice covers  $238 \times 180 \mu m$  field of view in the object space. In the optical design, the 2D holographic measurement is optical focused at the plane that is  $1\mu m$  before the first transverse slice. The compressive reconstruction presents high resolution images without the out-of-focused features compared to the backpropagated fields.

### 3.5 Water Flea Project

Microscopic holographic tomography is performed without using an objective lens. The pixel pitch of digital image sensor is a few microns so microscopic imaging is possible in a lensless compact system. The lensless imaging system provides aberration-free and cost-effective microscopic measurements [36]. Since holographic field extraction is not necessary in compressive holographic tomography, Gabor geometry is adopted for the compact system. Compressive holography demonstrates video-rate tomographic image acquisition of living water fleas as an extension of single shot tomography.

#### 3.5.1 Microscopic holographic tomography

The lensless Gabor geometry uses a point source as illumination so object scattered fields are modeled by considering the divergence. Figure 3.8 shows a schematic of the compressive holographic microscope. The incident field  $R(x, y; z_{FPA})$  is a spherical wave originating from  $z = 0$ , and the object scattered field  $E_s(x, y; z_{FPA})$  is expressed by linearly propagating the object scattering density  $\eta(x', y'; z')$ .

$$E_s(x, y; z_{FPA}) = \iiint dx' dy' dz' R(x', y'; z') \eta(x', y'; z') h_F(x - x', y - y'; z_{FPA} - z'), \quad (3.9)$$

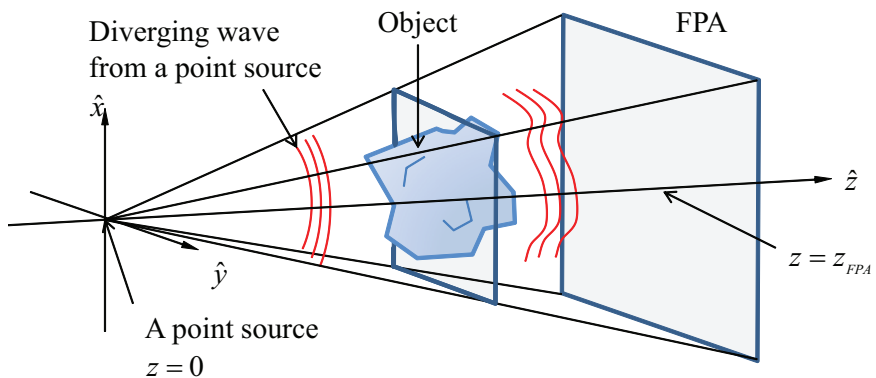


FIGURE 3.8: A schematic of the compressive holographic microscope.

where  $(x, y; z)$  and  $(x', y'; z')$  indicate the coordinates of the FPA plane and the object space, respectively.  $z_{FPA}$  denotes the position of the focal plane arrays (FPA). Since the effective NA is smaller than the system NA, the Huygens-Fresnel point-spread function (PSF)  $h_F$  [28] does not lose any numerical accuracy. The scattered field is re-expressed by replacing the reference field  $R$  with the PSF  $h_F$  and by considering coordinate conversion,

$$\begin{aligned} E_s(x, y; z_{FPA}) &= \iiint dx' dy' dz' h_F(x', y'; z') \eta(x', y'; z') h_F(x - x', y - y'; z_{FPA} - z'), \\ &= h_F(x, y; z_{FPA}) \iiint dx'' dy'' dz' C(z') \eta\left(\frac{x'' z'}{z_{FPA}}, \frac{y'' z'}{z_{FPA}}; z'\right) h_F(x - x'', y - y''; \frac{z_{FPA} - z'}{z'/z_{FPA}}), \\ &= h_F(x, y; z_{FPA}) \int dz' C(z') \mathcal{F}_{2D}^{-1} \left\{ \mathcal{F}_{2D} \left\{ \eta\left(\frac{x'' z'}{z_{FPA}}, \frac{y'' z'}{z_{FPA}}; z'\right) \right\} H_F(k_{x''}, k_{y''}; \frac{z_{FPA} - z'}{z'/z_{FPA}}) \right\}, \end{aligned} \quad (3.10)$$

where  $H_F(k_x, k_y; z)$  is the Fresnel transfer function and the coordinate  $(x'', y'')$  is defined by  $x'' = x' z_{FPA}/z'$  and  $y'' = y' z_{FPA}/z'$ . The uniform phase delay is given by the object plane  $z'$  and the FPA plane  $z_{FPA}$ ,

$$C(z') = e^{jkz_{FPA}(1-z_{FPA}/z')} \quad (3.11)$$

The discrete scattering model  $E_s(n_1\Delta, n_2\Delta; z_{FPA})$  is multiplied by the conjugate reference field  $R^*(n_1\Delta, n_2\Delta; z_{FPA})$  to remove the diverging reference field.

$$\begin{aligned} R^*(n_1\Delta, n_2\Delta; z_{FPA}) E_s(n_1\Delta, n_2\Delta; z_{FPA}) &= \\ \sum_l C\left(\frac{l\Delta_z}{z_{FPA}}\right) \mathcal{F}_{2D}^{-1} \left\{ \mathcal{F}_{2D} \left\{ \eta(n_1''\Delta'', n_2''\Delta''; l\Delta_z) \right\}_{m_1 m_2 l} H_F(m_1\Delta_k, m_2\Delta_k, \frac{z_{FPA} - l\Delta_z}{l\Delta_z/z_{FPA}}) \right\}, \end{aligned} \quad (3.12)$$

where  $\Delta$  and  $\Delta''$  denote the sampling spaces in the FPA plane and in the object space, respectively. Also,  $\Delta_z$  is the axial sampling space in the object space. The Fourier sampling space  $\Delta_k$  satisfies different relations:  $\Delta\Delta_k = 2\pi$  and  $\Delta''\Delta_k = 2\pi z'/z_{FPA}$ . Then, the discrete scattering model is used for the linear transformation and the compressive reconstruction process follows as shown in Section 3.1.

### 3.5.2 Optical design and experimental results

In the experiment, a HeNe laser of  $0.633 \mu\text{m}$  wavelength was used as a light source. A microscope objective with 0.65 NA manufactured by LOMO is used to generate a spherical wave for illuminating the sample. While a microscope objective was used for a point source generation, we note that alternative sources using fiber or holographic components could achieve similar NA. The microscope objective is chosen to have a larger NA (0.65) than the microscope system NA (0.27) to ensure uniform illumination intensity on the FPA. A Lumenera CMOS image sensor records the hologram with  $1280 \times 1024$  pixels,  $5.2 \mu\text{m}$  pixel pitch, and 15 fps frame rate. Fig. 3.9 (a) and (b) show photographs of the microscope instrumentation and the container. In the container, two living water fleas (cyclopes) are floating in water. The relative positions of the microscope objective and the samples are adjusted by two 3-axis translation stages. The depth of the container is 3 mm and the distance from the FPA to the illuminating microscope objective is 10 mm.

Fig. 3.10 shows a raw Gabor hologram. The incident spherical field is removed from the hologram by simply deleting DC term in Fourier transform. To avoid

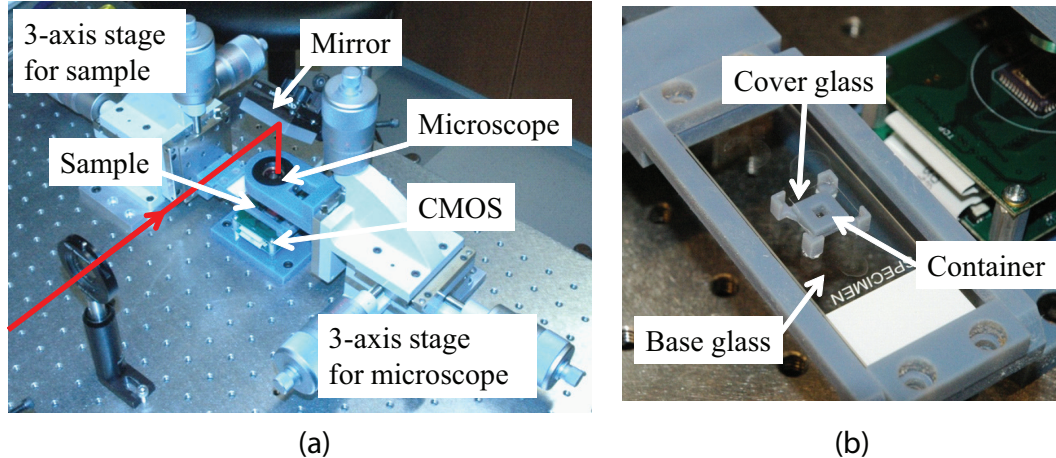


FIGURE 3.9: Photographs of (a) the holographic microscope and (b) a water container in which water cyclopes are swimming.



FIGURE 3.10: Raw image of a Gabor hologram.

circular wrapping effects, approximately 20 pixels around the boundaries are set to zero using only  $1240 \times 984$  pixels data. The preprocessed data are defined as  $g$  to reconstruct the object scattering density.

Fig. 3.11 compares the backpropagated fields with the compressive reconstructions. Fig. 3.11 (a) and (b) show transverse slices of the backpropagated fields at  $z = 3.31$  mm and  $z = 1.87$  mm, respectively. Fig. 3.11 (c) and (d) show transverse slices at the same axial positions with those in Fig. 3.11 (a) and (b). The compressive reconstructions clearly show better sectioning capability. Also, the compressive holographic reconstructions suffer less from the undesired background “noise” resulting in better image contrast. For example, the tails and antennae of both water cyclopses are remarkably sharper and more discernible in Fig. 3.11 (c) and (d), compared to those in Fig. 3.11 (a) and (b).

The theoretical resolutions of imaging system is determined by the wavelength and aperture size (see Appendix B). Since the system NA is 0.27, the theoretical resolutions are estimated as  $\Delta_x = 1.17\mu m$  and  $\Delta_z = 17.3\mu m$ . In practice, however,

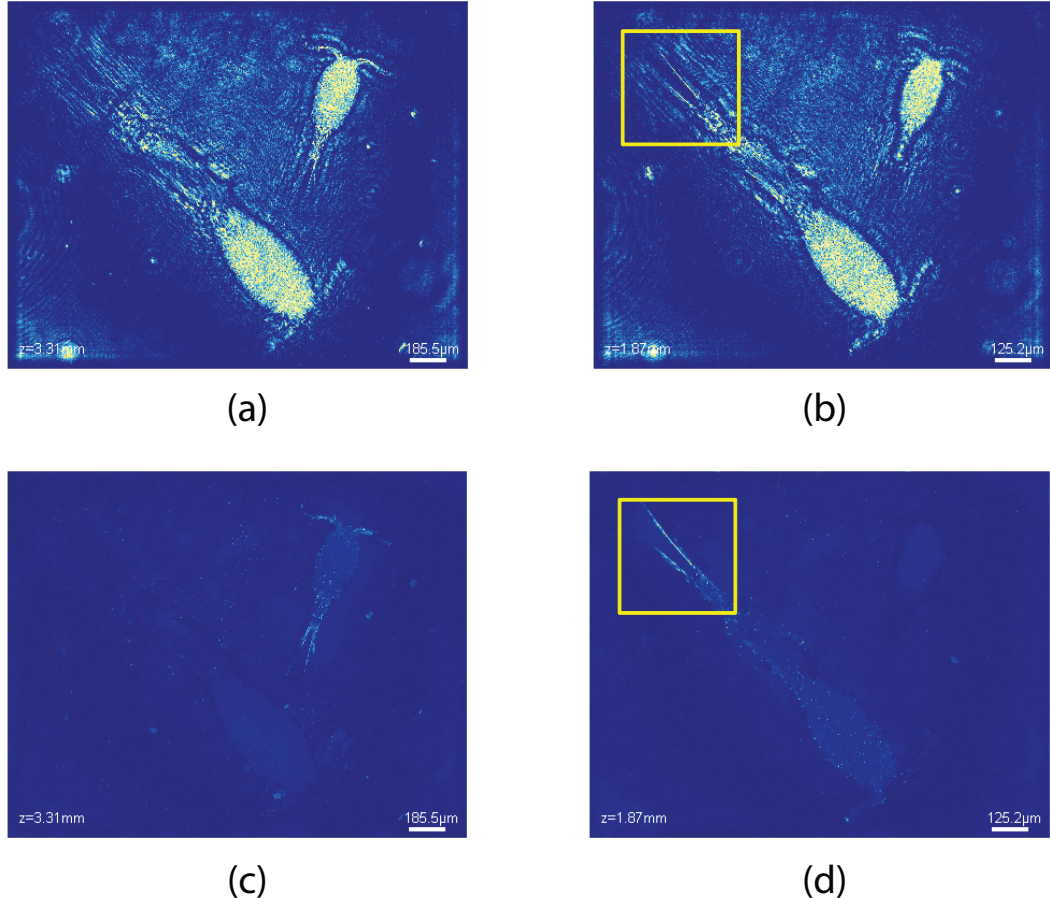


FIGURE 3.11: A comparison of reconstructions at chosen axial positions: (a-b) the backpropagation reconstructions and by (c-d) the compressive holographic reconstructions using the data shown in Fig. 3.

the resolutions are limited by other factors such as the quantization of FPA, various sources of noise, and object feature sizes. Practical resolutions may thus be estimated by considering amounts of diffraction signals [37]. For example, one tail of the water cyclops on the left-hand side in Fig. 3.11 produced diffractions over approximately 400 pixels. In the theoretical resolutions, the effective aperture size is  $D_e = 2.1\text{mm}$  and the propagation distance is approximately 7.0 mm. The estimated effective numerical aperture  $NA_e$  is approximately 0.15 so the practical resolutions become  $\Delta_x = 2.2\mu\text{m}$  and  $\Delta_z = 59\mu\text{m}$ .

Figure 3.12 compares the zoomed-in tails, marked by rectangles in Fig. 3.11

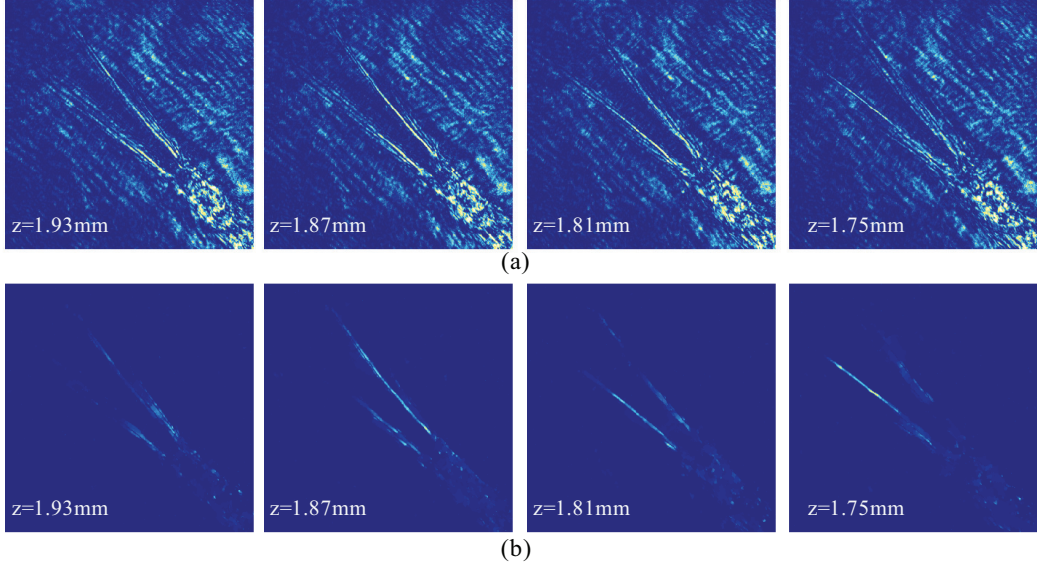


FIGURE 3.12: A comparison of the magnified tails, marked by rectangles in Figs. 4(b) and 4(d), of (a) the backpropagation reconstruction and (b) the compressive holography reconstruction.

(b) and (d), of (a) the backpropagated fields and (b) the compressive holography reconstruction. The detailed comparison clearly shows the difference between the two results and their changes in the axial direction.

A 3D visualization of the compressive reconstruction is shown in Fig. 3.13. The size of the 3D datacube is  $1280 \times 1024 \times 35$  pixels with the 2 mm depth range and  $60 \mu\text{m}$  resolution. The reconstruction takes about one and a half hours with the code written in Matlab 7.0.4 when the data is processed on Intel Xeon CPU X5650 at 2.67GHz and 24GB of RAM.

The Born approximation is valid when the product of the index contrast and object size is less than one-quarter wavelength [38, 39]. For example, the platelets of Sapphirinidae that belongs to the same subclass as water cyclopses have a high refractive index as 1.8 [40]. The bodies of cyclopses are not in the valid range of the Born approximation so its inner structure cannot be correctly reconstructed by our method.

Fig. 3.14 presents an alternative visualization of the same 3D datacube. Fig. 3.14 (a) shows an image of the maximum intensity values along the propagation directions in the datacube. Fig. 3.14 (b) represents a map of the axial positions corresponding to the maximum values in Fig. 3.14 (a). In Fig. 3.14 (c), a range map is constructed using the HSV space, where the hue (h) represents Fig. 3.14 (b), and the value (v) represents Fig. 3.14 (a). The saturation (s) is set to 1.

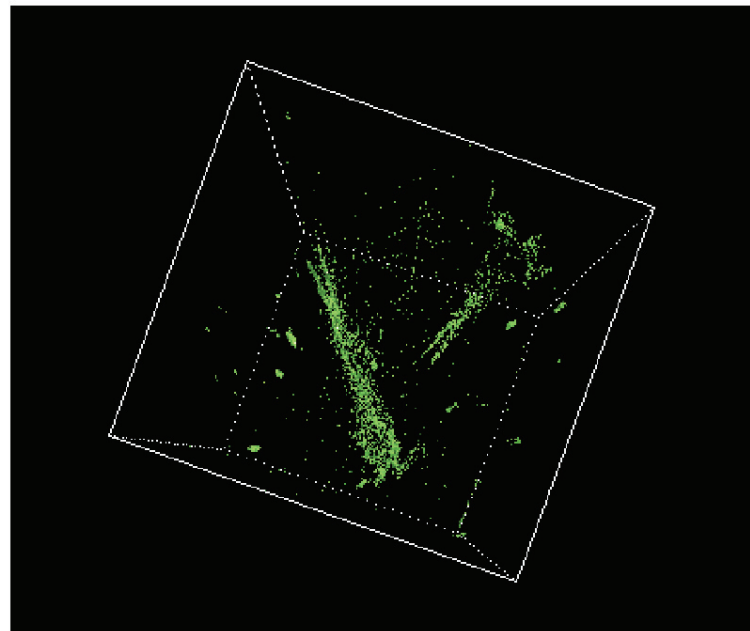


FIGURE 3.13: A 3D visualization of the compressive holography reconstruction.

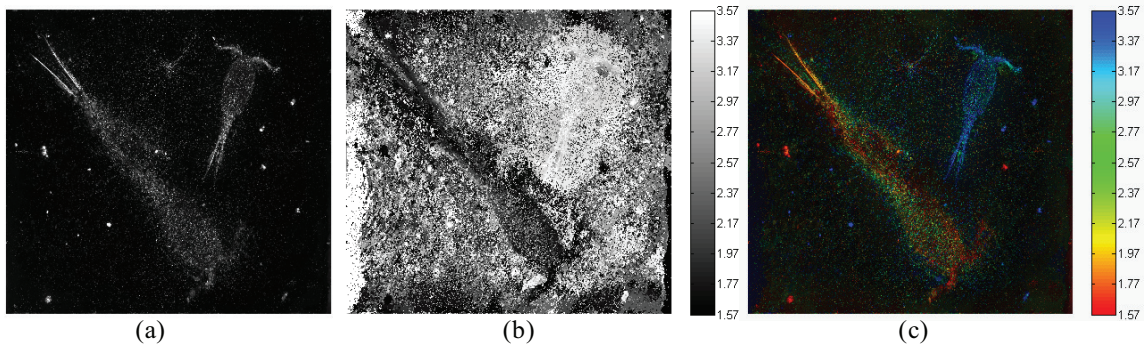


FIGURE 3.14: Images of (a) the maximum intensity values of the reconstructed density ( $f$ ) along the propagation directions and (b) a map of the axial positions corresponding to the maximum values in (a). (c) A range colormap represents the HSV space.

# 4

## Holographic Tomography of Diffuse Objects

Incoherent image estimation using multiple speckle realizations retrieves the smooth features destroyed by speckle effects. In coherent imaging, speckle is the random pattern arising from the interference of multiple fields due to the random roughness of object surfaces [41]. The speckle image is not in general compressible. For diffuse objects, however, one may neglect the random phase associated with coherent scatter and focus instead on a nonnegative scattering density. This approach efficiently forms an incoherent image of the object from holographic data and the incoherent image is typically compressible.

### 4.1 Computational Design

This section describes decompressive holographic image estimation for diffuse objects. The high sensitivity of LU holography enables compressive holography for weak scattering of diffuse objects [18]. In LU holography, off-axis geometry is used to make a linear phase reference field  $R = e^{j\alpha u}$ , where  $\alpha$  is the angular frequency [1]. The object-scattered field is separated from the other terms in the Fourier domain thanks to the linear phase term. Applying Fourier filtering to Eq. (3.3), the scattered

field term  $R^*(u, v)E_s(u, v)$  can be extracted.

The scattered field is also defined by the Born approximation and the ASM in the same manner with Section 3.1. After Fourier filtering, the holographic measurement has complex field values without the squared term and the conjugate term. Then, the  $k$ -th holographic measurement  $g_k$  can be written by,

$$g_k = Hf_k + w_k, \quad (4.1)$$

where  $g_k \in \mathbb{C}^{M \times 1}$  with  $M = N_x \times N_y$  and  $w_k$  indicates independent additive Gaussian noise.

Fully-developed speckle means that speckle patterns are statistically independent on an intensity basis [41]. In fully-developed speckle realizations, the total intensity is defined by  $I_s = \sum_{k=1}^K I_k$  and the standard deviation of the total intensity is defined by  $\sigma_s = \sqrt{\sum_{k=1}^K \bar{I}_k^2}$  for  $k \in \{1 \cdots K\}$ . Here  $\bar{I}_k$  denotes the mean value of each intensity  $I_k$ . Then the speckle contrast ( $C$ ) is given by

$$C = \frac{\sigma_s}{\bar{I}_s} = \frac{\sqrt{\sum_{k=1}^K \bar{I}_k^2}}{\sum_{k=1}^K \bar{I}_k}. \quad (4.2)$$

Assuming identical mean intensities for all realizations, the contrast reduces to  $C = 1/\sqrt{K}$ . Note the speckle contrast is inversely proportional to the factor of  $\sqrt{K}$ . At the same time, the signal-to-noise ratio increases as  $\sqrt{K}$ .

For the fully-developed speckle realizations, the 3D scattered field  $f = [f_1 \ f_2 \ \cdots \ f_N]^T$  with  $N = N_x \times N_y \times N_z$ , has the complex circular Gaussian probability density [41]:

$$p(f) = \frac{1}{\pi^N \det(R_f)} \exp(-f^H R_f^{-1} f), \quad (4.3)$$

where  $E[f] = 0$ ,  $R_f = E[ff^H] = \text{diag}(E[|f_1|^2], E[|f_2|^2], \cdots, E[|f_N|^2]) = \text{diag}(\alpha_1, \alpha_2, \cdots, \alpha_N) = \text{diag}(\alpha)$ . Symbolically, we write  $f \sim CN(0, R_f)$ . The covariance  $W$  is defined by  $\sigma^2 I$  with  $I$  denoting the  $M \times M$  identity matrix. This statistical model implies that  $g$

has also a complex Gaussian probability density with zero mean and covariance  $R_g$ :  
 $g \sim CN(0, R_g)$ , with  $R_g = HR_fH^H + \sigma^2 I = H(R_f + \sigma^2 I)H^H$ .

Since  $HH^H = I$ , the minimum-norm solution [42] to the inverse problem in Eq. (4.1) is given by

$$\hat{f}_k = H^H (HH^H)^{-1} g_k = H^H g_k = H^H H f_k + H^H w_k. \quad (4.4)$$

For diffuse objects, our goal is to estimate the incoherent image of the scattered field (e.g. the diagonal elements of  $R_f$ )

$$\hat{s}_n = \frac{1}{K} \sum_{k=1}^K |\hat{f}_{nk}|^2. \quad (4.5)$$

Let  $H = [h_1 \ h_2 \ \cdots \ h_N]$  where  $h_n$  denotes the n-th column of  $H$ , and  $[H^H H]_{mn} = \langle h_m, h_n \rangle = {h_m}^H h_n$ . Thus, the expected value of the estimate  $\hat{s}$  can be expressed as

$$\begin{aligned} d &= E[\hat{s}] \\ &= \frac{1}{K} \sum_{k=1}^K \text{Diag} \left( E[\hat{f}_k \hat{f}_k^H] \right) \\ &= \text{Diag} \left( E[\hat{f} \hat{f}^H] \right) \\ &= \text{Diag} \left( H^H H R_f H^H H + \sigma^2 H^H H \right) \end{aligned} \quad (4.6)$$

where the third equality holds because the probability density of  $\hat{f}_k$  is the same for all  $k$ . In particular, the fourth equality in Eq. (4.6) indicates that

$$E[\hat{s}_n] = \sum_{m=1}^N |\langle h_n, h_m \rangle|^2 \alpha_m + \sigma^2 \langle h_n, h_n \rangle = \sum_{m=1}^N |{h_n}^H h_m|^2 \alpha_m + \sigma^2 \|h_n\|^2, \quad (4.7)$$

where  $\|h\|$  denotes the Euclidean norm of  $h$ . Then Eq. (4.7) implies that

$$d = E[\hat{s}] = B\alpha + \sigma^2 W, \quad (4.8)$$

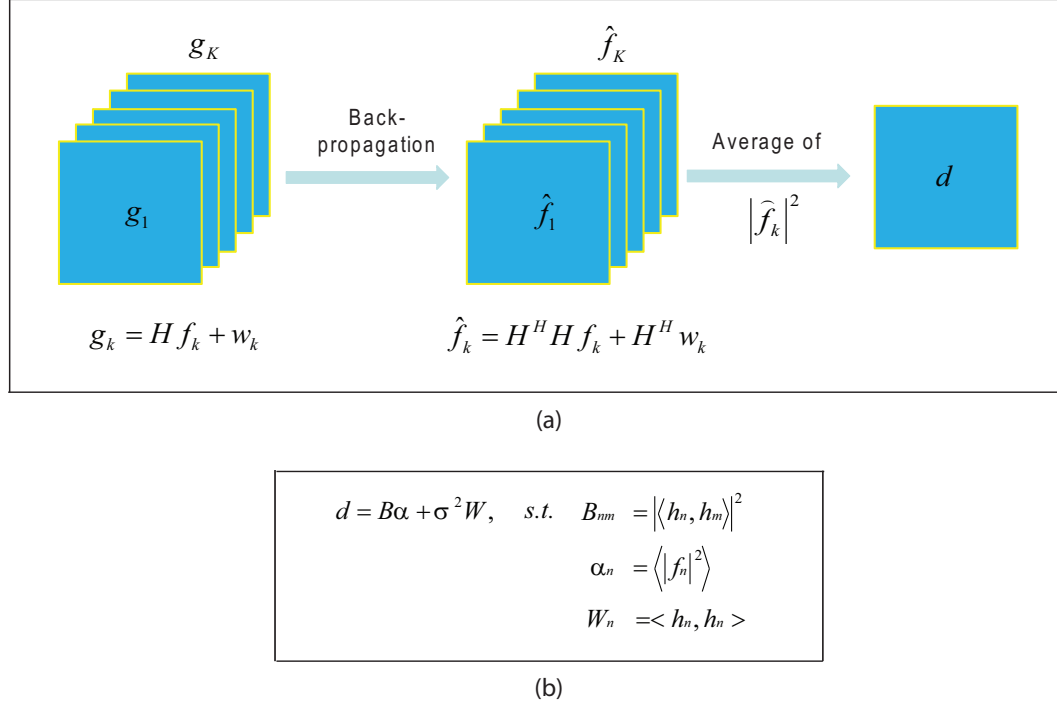


FIGURE 4.1: Incoherent image estimation : (a) synthetic measurements, and (b) forward model in incoherent image basis.

where  $\alpha = \langle |f|^2 \rangle$  and  $d$  are defined as *synthetic measurements*. Our goal is to estimate  $\alpha$  from a set of multiple speckle realizations. Figure 4.1 simply illustrates the process of the incoherent image estimation.

Eq. (4.8) suggests we may solve the constrained optimization problem:

$$\alpha^* = \arg \min_{\alpha} \frac{1}{2} \|d - B\alpha\|_2^2 + \beta \Phi(\alpha). \quad (4.9)$$

The functional  $\Phi(\alpha)$  imposes constraints on  $\alpha$ . For compressive inference,  $\Phi$  enforces the sparsity constraints. When the incoherent scattered field is expected to have a smooth surface, we can assume that the gradient of the incoherent image is sparse. This sparsity can be incorporated by minimizing the TV of the estimate. We define TV for our problem as  $\Phi(\alpha) = \|\alpha\|_{TV} = \sum_{n_x} \sum_{n_y} \sum_{n_z} |\nabla(\alpha_{n_z})_{n_x, n_y}|$ .

The sparsity-constrained estimates are known to be near optimal when the columns of the system matrix form approximately an orthonormal basis [43]. To transform

our system matrix to such an orthonormal basis, we apply a preconditioning method and convert  $d = B\alpha + \sigma^2 W$  to  $\tilde{d} = Pd = PB\alpha + \sigma^2 PW = \tilde{B}\alpha + \sigma^2 \tilde{W}$ , and we solve

$$\alpha^* = \arg \min_{\alpha} \frac{1}{2} \|\tilde{d} - \tilde{B}\alpha\|_2^2 + \beta\Phi(\alpha), \quad (4.10)$$

instead of Eq. (4.9).

If  $B$  has full rank, the preconditioner  $P$  may be chosen such that  $\tilde{B} = PB$  is as unitary as possible. An immediate choice of unitary  $\tilde{B}$  would be the identity matrix:  $\tilde{B} = I$ . In this case, the preconditioner  $P$  is merely the inverse of  $B$  and the estimation problem becomes an inverse problem. However, the matrix could often be rank deficient or ill-conditioned, some nonzero singular values of  $B$  either excessively amplify the noise or cause numerical instability. To alleviate this problem, we choose  $P$  in the Tikhonov-regularized sense. That is  $P = (B^H B + \lambda_t I)^{-1} B^H$ , where  $\lambda_t$  is a Tikhonov regularization parameter. Note that  $\lambda_t$  suppresses or ignores a small number of singular vectors associated with numerically unstable or zero singular values.

## 4.2 Sampling and Processing w/ Simulation

As a numerical example, we consider diffuse object tomography by using the incoherent image estimation model of Section 4.1. The coherent image estimation model of Section 3.1 cannot be used for diffuse object imaging due to speckle effects. To avoid these complications, we utilize fully-developed speckle realizations to statistically obtain the incoherent scattering density. By imposing sparsity constraints on the total variation of the incoherent scattering density, incoherent structure is localized in space and the speckle is suppressed [35].

Processing of diffuse object tomography is again described in the processing blocks of the given code (see Appendix C). In the Parameters block, we set up holographic parameters and object space. A LU hologram is taken using a coherent source at the

wavelength of  $0.633\text{ }\mu\text{m}$ . We generate a 3D datacube composed of  $64 \times 128 \times 3$  pixels in the object space. The pixel pitch is designed to  $50\text{ }\mu\text{m}$  at  $\pm 50\text{ mm}$  propagation ranges.

In the Object Generation block, three rectangular shapes are defined axially distributing in Fig. 4.2(a). We design an objective lens to collect the scattered fields with an optical magnification. The center object plane is one-to-one imaged to the measurement plane at  $z = 0$ , and the other planes are placed in -50 mm and +50 mm ranges relative to the measurement plane. In the Propagation Kernel blocks, the ASM and the plane wave illumination are used in the same manner with holographic tomography in Chapter 3. Fig. 4.2(b) shows phases of the propagation kernels depending on the propagation distances. Since the center object plane is imaged to the measurement plane, the plane does not need a propagation phase.

In the Holographic Measurement and Backpropagation block, multiple speckle realizations support the incoherent image estimation for diffuse object tomography. The fully-developed speckle realizations are implemented by using multiple-angle illuminations which make the speckle realizations statistically independent each other. To generate the fully-developed speckle realizations in the simulation, independent random fields are applied resulting in complex object fields. The backpropagation of a single speckle realization shows the severely degraded image in Fig. 4.2(c). The averaged backpropagation of multiple speckle realizations show the better image in Fig. 4.2(d). Nevertheless, the tomographic image is still degraded by speckles and out-of-focus images.

In the Incoherent System Matrix block, the incoherent system matrix  $Q$  is generated by Fourier transforming the squared PSF. The system matrix  $Q$  projects the original 3D object to the backpropagated image via multiple speckled realizations. The Tikhonov regularization alleviates the ill-conditioned problem in tomographic reconstruction. Using the preconditioning method in Section 4.1, the inverted datacube

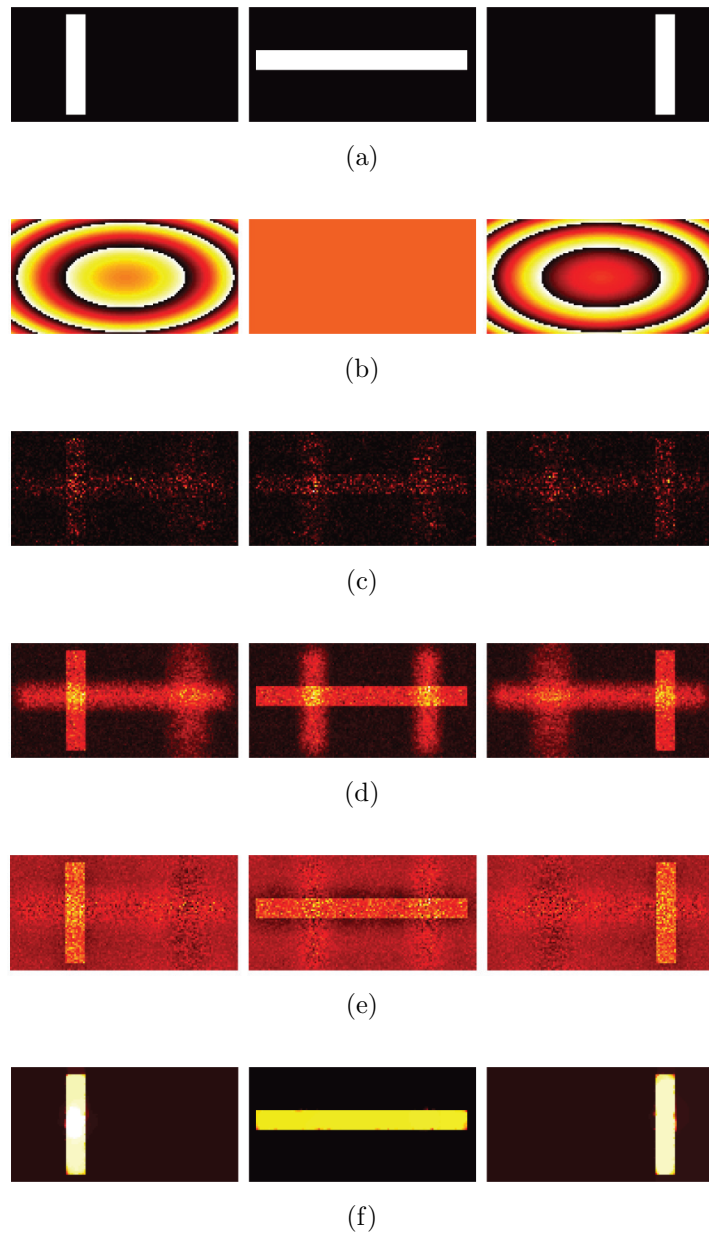


FIGURE 4.2: Simulations for diffuse object tomography : (a) 3D object, (b) phase of propagation kernels, (c) backpropagation of single speckled realization, (d) backpropagation averaged by 30 speckled realizations, (e) backpropagation using the Tikhonov regularization w/ 30 speckled realizations, and (f) compressive reconstruction w/ 30 speckled realizations.

shows better tomographic image reducing the out-of-focus features in Fig. 4.2(e). Note the Tikhonov regularization parameter  $\lambda_t$  is 1.0e-08 in the reconstruction.

In the TwIST Algorithm block, forward and backward projection operators are defined. The forward projection operator  $D$  is formed by a multiplication of Tikhonov-regularized inversion of  $Q$  and  $Q^*$  (e.g.  $\text{pinv}Q * Q$ ). The backward projection operator  $DT$  is an adjoint of the forward projection operator. The averaged backpropagation is inverted using the Tikhonov-regularized inversion of the incoherent system matrix,  $\text{pinv}Q$ , and input to the TwIST algorithm. The TwIST algorithm is regularized by TV sparsity constraints according to Eq. (4.9). The parameter  $\tau$  and the number of iterations are controlled to stably converge to the optimal solution. Fig. 4.2(f) shows the speckle suppressed image with 30 speckle realizations. Some artifacts remain in the overlapping region to the detector’s perspective, due to the ambiguity of decompressive inference.

### 4.3 Diffuse Object Project

We reconstruct the 3D incoherent image of a diffuse object from multiple realizations of the 2D speckled field measurements. To reduce the effect of speckle, we assume that the incoherent intensity image is sparse in some basis. Our inference relies on the estimation of the diagonal covariance [44] of the object scattered field. To demonstrate, we image some planate objects shaped as the letters ‘DISP’. Each letter is located at a different axial position and compressive reconstruction achieves approximately 5 mm depth resolution.

#### 4.3.1 Optical design and experimental results

The co-design approach makes the optical design support the computational design of the incoherent image estimation. For the optical support, LU holography was adopted separating the illumination beam from the reference beam. In the LU geometry, a static diffuser and a goniometer can be inserted in the illumination beam for fully-developed speckle realizations.

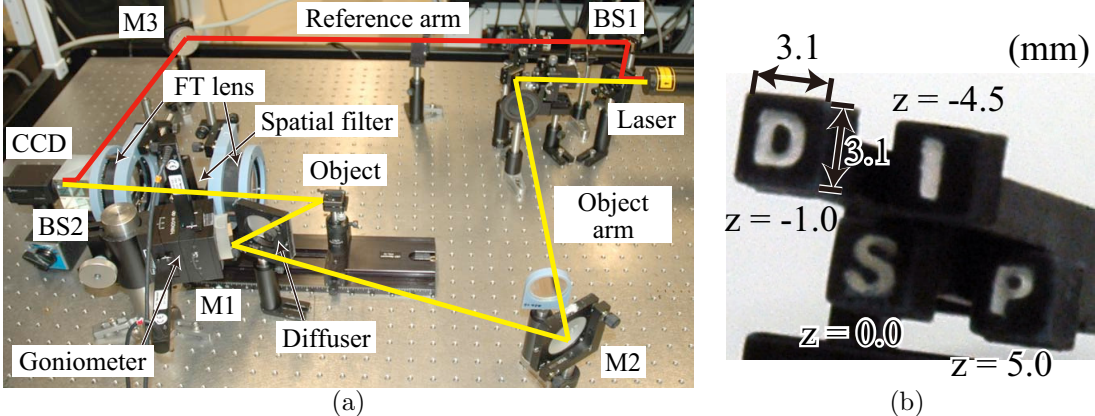


FIGURE 4.3: (a) A photograph of experimental setup: 'M', 'BS', and 'FT lens' represent a mirror, a beam splitter, and a Fourier transform lens, respectively, (b) a photograph of a 3D diffuse object 'DISP'

Figure 4.3(a) and 4.3(b) show photographs of the experimental setup and a 3D diffuse object 'DISP', respectively. The interference intensity was recorded by a CCD sensor, which has  $1624 \times 1224$  pixels with  $4.4 \mu\text{m}$  pixel pitch. The beams were created with a He-Ne laser at  $632.8 \text{ nm}$  wavelength. The spatial filter was applied in the Fourier domain of  $4f$  optical system with a focal length of 75 mm. The spatial filter ensures complete separation of the object scattered field from the undesired terms. The recorded intensity image was Fourier filtered to obtain the object scattered field. Consequently, the size of the separated speckle field, associated with only the object, is  $1582 \times 222$  pixels.

The object was illuminated through a stationary diffuser whose purpose is to fully develop the speckles in individual speckle realizations. To change the random phase patterns of the speckle fields, a goniometer was introduced to illuminate the diffuser from different angles for the speckle field measurements. The multiple speckle realizations produce stationary random phases by using the angular diversity of the illumination. Readers may be referred to Ref. [45] for more details on how a diffuser can be used to create uncorrelated speckle measurements.

A conventional approach for speckle reduction is to average the intensities of

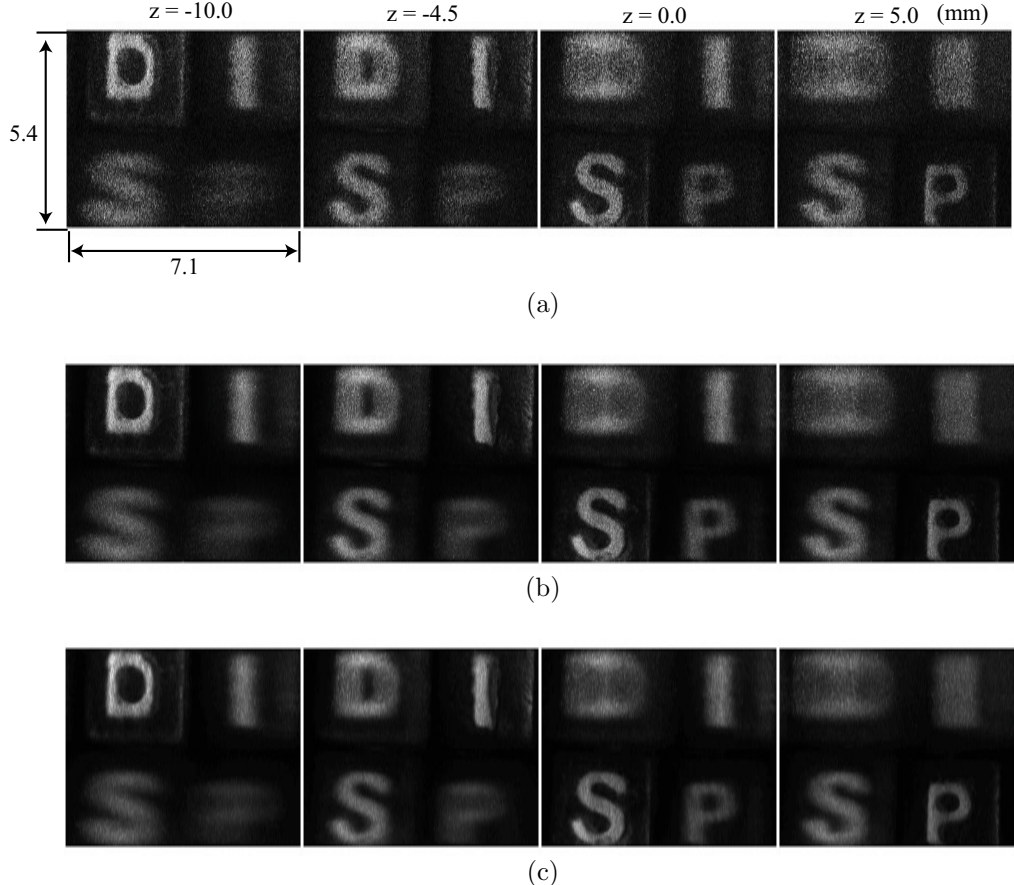


FIGURE 4.4: (a) The intensity of the backpropagation with a single speckle field, (b) the average of the backpropagation intensities of 50 speckle fields (see Eq. (4.5)), and (c) an image obtained by applying a  $5 \times 5$  median filter to the image in (b).

multiple backpropagated fields. Fig. 4.4(a) shows a backpropagation reconstruction with a single speckle field. Fig. 4.4(b) shows the average of the backpropagation reconstruction intensities of 50 speckle fields. The reconstruction is smoother and has better contrast when the multiple intensities are averaged. Nonetheless, speckle artifacts are still manifest and the axial resolution is poor. For example, although the letter ‘S’ becomes in focus and presents clear features in the third plane, the estimated intensity of the letter ‘S’ is strongly blurred into the second and fourth planes. For reference, Fig. 4.4(c) shows a speckle reduction result obtained by applying a  $5 \times 5$  median filter to the estimate in Fig. 4.4(b).

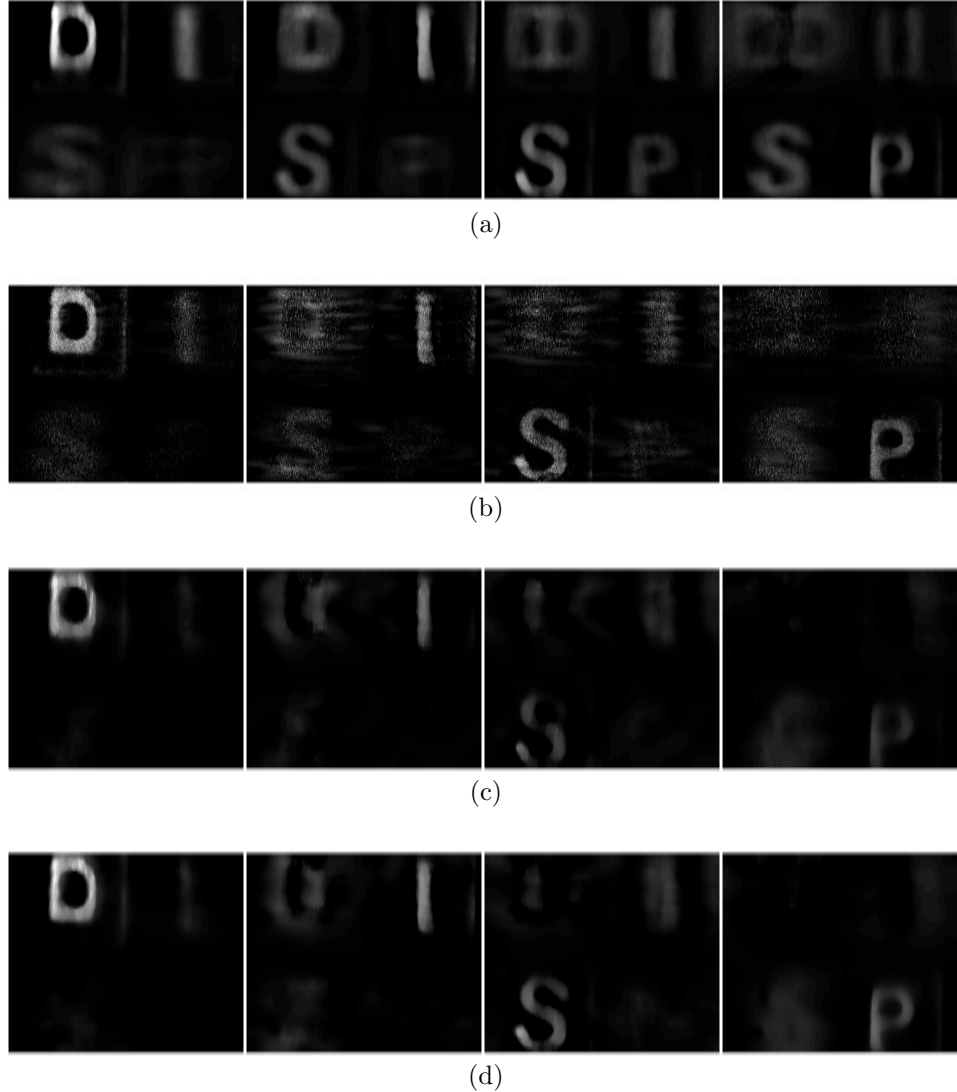


FIGURE 4.5: (a) An estimate obtained by solving Eq. (4.9), (b) a Tikhonov regularized pseudoinverse (i.e.,  $\tilde{d} = \tilde{B}\alpha + \sigma^2\tilde{W}$ ) with  $\lambda_t = 10^{-8}$  using 50 speckle fields both for (a) and (b), (c)-(d) reconstructions (with  $\beta = 0.3$ ) obtained by solving the preconditioned formulation in Eq. (4.10) with (c) a single speckled field, and (d) 50 speckled fields.

Figure 4.5(a) shows an estimate obtained by solving Eq. (4.9) when  $\tilde{d}$  is constructed with 50 speckle fields. Note that speckle artifacts have been significantly reduced, as indicated by the smooth surfaces of the letters ‘D’, ‘I’, ‘S’, and ‘P’. In addition, the estimate shows improved axial resolution, by suppressing the letters

out of focus. However, the blurred letters are still undesirable. Fig. 4.5(b) shows a Tikhonov pseudoinverse estimate from 50 speckle fields:  $\tilde{d} = \tilde{B}\alpha + \sigma^2\tilde{\omega}$ . In this reconstruction, although the axial resolution is improved by suppressing the blurred letters in the out-of-focus planes, the speckle artifacts are still manifest as the rough surfaces of the letters in focus. Fig. 4.5(d) shows an estimate obtained by solving Eq. (4.10) from the same  $\tilde{d}$ . The estimate shows remarkably suppressed speckle artifacts and improved axial resolution. For comparison, Fig. 4.5(c) demonstrates an estimate obtained by solving Eq. (4.10) with a single speckle field. The axial resolution of the estimate appears comparable to the estimate created with 50 speckle fields. In contrast, the letters ‘S’ and ‘P’ in the estimate created with 50 speckle fields are clearer compared to the single estimate created with a single speckle field.

The regularization parameter  $\beta$  was chosen by trial and error such that the estimate shows least speckle artifacts and “visually best” axial resolution. Our choice is  $\beta = 0.3$  for the reconstructions in Fig. 4.5. Reconstructions obtained with other values of  $\beta$  are also shown in Fig. 4.6, to illustrate the effect of  $\beta$  on reconstructions.

Figure 4.7 shows another experiment. In the experiment, we placed letters ‘LA-

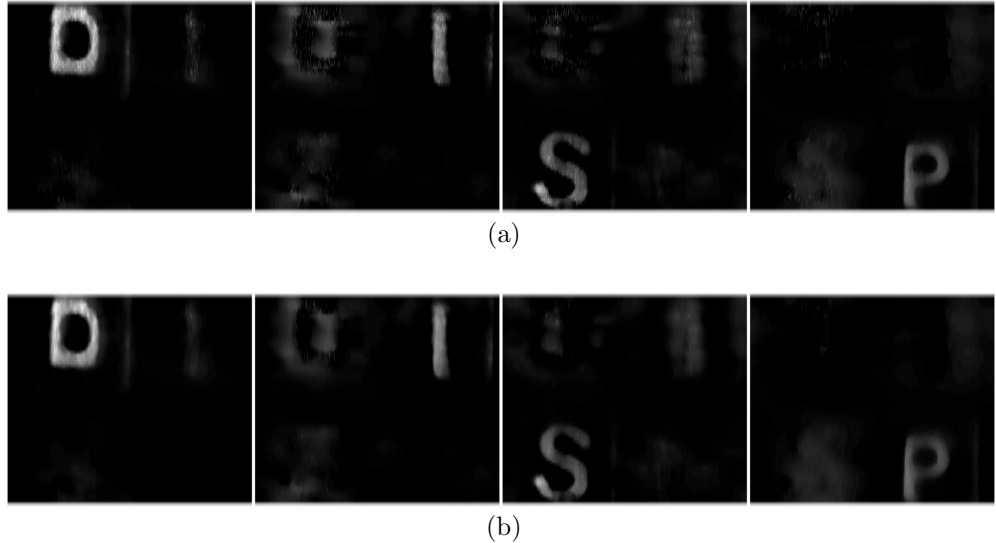
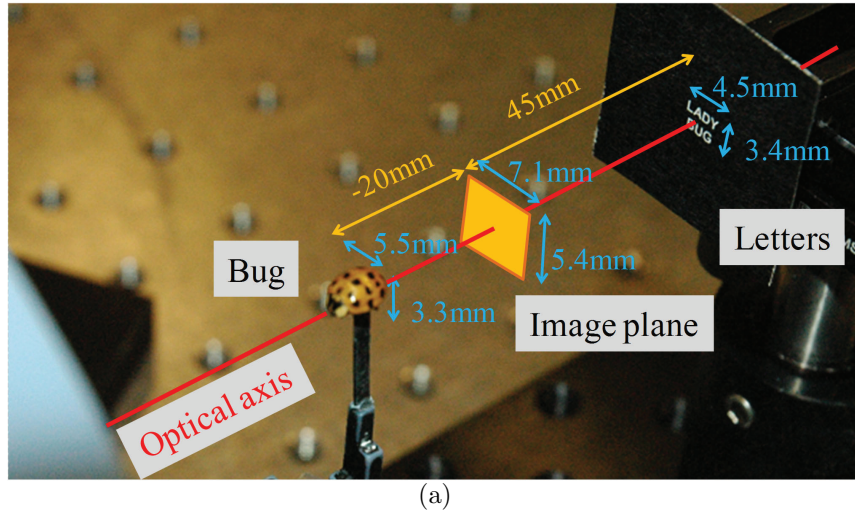
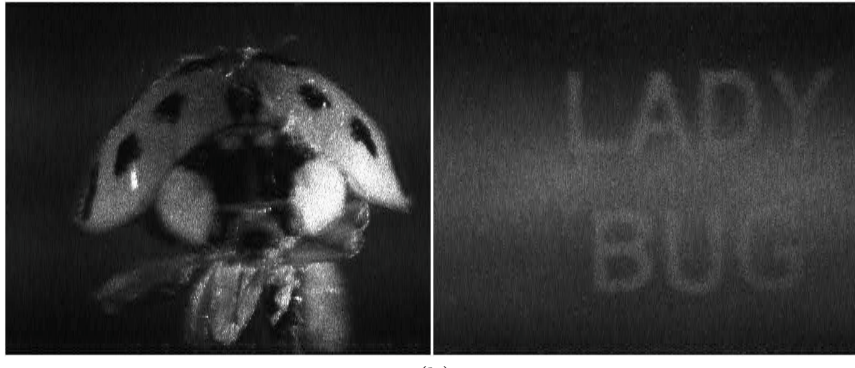


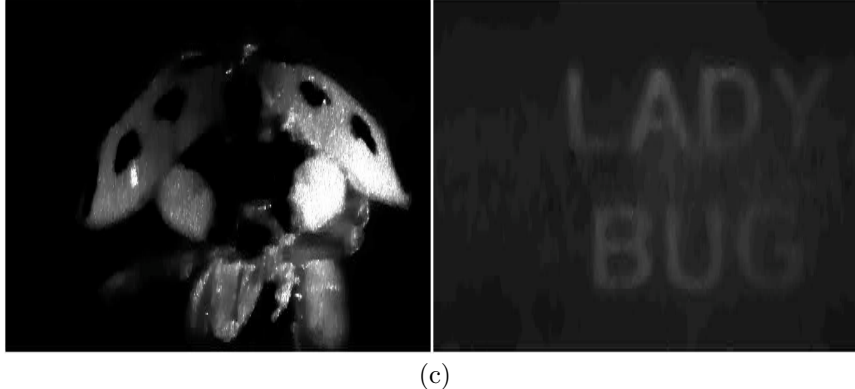
FIGURE 4.6: The reconstructions with (a)  $\beta = 0.1$  and (b)  $\beta = 0.2$ .



(a)



(b)



(c)

FIGURE 4.7: (a) A photograph of the objects: a real ladybug in front and letters 'LADYBUG' in the back with their dimensions; the yellow rectangle shows the location of the in-focus plane, (b) the average image of the backpropagation intensities of 20 speckle fields, and (c) our reconstruction obtained by solving Eq. (4.10).

DYBUG' directly behind a real ladybug in the axial direction. Fig. 4.7(b) shows the averaged intensity of the backpropagations created with 20 object speckle fields. The wings of the real ladybug show speckle artifacts, and the letters 'LADYBUG' are disguised in the blurs of the real ladybug. Fig. 4.7(c) shows an estimate obtained by solving Eq. (4.10). The surfaces of the wings become smoother. In particular, image contrast has been improved, as illustrated by the black spots on the wings. Also, the blurs placed on the letters have been reduced, while the letters become smoother. Readers may notice, however, that some of the features appear lost around the center of the real ladybug and in some part of the letters as well. We found some scattered lights were obscured by the object.

# 5

## High Pixel Count Holography

This chapter discusses scanning-based aperture synthesis and sparse aperture synthesis for high pixel count holography. Since scanning-based synthetic aperture holography synthesizes 12 by 12 scanned patches (1200 by 1200 pixels per patch), the synthesis confronts a multivariable global optimization problem for measurement errors estimation. The computational and optical co-design proposes a possible estimation method by localizing the measurement errors in time and space (Section 5.1). On the other hand, sparse aperture holography can synthesize a wide aperture using static measurement instead of dynamic scanning. To compensate the incomplete measurements of sparse aperture, incoherent image estimation is used for compressive reconstruction. The effect of compressive sparse aperture is discussed by some simulations in Section 5.2.

### 5.1 Scanning-based Synthetic Aperture Holography

#### 5.1.1 *Introduction*

Aperture synthesis is used to increase the resolution of coherent sensors [46]. Synthetic aperture holography has been studied using a scanning system in off-axis

digital holography. Two effects of scanning measurement complicate coherent aperture synthesis: subaperture registration errors and the relative phase instability of the reference field to the object field.

A cross-correlation method [47, 48] has been used to estimate the registration errors. The method basically conducts a similarity test on measurement overlap. Massig demonstrated improved resolution and reduced speckle sizes in the reconstructed image at a distance of 0.8 m [49]. In that study, a  $12.7 \times 12.7$  mm synthetic aperture was formed by scanning a  $6.4 \times 8.3$  mm sensor. Binet *et al.* presented a  $27.4 \times 1.7$  mm aperture synthesis by scanning a sensor with an effective area of  $1.7 \times 1.7$  mm at 1.5 m [50].

This research proposes an image-based method of coherent aperture synthesis on scanned images. An image-based metric, the sharpness metric [51], is used to estimate registration errors. The sharpness metric does not rely on any measurement overlap. Therefore, the image-based method is free from the change of speckle pattern [45] caused by phase instability. The measurement overlap is not necessary, so every measurement contributes to the improvement of image resolution.

Previous studies have accounted for phase instability by various methods. For example, Mico *et al.* synthesized nine measurements in a regular octagon geometry, improving resolution by a factor of 3 in digital holographic microscopy [52]. The phase instability was compensated by using phase factors up to the 2nd order that represent constant, linear, and quadratic phase error. Jiang *et al.* used the same phase factors for a  $25.9 \times 23.3$  mm aperture synthesis in digital Fresnel holography [53].

In this research, phase instability is mathematically analyzed and compensated. The mathematical model addresses phase instability by using spatial displacement of a point source that generates a wide reference field. The spatial displacement may be caused by experimental instability such as vibration, drift, and temperature

fluctuations. By correcting the displaced position of reference field, phase instability is alleviated in the object field. Thus, physical and concise representation of phase instability is possible in aperture synthesis.

The angular spectrum method [4, 28] supports mathematical modeling of phase instability. The angular spectrum method does not depend on Fresnel approximation, which is based on paraxial approximation in optics. Thus, the reference field can be accurately modeled for a large aperture synthesis.

A secondary camera is designed to monitor piston phase error as a kind of phase instability. Since piston phase error is parameterized in the optical measurement, the number of estimation variables decrease in the computational process. A specific scanning scheme also enables us to reduce the number of estimation variables in the computational domain.

A hierarchical strategy is adopted for computational estimation. The estimation process first solves the hologram patch errors within a block and again solves the hologram block errors between blocks within the synthetic aperture hologram. This strategy helps us efficiently break the large synthesis problem into small sub problems in the two steps.

The main result is a near diffraction-limited image synthesis achieving 60 micron resolution over a 63.4 mm field at a range of 2 meters. The hologram size is equivalent to  $14400 \times 14400$  pixels. This lensless imaging enables us to achieve a thin imager for a large synthetic aperture.

Depth imaging is also demonstrated by numerically focusing the image-based synthetic aperture hologram. The phase information of the field is recorded and processed [27, 54]. So, numerical focus axially forms the object image at a desired depth.

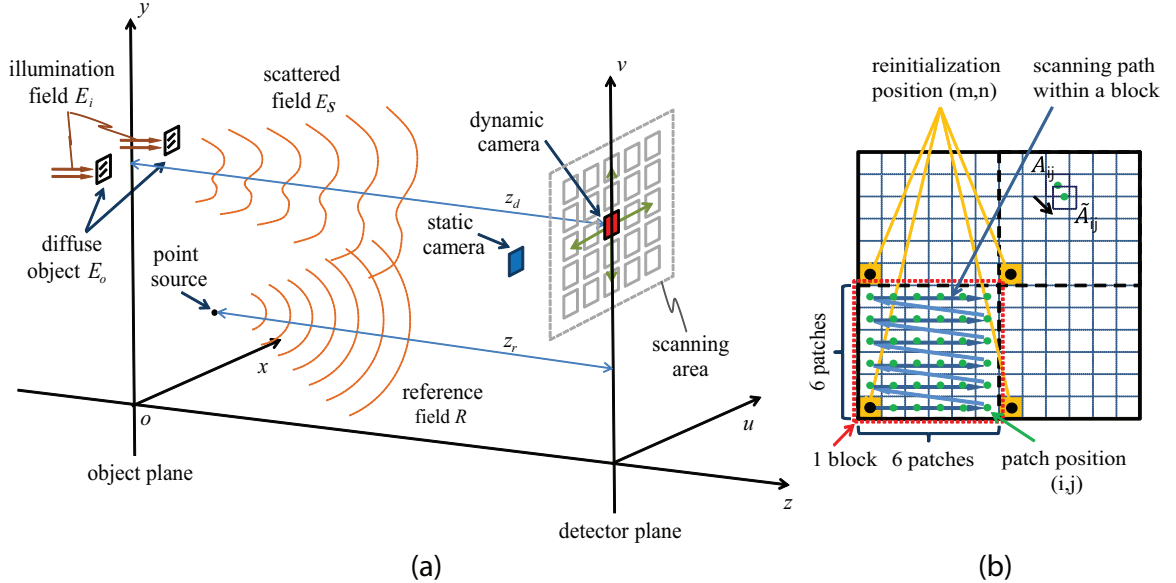


FIGURE 5.1: Schematic for image-based synthetic aperture holography: (a) scattered field  $E_s$  and reference field  $R$  form a hologram in the detector plane by propagating the distances,  $z_d$  and  $z_r$ , respectively, and (b) dynamic camera scans patch by patch within a reinitialized block. Note that  $\tilde{A}_{ij}$  describes the error-impacted measurement of a measurement subset  $A_{ij}$ .

### 5.1.2 Problem formulation

Figure 5.1 shows a simplified schematic of the measurement process. *Object plane* and *detector plane* are defined with the spatial coordinates of  $(x, y)$  and  $(u, v)$ , respectively. Also,  $z_d$  and  $z_r$  denote the ranges of the object and the reference point from the detector array along the optical axis. A *hologram patch* indicates a measurement of scanning aperture. A *hologram block* is composed of the hologram patches, and a *wide aperture (WA) hologram* is a collection of the hologram blocks. A symbol  $A$  denotes the set of spatial coordinates of all locations in the area of the synthetic aperture as shown in Fig. 5.1(b). The  $A$  is partitioned into  $I \times J$  subsets, where  $A_{ij}$  denotes the  $(i, j)$ -th subset of  $A$ :  $\bigcup_{ij} A_{ij} = A$ .

An illumination field is incident on a diffuse object confined in a field of view (FOV) and creates a field scattered off the object. The incident field and the object

field are denoted by  $E_i(x, y)$  and  $E_o(x, y)$ , respectively. A point source is located below the object to create a reference field  $R(x, y)$ . The object field  $E_o(x, y)$  propagates to the detector plane and creates a field  $E_s(u, v; z_d)$  incident on focal plane array (FPA). Also, the reference field  $R(x, y)$  propagates to the detector plane and creates a propagated reference field  $R(u, v; z_r)$ . The fields  $E_o(x, y)$  and  $E_s(u, v; z_d)$  are related by

$$E_s(u, v; z_d) = (E_o \circledast h)(u, v; z_d) = \iint E_o(x, y)h(u - x, v - y; z_d)dx dy, \quad (5.1)$$

where  $\circledast$  denotes a 2D convolution operator, and  $h$  denotes the point spread function (PSF) [28] given by

$$h(u, v; z) = \left[ \frac{-jz/\lambda}{z^2 + u^2 + v^2} + \frac{z/2\pi}{(z^2 + u^2 + v^2)^{3/2}} \right] e^{j\frac{2\pi}{\lambda}\sqrt{z^2 + u^2 + v^2}}, \quad (5.2)$$

whose 2D Fourier transform (FT) is the angular spectrum transfer function [28]:

$$\mathcal{F}\{h(u, v; z)\} = e^{j\frac{2\pi z}{\lambda}\sqrt{1-(\lambda f_u)^2-(\lambda f_v)^2}}. \quad (5.3)$$

Propagated fields  $E_s(u, v; z_d)$  and  $R(u, v; z_r)$  form an interference pattern on the detector plane whose intensity is given by

$$I(u, v; z_d, z_r) = |R(u, v; z_r) + E_s(u, v; z_d)|^2, \quad (5.4)$$

whose partition is measured by scanning the FPA.

Ideally, once the interference intensity measurements  $I^{ij}(u, v; z_d, z_r)$  for all  $i$  and  $j$  are collected, we can register them together by placing in the positions according to the  $A_{ij}$  as shown in Fig. 5.1(b). By doing so, we can synthesize the full synthetic aperture intensity. Then a typical holographic filtering process [4] can be performed to extract the scattered field  $E_s(u, v; z_d)$ , which can then be backpropagated by using an adjoint operator to form a coherent image of the object field  $E_o(x, y)$ .

However, in real experiments, creating a synthetic aperture hologram can involve various errors that will degrade the reconstructed image resolution. These errors are described, modeled, and analyzed in the following subsections.

#### *Error sources*

In synthetic aperture holography, a large diffracted optical field scattered off a 2D object is measured in many hologram patches, each of which is measured with a FPA by moving it to a designated position and then pausing it for a few seconds to allow for the vibration to cease, and then repeating at the next position. This process takes an amount of time and space in linear proportion to the number of hologram patches. Therefore, there can be temporal and spatial changes, causing several different errors in the measurements from one hologram patch to another.

While there are many types of errors, we are mostly concerned about the following:

- 1) *Piston phase errors*: unknown changes in the constant phase of the interference intensity measurements  $I^{ij}(u, v; z_d, z_r)$ ,
- 2) *Detector registration errors*: unknown errors in the exact positions of  $I^{ij}(u, v; z_d, z_r)$  caused by the inaccuracy of the 2D translation stage that scans the FPA,
- 3) *Reference field errors*: unknown relative changes in the position of the reference field to the object field, which may be caused by the experimental instability (e.g. vibration and temperature fluctuations),
- 4) *Reference field discrepancy*: unknown discrepancy in the phase of the reference field caused by the non-ideal generation of the spherical field.

### Mathematical modeling of errors

The ideal interference intensity measurement  $I^{ij}(u, v; z_d, z_r)$  is captured by placing the sensor array at the (i,j)-th position as shown in Fig. 5.1(b). It consists of the reference and scattered field,  $R^{ij}(u, v; z_r)$  and  $E_s^{ij}(u, v; z_d)$ , and can be expressed as

$$I^{ij}(u, v; z_d, z_r) = |R^{ij}(u, v; z_r) + E_s^{ij}(u, v; z_d)|^2, \quad (u, v) \in A_{ij} \quad (5.5)$$

$$\begin{aligned} &= |R^{ij}(u, v; z_r)|^2 + |E_s^{ij}(u, v; z_d)|^2 \\ &\quad + R^{*,ij}(u, v; z_r)E_s^{ij}(u, v; z_d) + R^{ij}(u, v; z_r)E_s^{*,ij}(u, v; z_d), \end{aligned} \quad (5.6)$$

where the superscript ‘\*’ denotes a complex conjugate. Applying Fourier filtering to Eq. (5.6), the (i,j)-th field measurement  $D^{ij}(u, v; z_d, z_r) = R^{*,ij}(u, v; z_r)E_s^{ij}(u, v; z_d)$  is obtained.

If considering the errors described above, the errors-impacted field measurement  $\tilde{D}^{ij}(u, v; z_d, z_r)$  is re-defined by

$$\begin{aligned} \tilde{D}^{ij}(u, v; z_d, z_r) &= D^{ij}(u, v; z_d, z_r; \theta_e^{ij}) \\ &= e^{-j\phi_c^{ij}} \tilde{R}^{*,ij}(u, v; z_r) \tilde{E}_s^{ij}(u, v; z_d) e^{-j\phi_r^{ij}(u, v)}. \end{aligned} \quad (5.7)$$

Error parameters vector is defined as  $\theta_e^{ij} = [\phi_c^{ij}, e_d^{ij}, e_t^{ij}, \phi_r^{ij}(u, v)]^T$  with the superscript ‘T’ denoting a transpose:  $\phi_c^{ij}$  indicate the piston phase errors in error source 1,  $e_d^{ij}$  indicate the detector registration errors in error source 2,  $e_t^{ij}$  indicate transverse errors of the detector registration errors in error source 2 and the reference field errors in error source 3, and  $\phi_r^{ij}(u, v)$  indicate the reference field discrepancy in source 4.

The inaccurate reference field  $\tilde{R}^{ij}(u, v; z_r)$  and the inaccurate scattered field

$\tilde{E}_s^{ij}(u, v; z_d)$  may be expressed using the PSF [28],

$$\begin{aligned}\tilde{R}^{ij}(u, v; z_r) &= h(u, v; z_r) \circledast \delta(u + e_{d,u}^{ij} + e_{f,u}^{ij}, v + e_{d,v}^{ij} + e_{f,v}^{ij}; z_r) \\ &= h(u, v; z_r) \circledast \delta(u + e_{t,u}^{ij}, v + e_{t,v}^{ij}; z_r)\end{aligned}\quad (5.8)$$

$$\begin{aligned}\tilde{E}_s^{ij}(u, v; z_d) &= E_s^{ij}(u + e_{d,u}^{ij}, v + e_{d,v}^{ij}; z_d) \\ &= [E_i(x, y)E_o(x, y)] \circledast h(u, v; z_d) \circledast \delta(u + e_{d,u}^{ij}, v + e_{d,v}^{ij}; z_d).\end{aligned}\quad (5.9)$$

Here the reference field  $\tilde{R}^{ij}(u, v; z_r)$  is impacted by the transverse error  $e_t^{ij} = (e_{t,u}^{ij}, e_{t,v}^{ij})$ , which is a combination of the detector registration error  $e_d^{ij}(u, v; z_d) = (e_{d,u}^{ij}, e_{d,v}^{ij})$  and the reference field error  $e_f^{ij}(u, v; z_r) = (e_{f,u}^{ij}, e_{f,v}^{ij})$ . The scattered field  $\tilde{E}_s^{ij}(u, v; z_d)$  is impacted by the detector error  $e_d^{ij}(u, v; z_d)$ . Note that the depth error of hologram patch is not considered in this error model. This is justified by the fact that the depth resolution in optical axis is large enough that the effect of the axial displacement is negligible.

### 5.1.3 Computational design

Fig. 5.2 shows the flow chart of estimation processes for WA hologram synthesis. After the piston phase errors compensation, the error parameters vector becomes

$$\theta_e^{ij} = [e_{dp}^{ij}, e_{db}^{ij}, e_t^{ij}, \phi_r^{ij}(u, v)]^T,\quad (5.10)$$

where the detector registration errors  $e_d^{ij}(u, v; z_d)$  are split into patch errors  $e_{dp}^{ij}(u, v; z_d)$  and block errors  $e_{db}^{ij}(u, v; z_d)$ . Estimating the errors  $e_{dp}^{ij}(u, v; z_d)$  in hologram block synthesis, the errors  $e_{db}^{ij}(u, v; z_d)$  are left which is constant for  $i, j \in B_{mn}$  where  $B_{mn}$  is the set of all indices i and j for the (m,n)-th block. Thus the error parameters vector becomes,

$$\theta_e^{ij} = [e_{db}^{ij}, e_t^{ij}, \phi_r^{ij}(u, v)]^T.\quad (5.11)$$

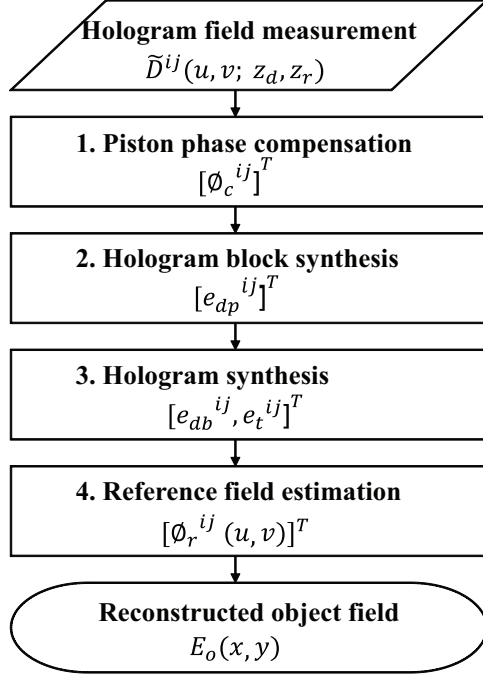


FIGURE 5.2: Flow chart of the error estimation processes for image-based synthetic aperture holography. The estimated errors are denoted in the processes.

WA hologram synthesis (subsection 3.3) makes the error parameters vector become,

$$\theta_e^{ij} = [\phi_r^{ij}(u, v)]^T. \quad (5.12)$$

Finally, the reference field discrepancy  $\phi_r^{ij}(u, v)$  is estimated in reference field estimation.

#### *Piston phase compensation*

A secondary camera is used to eliminate the piston phase errors  $\phi_c^{ij}$  in the measurement. The secondary FPA is set up to monitor the piston phase fluctuations of WA hologram field. The piston phase errors  $\phi_c^{ij}$  are given by,

$$\phi_c^{ij} = \text{angle} \left\{ \sum_{uv} \text{sign} \left\{ s^{ij}(u, v)/s^{11}(u, v) \right\} \right\}, \quad (5.13)$$

where  $s^{ij}(u, v)$  indicates the complex hologram image in the (i,j)-th hologram patch. To figure out the relative field variation to the first hologram image,  $s^{ij}(u, v)$  is

divided by  $s^{11}(u, v)$  in exponential form. The MATLAB function `sign` avoids the phase variation from being affected by phase wrapping problem. The MATLAB function `angle` returns the phase angles, in radians, of complex elements.

#### *Hologram block synthesis (hologram patch based process)*

Recall that a hologram block is defined as a specified group of WA hologram. We alleviate the detector registration errors by registering hologram patches in each block, by shifting the patches by a few pixels that will be estimated. Since the reference field change is negligible within a hologram block (meaning that the associated errors are constants in a block), the detector registration errors mainly degrade the hologram synthesis.

The object field  $E_o^{mn}(x, y)$  is backpropagated using the angular spectrum method [4] from the corrected field measurement  $\tilde{D}^{ij}(u - e_{dp,u}^{ij}, v - e_{dp,v}^{ij}; z_d, z_r)$ , where  $i = 1, \dots, I$  and  $j = 1, \dots, J$ . The (i,j)-th hologram patch is defined in the (m,n)-th hologram block.

$$E_o^{mn}(x, y; e_{dp,u}, e_{dp,v}) = \mathcal{F}^{-1}\{\mathcal{F}\{R^{mn}(u, v; z_r)$$
(5.14)

$$\times \tilde{D}^{mn}(u - e_{dp,u}, v - e_{dp,v}; z_d, z_r)\}e^{-jz_d\sqrt{k^2 - k_u^2 - k_v^2}},$$

where  $R^{mn}(u, v; z_r)$  is the numerically generated spherical field with the hologram block size. The backpropagated field image is evaluated using the sharpness metric [55] which is expressed as,

$$\Omega_{SM}(e_{dp}) = \sum_{xy \in G} I(x, y; e_{dp})^{0.5},$$
(5.15)

$$e_{dp} = [e_{dp,u}^{11}, e_{dp,v}^{11}, \dots, e_{dp,u}^{IJ}, e_{dp,v}^{IJ}]^T,$$
(5.16)

where the image intensity is defined as  $I(x, y; e_{dp,u}, e_{dp,v}) = E_o^{mn}(x, y) \cdot E_o^{*,mn}(x, y)$  and  $G$  is the set of coordinate for the area containing guiding features. The sharpness

metric enforces the concentration of energy at few points distinguishing real image from plausible images. The detector registration errors in the hologram patches are estimated and corrected by minimizing the sharpness metric  $\Omega_{SM}(e_{dp})$  on the guiding feature images,

$$\hat{e}_{dp} = \arg \min_{e_{dp}} \Omega_{SM}(e_{dp}). \quad (5.17)$$

#### *Hologram synthesis (hologram block based process)*

After the hologram block synthesis, we estimate the detector registration errors and the reference field errors in hologram blocks. Both the errors are dominant in the WA hologram synthesis because the hologram blocks suffer from the phase instability and the registration errors.

The block (say  $B_k$ ) is denoted in the m-th row and in the n-th column of the matrix of the blocks. The detector registration errors in hologram blocks are defined as  $e_{db}^{mn} = (e_{db,u}^{mn}, e_{db,v}^{mn})$ , where  $m = 1, \dots, M$  and  $n = 1, \dots, N$ . Then the WA hologram field measurement is expressed by summing the estimated hologram blocks  $D^{mn}(u, v; z_d, z_r)$ ,

$$D(u, v; z_d, z_r) = \sum_{mn} \tilde{D}^{mn}(u - e_{db,u}^{mn}, v - e_{db,v}^{mn}; z_d, z_r). \quad (5.18)$$

The transverse errors in the hologram blocks,  $e_t^{mn} = (e_{t,u}^{mn}, e_{t,v}^{mn}) \forall i, j \in B_{mn}$ , are also considered. The estimated WA reference field is expressed by,

$$R(u, v; z_r) = \sum_{mn} \tilde{R}^{mn}(u - e_{t,u}^{mn}, v - e_{t,v}^{mn}; z_r). \quad (5.19)$$

The estimated scattered field  $\mathbf{E}_s(u, v; z_d)$  is obtained by multiplying the estimated WA hologram field measurement by the estimated WA hologram reference field,

$$\begin{aligned} \mathbf{E}_s(u, v; e_{db,u}, e_{db,v}, e_{t,u}, e_{t,v}) &= \tilde{R}(u - e_{t,u}, v - e_{t,v}; z_r) \\ &\times \tilde{D}(u - e_{db,u}, v - e_{db,v}; z_d, z_r) \end{aligned} \quad (5.20)$$

Then the estimated WA object field  $\mathbf{E}_o(x, y)$  is obtained by using the backpropagation method,

$$\begin{aligned}\mathbf{E}_o(x, y; e_{db,u}, e_{db,v}, e_{t,u}, e_{t,v}) &= \mathcal{F}^{-1}\{\mathcal{F}\{\mathbf{E}_s(u, v; e_{db,u}, e_{db,v}, e_{t,u}, e_{t,v})\} \\ &\quad \times e^{-jz_d\sqrt{k^2-k_u^2-k_v^2}}\}.\end{aligned}\quad (5.21)$$

To evaluate the errors  $e_{db,r} = (e_{db,u}, e_{db,v}, e_{t,u}, e_{t,v})$ , we again use the sharpness metric [55] on the guiding feature images,

$$\Omega_{SM}(e_{db,r}) = \sum_{xy \in G} I(x, y; e_{db,r})^{0.5}, \quad (5.22)$$

$$e_{db,r} = [e_{db,u}^{11}, e_{db,v}^{11}, e_{t,u}^{11}, e_{t,v}^{11}, \dots, e_{db,u}^{MN}, e_{db,v}^{MN}, e_{t,u}^{MN}, e_{t,v}^{MN}]^T. \quad (5.23)$$

Thus, the estimation is performed as,

$$\hat{e}_{db,r} = \arg \min_{e_{db,r}} \Omega_{SM}(e_{db,r}). \quad (5.24)$$

### *Reference field estimation*

Since the hologram synthesis came through the error estimation processes, only reference field discrepancy is left. To generate a phase estimate, 2D Chebyshev polynomials are used. The 2D Chebyshev polynomials need fewer polynomial terms to express the 2D rectangular aperture than Zernike polynomials. The phase estimate has the form

$$\phi_r(u, v; C_k) = \sum_k C_k P_k(u, v), \quad (5.25)$$

where  $P_k(u, v)$  and  $C_k$  are Chebyshev basis function and coefficient, respectively. Here the Chebyshev polynomials of the first kind are used up to 4th order (15 terms representing piston, tilt, focal shift, primary coma, and primary spherical phase error).

We multiply the phase estimate by the estimated scattered field  $\mathbf{E}_s(u, v; z_d)$ . Then the phase estimation is performed by minimizing the sharpness metric on the guiding feature images. The estimated WA object field  $\mathbf{E}_o(x, y)$  is obtained by using the backpropagation method,

$$\mathbf{E}_o(x, y; C_k) = \mathcal{F}^{-1} \left\{ \mathcal{F} \left\{ e^{-j\phi_r(u, v)} \mathbf{E}_s(u, v; z_d) \right\} e^{-jz_d \sqrt{k^2 - k_u^2 - k_v^2}} \right\}. \quad (5.26)$$

The sharpness metric [55] is again,

$$\Omega_{SM}(C_k) = \sum_{xy \in G} I(x, y; C_k)^{0.5}, \quad (5.27)$$

Finally, the estimation is,

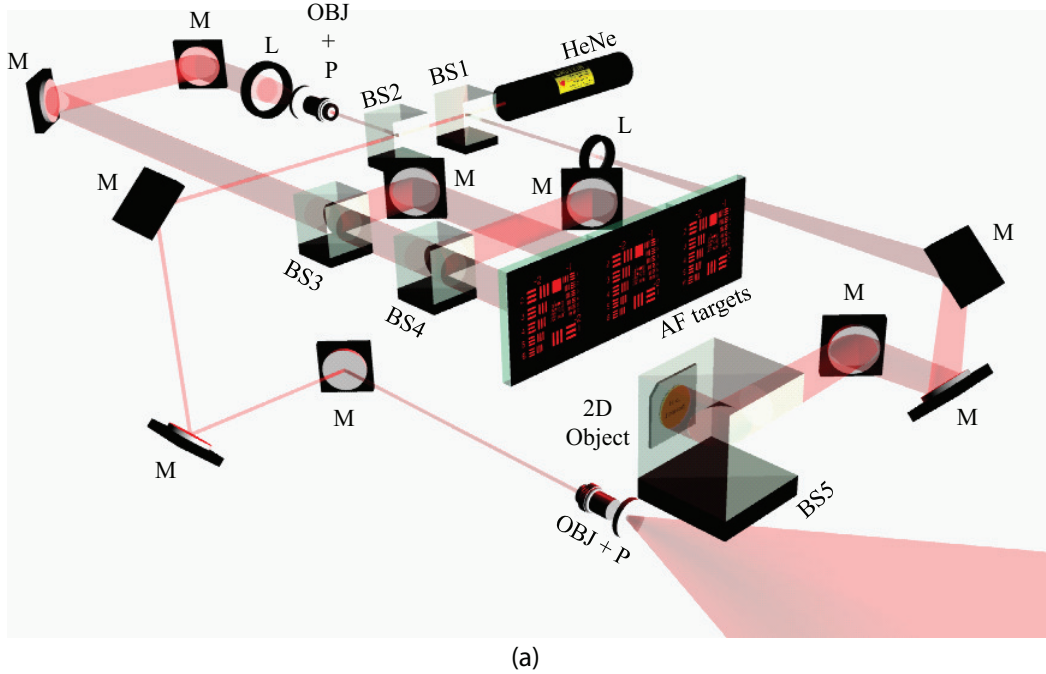
$$\hat{C}_k = \arg \min_{C_k} \Omega_{SM}(C_k), \quad (5.28)$$

where the estimation starts with the initial phase coefficients of zeros.

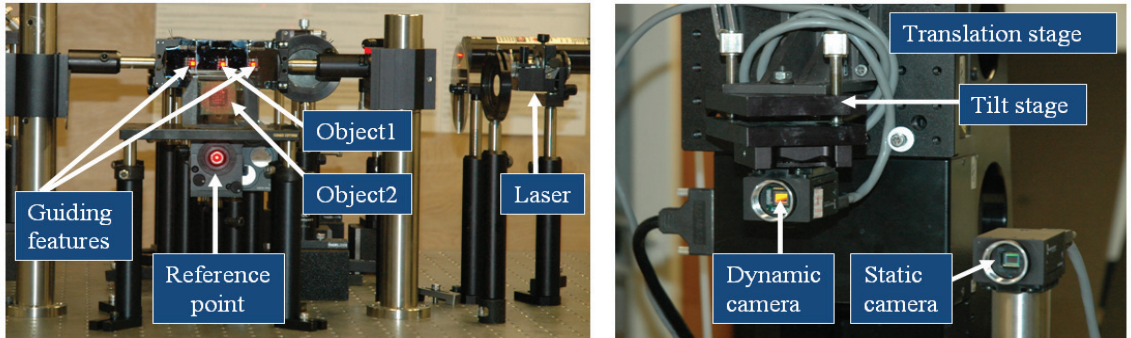
#### 5.1.4 Optical design

We designed our experiment to demonstrate coherent aperture synthesis in digital holography. The optical setup is composed of field generation and detection. In the field generation, three beams were used for the experiment: two beams were for the object and reference illumination of off-axis holography, and the other beam was for the guiding features illumination of image-based synthetic aperture holography. A HeNe laser with the wavelength of 633nm and the power of 20 mW was used to make a monochromatic light source for hologram measurement as shown in Fig. 5.3. The laser beam was split by beam splitters (BS1 and BS2) making two object and one reference beams.

In the reference beam, the two mirrors were used to step down the reference beam maintaining laser polarization perpendicular to the optical table. The polarization



(a)



(b)

FIGURE 5.3: Experimental setup: (a) the field generation consists of a HeNe (633 nm laser), M (mirrors), BS1–5 (beam splitters), AF (1951 USAF resolution target), OBJ+P (microscopic objective lens and pinhole), and L (lens), and (b) photographs of the field generation system (left) and the field detection system (right). Object 1 is a performance test object and Object 2 is a depth imaging object.

is one linear factor to determine the degree of optical coherence, so maintaining the polarization is critical for highly visible hologram measurement. Then the reference beam was guided by a mirror and spatially filtered by a  $25 \mu\text{m}$  pinhole and a 0.65 numerical aperture (NA) microscopic objective lens. The high NA microscopic ob-

jective lens generates a wide spherical field in the detector plane. Note the center of the reference field was vertically 100 mm lower than the center of the guiding features and axially 2.032 m (within  $\pm 2$  mm accuracy) away from the surface of FPA.

In the object beam of the guiding features, the beam after the beam splitter (BS2) was filtered and collimated using a microscopic objective lens, a pinhole and a f/3 lens to illuminate the 2D object features. The filtered/expanded beam was also split into three illumination beams of the guiding features by two beam splitters (BS3 and BS4). In the other object beam of the target object, the beam split by a beam splitter (BS1) was guided to illuminate the target object using a 2 inch beam splitter (BS5). A lens (L) diverged the beam to illuminate the full size of the target object. Therefore, the generated object and reference fields interfere, forming a hologram field in the detector plane.

A 1951 USAF resolution target (AF target) was used as the 2D guiding features, quantifying our estimation process in terms of image resolution. A diffuser inserted in the back side of the AF target scatters the field more uniformly spread with speckle patterns. Fig. 5.3 shows three AF targets in total: two AF targets at the sides were used for the guiding features and the other one at the center was used for the test object of the hologram synthesis. Note that the axial position of the guiding features are 2.034 m (within  $\pm 2$  mm accuracy) away from the surface of FPA and 2 mm away from the reference point source. The individual AF targets were horizontally placed 30 mm away in the same object plane.

A reflective 2D object was added to show the depth imaging in the synthetic aperture holography. The computer CPU chip was placed 35 mm below the AF targets' vertical location and 1.99 m away from the surface of FPA in optical axis. The logo inscription of the CPU chip was illuminated with a beam size of 22 mm in diameter.

The theoretical resolution and FOV is determined by the number of pixels and

pixel pitch of the sensor array using Eq. (2.2) and Eq. (2.3). Our experiments use a pixel pitch of  $4.4 \mu\text{m}$ , corresponding to the monochrome CCD PointGrey GRAS-20S4M-C FPA. We use a square patch of  $1200 \times 1200$  pixels on the array, meaning that a single aperture hologram captures a  $5.28 \times 5.28 \text{ mm}$  aperture and a  $12 \times 12$  synthetic aperture captures a  $63.36 \times 63.36 \text{ mm}$  aperture. At the object range of 2 meters, the theoretical resolution and FOV are  $20 \mu\text{m}$  and  $288 \times 288 \text{ mm}$  (where  $N = 12 \text{ hologram patches} \times 1200 \text{ pixels/hologram patch}$ ).

In practice, the FOV is reduced to account for separation of the reference and object fields. In Fourier filtering for the off-axis holography, only one fourth of the total hologram bandwidth is used to avoid the effect of undesired signals. In the ASM, the effective resolution and the FOV are constant to the propagation range  $z$  (Eq. (2.5) and Eq. (2.6)). Thus, the effective FOV of the  $12 \times 12$  synthetic aperture holography becomes  $63.36 \times 63.36 \text{ mm}$  equivalent to the synthetic aperture size, and the effective image pixel resolution is  $4.4 \mu\text{m}$  equivalent to the pixel pitch of FPA. The angular spectrum method was used since the Fresnel approximation method is designed for the small FOV object at the center.

#### *Stereo camera system for piston phase compensation*

A stereo camera system is designed to compensate the piston phase errors for 144 hologram patches. One static camera is placed 50 mm away from the center of the hologram scanning area as shown in Fig. 5.1(a) (see also Fig. 5.3) to record the piston phase fluctuation of hologram field.

The piston phase fluctuation over time is a dominant phase instability in the scanning measurement. The effect of piston phase fluctuation is that the reconstructed images from the hologram patches can destructively combine, resulting in worse image resolution than theoretical resolution.

The idea of the stereo camera system is based on the assumption that the holo-

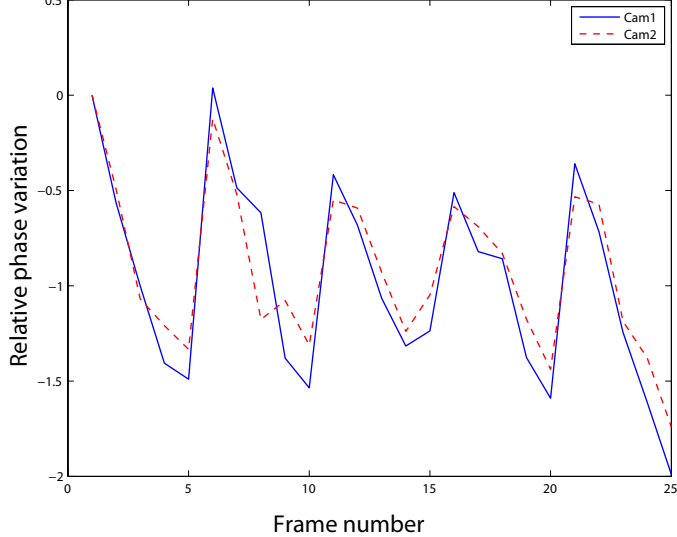


FIGURE 5.4: Piston phase correlation in two distant cameras: the red continuous line is the relative phase variation of camera 1 and the blue dotted line is the relative phase variation of camera 2.

gram field shares common phase fluctuations over the scanning area. Thus, the piston phase at two distant locations will be highly correlated such that the static camera can be used to estimate the piston phase fluctuations.

To verify the validity of this assumption, two cameras were fixed and tested. Both the cameras simultaneously took 25 image frames every two seconds. Using Eq. (5.13), the piston phase fluctuations were obtained in Fig. 5.4. The continuous red and dotted blue lines are the relative phase variations of camera 1 and camera 2 respectively. Both the line plots are shown to be strongly correlated over the frames.

#### *Reinitialization points scheme for hologram scanning*

A reinitialization points scheme uses a few initial measurement points for the individual blocks. So  $2 \times 2$  reinitialization points are set to measure 2D WA hologram area as shown in Fig. 5.1(b). The 2D WA hologram area is equivalent to  $12 \times 12$  hologram patches area without any overlap. The individual blocks are raster scanned starting from the reinitialization points and the hologram blocks are composed of  $6 \times 6$  holo-

gram patches. The number of hologram patches in one hologram block is determined such that the hologram block has only localized detector registration errors.

A scanning scheme of reinitialization points is designed to support the computational methods for hologram synthesis. Since the WA hologram is scanned block by block, the detector registration errors are dominant in the hologram patches within a block. For the WA hologram synthesis, we estimate the detector registration errors and the reference field errors. In the measurement, we used a 600mm 2D axis translation stage (Newport M-IMS600CC) specifying a mechanical resolution of  $1.25\text{ }\mu\text{m}$  and a bi-directional repeatability of  $1.0 - 2.5\text{ }\mu\text{m}$ . However, the guaranteed accuracy is  $15\text{ }\mu\text{m}$  and the inaccuracy linearly accumulates along the translation axis.

#### *5.1.5 Processes and results*

The data processing of image-based synthetic aperture holography followed the computational methods as described in Section 3. To process the WA hologram data ( $14400 \times 14400$  pixels), a Dell Precision T5500 was used with Intel Xeon CPU at 2.27 GHz, 48 GB RAM, and Windows7 64 bit operating system.

The processing time was dominantly taken by the hologram block synthesis, the WA hologram synthesis, and the reference field estimation. The hologram block synthesis searched the detection registration errors in a range of 5 pixels, minimizing the sharpness metric. The range was determined by the guaranteed accuracy  $15\mu\text{m}$  of the translation stage. To speed up the estimation of the hologram block, each row of the hologram block was considered to have identical detector registration errors. This is a reasonable assumption since the translation stage achieves bi-directional repeatability in the adjacent row measurement. So the detector registration errors were transversely searched for by sweeping the possible errors within the range for about one hour.

Both the WA hologram synthesis and the reference field estimation used un-

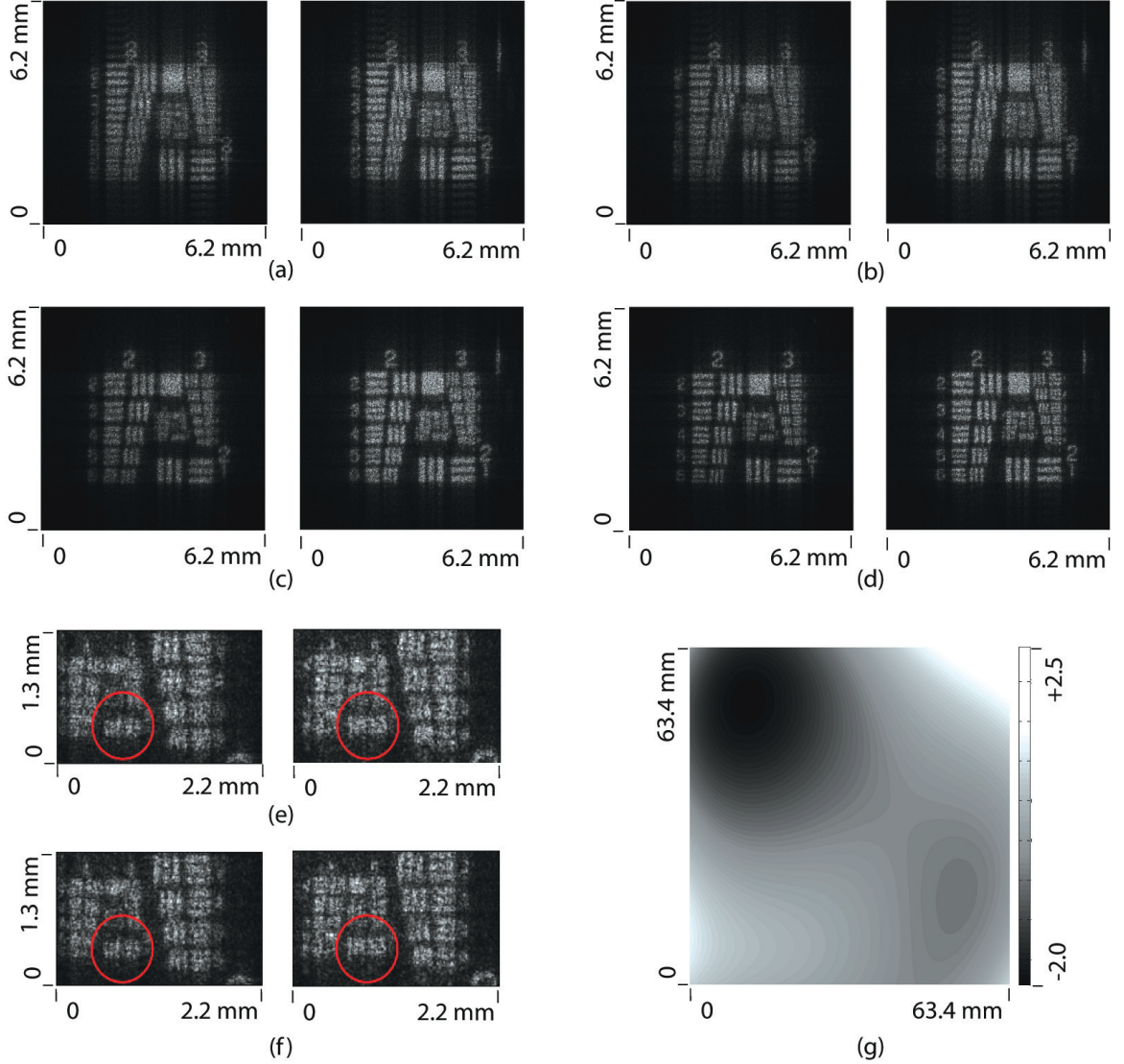


FIGURE 5.5: Evolution of estimation effects on the guiding features image: the left and right hand guiding features of (a) the raw data image, (b) the piston phase compensated image, (c) the hologram block synthesized image, (d) the WA hologram synthesized image, (e) the zoomed-in image of (d), and (f) the zoomed-in image of reference field estimated image. Also, (g) the estimated reference field discrepancy. Note that the image pixel resolution is  $4.4 \mu\text{m}$  in the angular spectrum method.

constrained multivariate minimum search in MATLAB. The algorithm utilizes the Quasi-Newton line search, which is stably convergent but slow. The WA hologram synthesis required about 4 hours for 5 iterations and the reference field estimation took about 6 hours for 5 iterations.

In the experiment, two transversely distant AF targets were used as the guiding features to avoid finding local minima in the estimation. Fig. 5.5 shows the evolution of estimation in the  $12 \times 12$  hologram patches. The raw data image suffers from all the errors  $\theta_e^{ij} = [\phi_c^{ij}, e_{dp}^{ij}, e_{db}^{ij}, e_t^{ij}, \phi_r^{ij}(u, v)]^T$ , resulting in the periodic ghost images and the blurs in Fig. 5.5(a). Compensating for the piston phase errors  $\phi_c^{ij}$ , the ghost images were effectively mitigated. However, the ghost images and the blurs still remain in Fig. 5.5(b). Estimating the detector patch errors  $e_{dp}^{ij}$ , the ghost images were removed in Fig. 5.5(c). Due to the blurs remaining in the image, the two AF targets resolve only the features (group 2, element 5) whose resolution correspond to  $158 \mu\text{m}$ .

In the WA hologram synthesis, the detector block errors and reference field errors in the hologram blocks  $[e_{db}^{ij}, e_t^{ij}]$  were estimated, resolving the features in group 3 in Fig. 5.5(d). Finally, the estimation of reference field discrepancy restores the resolution in the features (group 4, element1) that correspond to the theoretical resolution  $62.5 \mu\text{m}$  in Fig. 5.5(f). Also, Fig. 5.5(e) and (f) show the effect of the reference field discrepancy estimation on the zoomed-in images. The estimation helps to resolve the features (group 4, element1) that are marked by a red circle. The estimated phase of the reference field is shown in Fig. 5.5(g). Note that the theoretical resolution is calculated by multiplying the speckle factor of 3 by the theoretical resolution [28, 56].

Fig. 5.6 shows the evolution of image resolution to the number of hologram patches in the estimated guiding features. The image of the  $1 \times 1$  hologram patch barely resolves any feature (Group 2 and 3) in Fig. 5.6(a) and (d). The image of the  $3 \times 3$  hologram patches resolves the features (group 2, element 1) whose resolution corresponds to the theoretical resolution of  $250 \mu\text{m}$  in Fig. 5.6(b) and (e). The image of the  $12 \times 12$  hologram patch resolves the features (group 4, element 1) whose

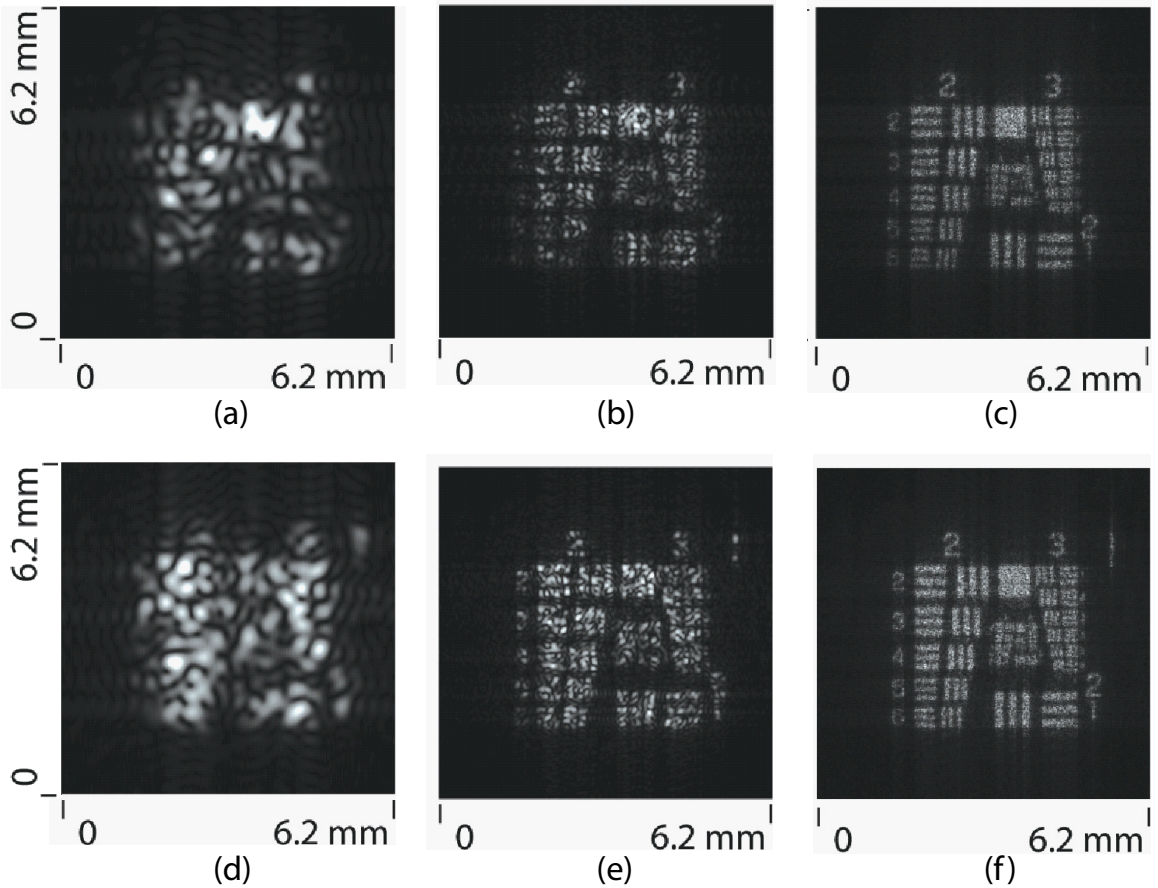


FIGURE 5.6: Resolution improvement to the number of hologram patches in the guiding features: (a), (b), and (c) show the images of  $1 \times 1$ ,  $3 \times 3$ , and  $12 \times 12$  hologram patches in the left-hand AF targets. Also, (d), (e), and (f) show the images of  $1 \times 1$ ,  $3 \times 3$ , and  $12 \times 12$  hologram patches in the right-hand AF targets.

resolution corresponds to the theoretical resolution  $62.5 \mu\text{m}$  in Fig. 5.6(c) and (f). Here we used the speckle-affected resolution [56].

Another experiment demonstrated the holographic images of three AF targets and one reflective 2D object. A full FOV image is shown with the  $63.4 \times 63.4 \text{ mm}$  aperture in Fig. 5.7), which is  $14400 \times 14400$  pixels imaging. In the figure, the CPU chip was numerically focused and the AF targets were not focused. The two AF targets at the sides were used as the guiding features to estimate the synthetic errors, and the CPU chip was an object for depth imaging. The two AF targets were

transversely separated by 60 mm on the same object plane.

Fig. 5.8 shows the images estimated by the hologram synthesis. Two AF targets at the sides (see Fig. 5.8(a) and (c)) were used for the guiding features, and the center one (Fig. 5.8(b)) was used for the performance test target. Unlike the non estimated images in Fig. 5.8(a) and (c), the estimated images in Fig. 5.8(d) and (f) have the ghost images and the blurs mitigated. In Fig. 5.8(e), the center AF target can also read the numbers in group 2. Thus, the estimation strategy using the guiding features is verified to be useful in the synthetic aperture holography. Unlike the images of Fig. 5.5, the resolution degradation is caused by the limit of the detector's dynamic range. The increased field signals easily saturate the dynamic range of the detector as the number of objects increases.

Fig. 5.9 shows the feasibility of depth imaging. The logo inscription of a CPU chip is in focus by backpropagating the estimated synthetic aperture hologram. The

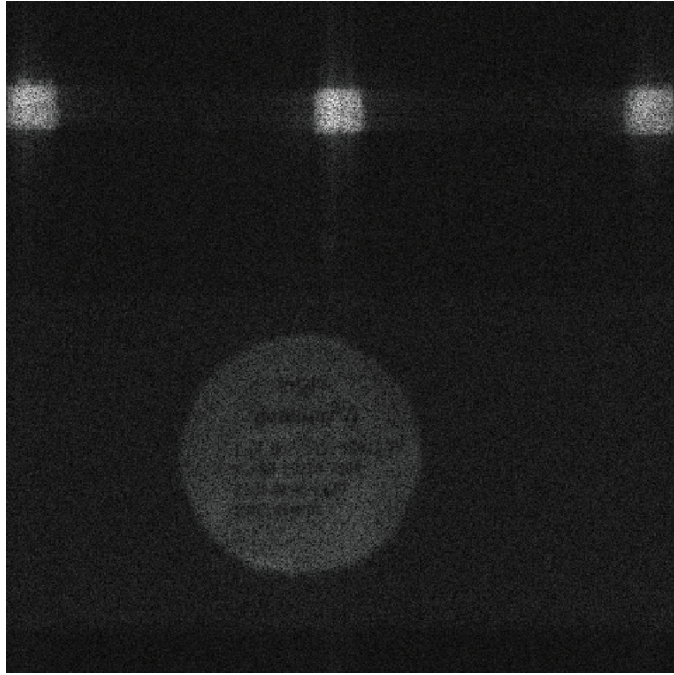


FIGURE 5.7: Full FOV image with  $63.4 \times 63.4$  mm aperture: the CPU chip was numerically focused and the AF targets were not focused.

resolution improvement to the number of hologram patches is presented in Fig. 5.9(a), (b), and (c). The more hologram patches we synthesize, the smaller letters are readable. Fig. 5.9(d) and (e) show the effect of error estimation on the in-focus image. The zoomed-in images have better sharpness in the estimated image in Fig. 5.9(e). Fig. 5.9(f) shows an incoherent base line image of the logo inscription.

In Fig. 5.10, the piston phase errors were monitored showing temporal drift over the 144 scanned hologram patches. The hologram block synthesis estimated the horizontal and vertical detector errors as  $e_{dp,u}^{ij} = 0$  and  $e_{dp,v}^{ij} = 1 - i$ , respectively (for  $m=1$  and  $n=1$ ). The other blocks showed the same detector errors with the

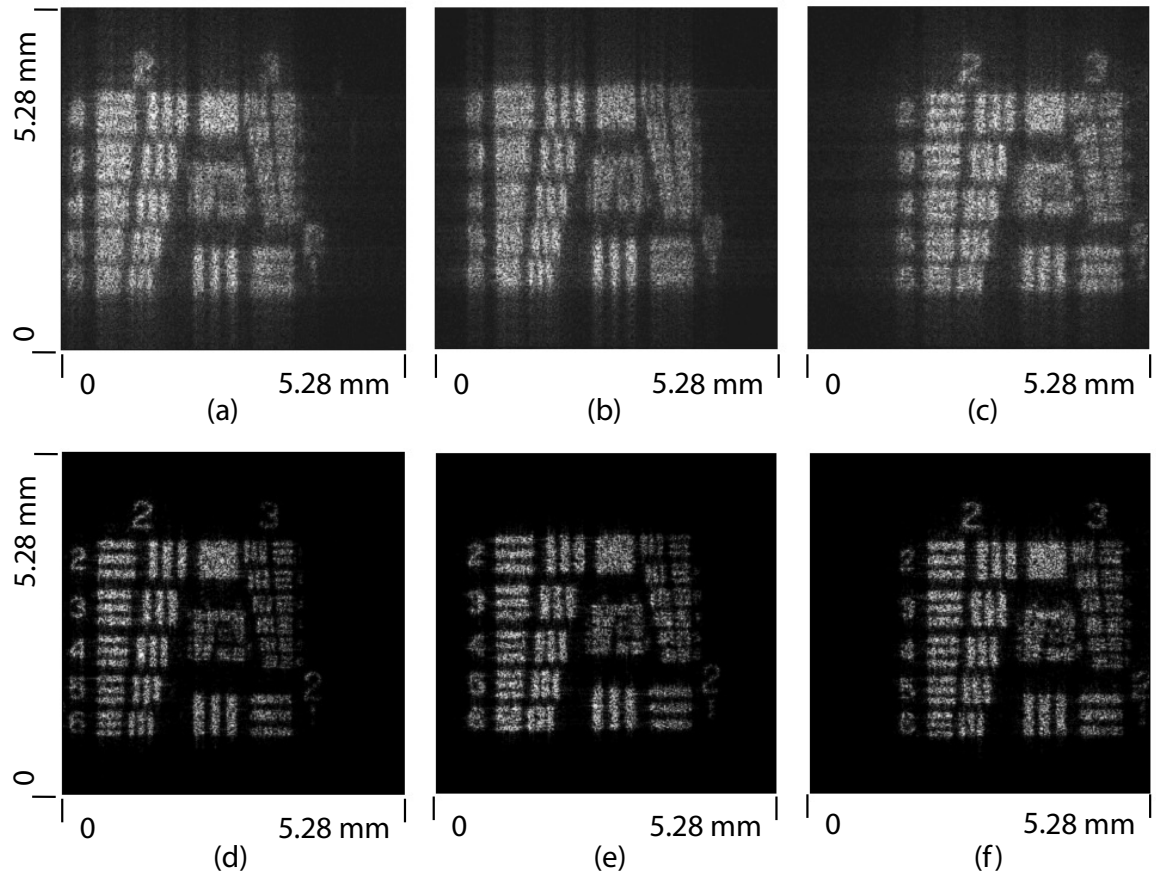


FIGURE 5.8: The images of the AF targets in the depth imaging experiment: (a) left-hand guiding features, (b) performance test features, and (c) right-hand guiding features of the raw data. Also, (d) left-hand guiding features, (e) performance test features, and (f) right-hand guiding features of the hologram synthesis.

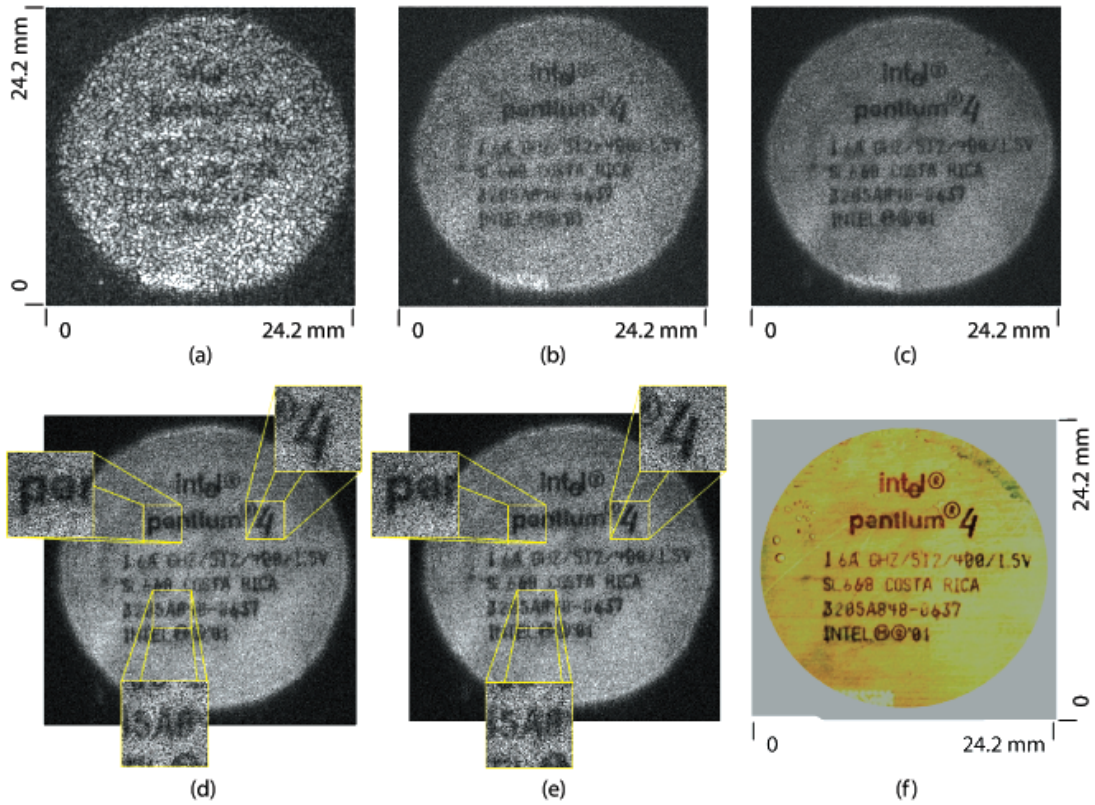


FIGURE 5.9: The image of the CPU chip: resolution improvement to the number of hologram patches showing the images of (a) the  $1 \times 1$  hologram patch, (b) the  $3 \times 3$  hologram patches, and (c) the  $12 \times 12$  hologram patches. Also, comparison of the images of (d) the un-synthesized hologram, (e) the synthesized hologram, and (f) the real photograph. Note that this object is placed 44 mm closer to the detector plane than the guiding features' plane.

hologram block of  $m=1$  and  $n=1$ . Table 5.1 shows the detector registration errors and reference field errors estimated for the hologram blocks. The estimates for the reference field discrepancy are shown in Table 5.2.

Table 5.1: The estimated parameters of the detector registration errors and the reference field errors for the WA hologram synthesis.

$e_{db,u}^{mn}$	$e_{db,u}^{11}$	$e_{db,u}^{12}$	$e_{db,u}^{21}$	$e_{db,u}^{22}$	$e_{db,v}^{mn}$	$e_{db,v}^{11}$	$e_{db,v}^{12}$	$e_{db,v}^{21}$	$e_{db,v}^{22}$
pixels	-1	-2	+3	0	pixels	-2	0	-1	+3
$e_{t,u}^{mn}$	$e_{t,u}^{11}$	$e_{t,u}^{12}$	$e_{t,u}^{21}$	$e_{t,u}^{22}$	$e_{t,v}^{mn}$	$e_{t,v}^{11}$	$e_{t,v}^{12}$	$e_{t,v}^{21}$	$e_{t,v}^{22}$
pixels	+2	+3	0	-3	pixels	-1	-2	+3	+1

Table 5.2: The Chebychev coefficients for the reference field discrepancy.

$C_k$	$C_0$	$C_1$	$C_2$	$C_3$	$C_4$	$C_5$	$C_6$	$C_7$
values	0.0000	0.3549	0.3305	0.2446	-0.6808	-0.0903	0.1009	-0.0957
$C_k$	$C_8$	$C_9$	$C_{10}$	$C_{11}$	$C_{12}$	$C_{13}$	$C_{14}$	
values	0.1398	0.0530	0.0797	-0.0528	0.0719	-0.2289	-0.1287	

## 5.2 Sparse Aperture Holography

### 5.2.1 Introduction

We consider sparse aperture holography which allows high pixel count 2D imaging without scanning. Mosaics of low cost 2D sensor arrays achieve large aperture digital holography of hundreds of mega pixel fields. The major challenges of scanning-based holography are subaperture registration errors and the relative phase instability of the reference field to the object field due to sources such as vibration and thermal fluctuation [57].

A sparse aperture can avoid a lengthy acquisition time as well as computational compensation for the phase instabilities. Synchronization of the sensors in a sparse

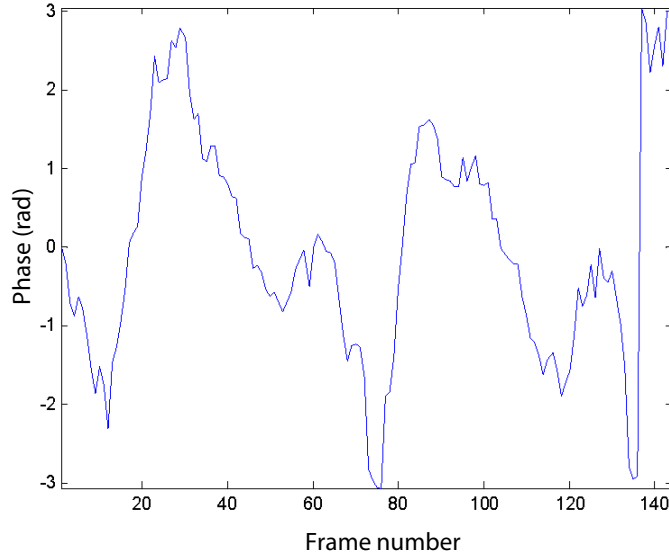


FIGURE 5.10: The monitored piston phase variation of scanned 144 hologram patches.

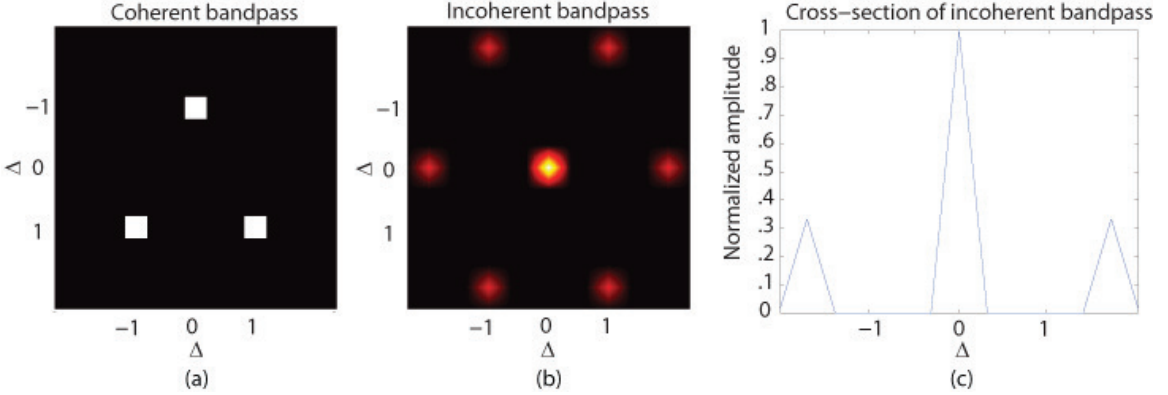


FIGURE 5.11: Coherent and incoherent bandpasses in sparse aperture design : (a) coherent bandpass, (b) incoherent bandpass, and (c) cross-section of incoherent bandpass. Note that  $\Delta$  is the space of subapertures.

aperture may enable snap-shot detection eliminating phase instability. Using spatially incoherent laser illumination enables incoherent synthesis of apertures and a corresponding enhancement of MTF support [4]. Radio telescopes employ the same techniques to measure a large MTF support with a sparse aperture [58]. In addition, incoherent image estimation eliminates the speckle problems common when reconstructing diffuse objects using holography.

We compare coherent and incoherent bandpasses in a sparse aperture system with three square apertures. The MTF is obtained by the autocorrelation of the transmittance of a sparse aperture [28]. Fig. 5.11.(b) shows that the MTF bands are located in the high frequencies, increasing the maximum frequency of the MTF. Thus, sparse aperture holography can detect higher frequency information than a single wide aperture system with equal detector area. While the loss of mid-band information can be problematic, compressive reconstruction is used to mitigate it.

Compressive reconstruction uses the incoherent image estimation supported by multiple speckle realizations. Decompressive inference can help alleviate the loss of some MTF support not sampled by the incoherent MTF by imposing sparsity constraints on an incoherent source or scatterer reconstruction, in a manner generalizing

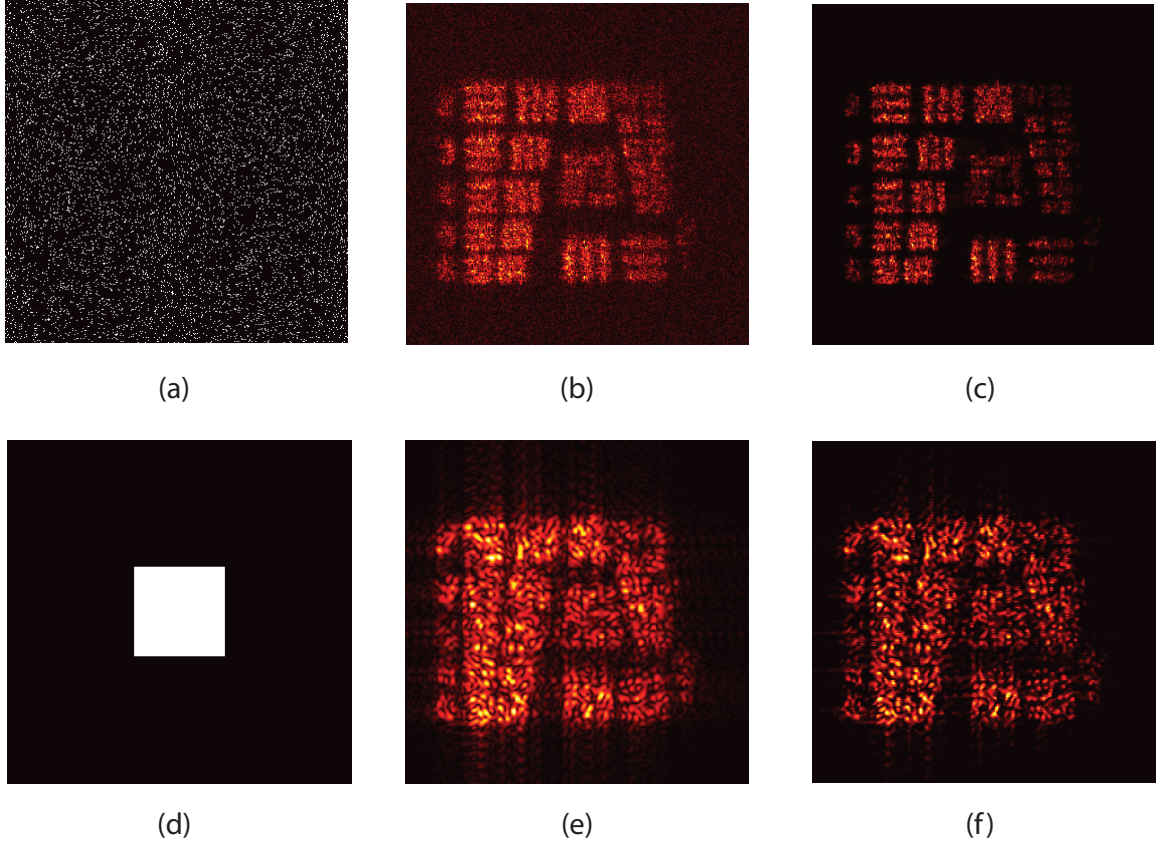


FIGURE 5.12: Feasibility of sparse aperture holography : (a) sparse aperture with 6.7 percent fill factor, (b) backpropagated field of sparse aperture, (c) compressive reconstruction of sparse aperture, (d) low-pass aperture with 6.7 percent fill factor, (e) backpropagated field of low-pass aperture, (f) compressive reconstruction of low-pass aperture.

methods like the CLEAN algorithm. [58]

### 5.2.2 The feasibility of sparse aperture holography

The effect of sparse aperture holography is tested with 63.4 by 63.4 mm synthetic aperture hologram of Section 5.1. Figure 5.12 shows the center AF targets processed from the sparse aperture and the low-pass aperture. The two apertures were applied to the scanning-based synthetic aperture by sampling the full synthetic aperture (207 Mega pixels) as designed in Fig. 5.12 (a) and (d). The sparse aperture was generated by Gaussian random probability with 6.7 percent opening as shown in Fig. 5.12 (a).

The backpropagated fields and the compressive reconstructions clearly show that the sparse aperture collects more information than the low-pass aperture with the same fill factor. Moreover, the compressive reconstructions show better contrast than the backpropagated fields. Therefore, the sparse aperture can be an efficient strategy for high pixel count holography. The feasibility test of sparse aperture holography was performed by the coherent image estimation and the effect of the incoherent image estimation is discussed next.

### 5.2.3 Sampling and processing w/ simulation

In this example, sparsity constraints on total variation decompressively localizes 2D structure alleviating the ambiguity of sparse measurement [35]. The simulation of sparse aperture holography is mostly similar to that of diffuse object tomography in Chapter 4. The codes are also given for the coherent estimation and the incoherent estimation (see Appendix C). A 2D phantom object is generated with  $2048 \times 2048$  pixels in 2 m range as shown in Fig. 5.13 (a). LU holography is used for lensless holographic imaging at the wavelength of  $0.633 \mu\text{m}$ . The pixel pitch is assumed to be  $25 \mu\text{m}$  in the measurement plane, avoiding the aliasing issue (see Appendix A) and achieving  $25 \mu\text{m}$  pixel resolution in the object plane.

In the Sparse Aperture Generation block, randomized distribution of the sparse aperture maximizes decompressive inference in the measurement plane. This design follows the coherence restriction between the measurements and the object basis for the high fidelity reconstruction. In remote imaging, scattered fields have a lot of information redundancy in the measurement plane because of field divergence. Individual apertures are designed to be point-like detectors to reduce the measurement redundancy, and the sparse distribution of point-like apertures may be supported by a phase mask in the optical domain. Fig. 5.13 (d) shows a sparse aperture design with a 16 percent fill factor.

In the Propagation Operators block, the FSASM is used to represent optical fields in the field range with compactness and reliability (see Section 2.3). Fig. 5.13 (b) and (e) compare the averaged backpropagations of the coherent image estimation and the incoherent image estimation, respectively. Fig. 5.13 (b) contains higher frequency features than Fig. 5.13 (e), because the incoherent image estimation expands the bandpass twice. Fig. 5.13 (c) and (f) also compare the compressive reconstructions of the coherent image estimation and the incoherent image estimation, respectively. The compressive reconstruction of the incoherent image estimation, Fig. 5.13 (c), is superior to that of the coherent image estimation, Fig. 5.13 (f), because of the expanded bandpass of the incoherent image estimation. Thus, the image of Fig. 5.13 (c) is speckle suppressed showing high resolution. The compressive reconstruction was performed by the TwIST algorithm.

Fig. 5.14 shows a patch-based sparse aperture design compared to the point-based sparse aperture design in Fig. 5.13. The patch-based sparse aperture can be more realistic than the point-like sparse aperture in terms of sparse aperture registration. While the compressive reconstruction of the incoherent image estimation shows the high frequency features in Fig. 5.14 (c), the compressive reconstruction of the coherent image estimation hardly show any high frequency features in Fig. 5.14 (f). Thus, compressive sparse aperture holography is still valid with the patch-based design.

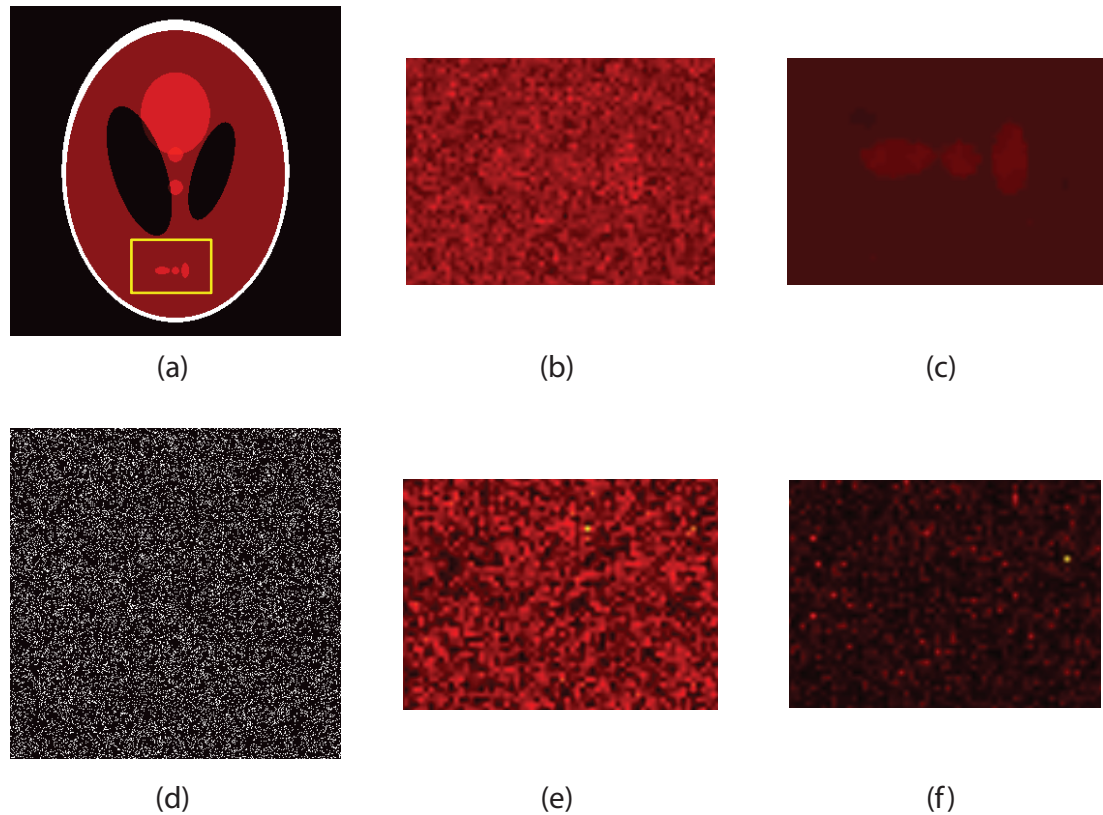


FIGURE 5.13: Point-based sparse aperture holography : (a) 2D object, (b) region of interest of backpropagated field in coherent estimation, (c) region of interest of compressive reconstruction in coherent estimation, (d) sparse aperture with 16 percent fill factor, (e) region of interest of backpropagated field in incoherent estimation, and (f) region of interest of compressive reconstruction in coherent estimation.

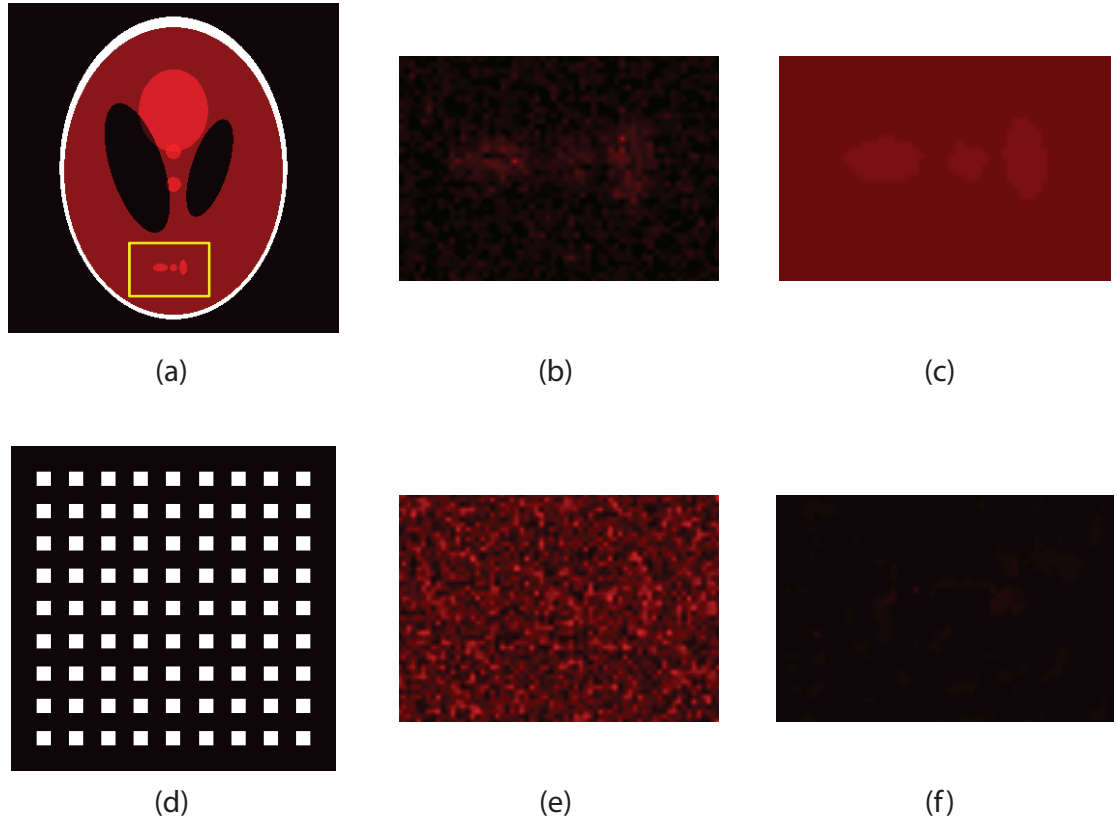


FIGURE 5.14: Patch-based sparse aperture holography : (a) 2D object, (b) region of interest of backpropagated field in coherent estimation, (c) region of interest of compressive reconstruction in coherent estimation, (d) sparse aperture with 16 percent fill factor, (e) region of interest of backpropagated field in incoherent estimation, and (f) region of interest of compressive reconstruction in coherent estimation.

# 6

## Conclusions

Compressive holography has successfully demonstrated holographic tomography and sparse aperture holography as examples of high performance imaging. Throughout the dissertation, the underlying message is a design methodology of the high performance imaging system. The computational and optical co-design enables high dimensional imaging problems, tomographic imaging and high pixel count imaging, tractable. Computational imaging develops a discrete mathematical model to represent the optical measurement process, which is called forward modeling. The forward model should efficiently identifies what problem to be solved for successful outcome. Then computational process performs the image reconstruction using the forward model, which is called inverse problem solving. The co-design strategy not only develops the forward model, but continues adapting the optical system to the computational design. Since computational imaging demands high dimensional data processing, the optical design necessarily supports the computational reconstruction, transforming it into manageable problems.

The computational and optical co-design is understood as a multi-domain approach. Computational imaging conceptually projects the imaging problem into the

computational domain; however, the co-design strategy projects it into the joint computational and optical domain. The co-design optimizes the problem solution in the high dimensional design space so the system optimization can be effectively performed more than in the single domain. The projects of compressive holography clearly support this claim. In the practical perspective, the co-design approach can relax the computational and optical limits set by the conventional design. Therefore, we may achieve high performance imaging beyond the conventional limits. In the theoretical perspective, the approach is attractive because theoretical ideas can be implemented and verified by the co-design support.

## 6.1 Summary of Results

Chapter 2 introduced compressive holography in terms of digital holography and compressive sensing. The main objective of compressive holography was identified by the reconstruction of a large number of pixel data from a small number of pixel measurement. Due to the insufficient measurements, the reconstruction was an ill-posed inverse problem so sparsity priors in proper basis were applied to compensate the insufficiency.

Compressive holography demonstrated single-shot holographic tomography in Chapter 3. 3D datacube was reconstructed from 2D Gabor hologram by using the holographic system model and the TwIST algorithm. The TwIST algorithm imposed sparsity priors on the total variation of the object. In the project, any advanced optical design was avoided to show the computational potential of holographic tomography. Holographic tomography was also applied to microscopic imaging. Holographic tomography does not require multiple measurements for holographic field extraction and 3D datacube reconstruction, so compressive holography possibly demonstrated the lensless tomographic microscope of living samples. To implement the lensless microscope system, the bare FPA microscope was optically designed with the Gabor

geometry and the diverging source.

Holographic tomography was applied to 3D diffuse object imaging in Chapter 4. The field complexity of holographic imaging occurred in the diffuse object due to the speckle effect. The incoherent image estimation relaxed the field complexity, resulting in the sparse representation of the incoherent image. In the optical design, the fully-developed speckle realization supported the computational design of the incoherent image estimation.

High pixel count holography was the other main project in Chapter 5. Scanning-based synthetic aperture holography was approached by the hierarchical estimation strategy. The computational and optical co-design supported the error estimation by locally dividing the estimation process. Sparse aperture holography was also introduced as an alternative method using compressive holography. In the simulation, compressive holography reconstructed the high resolution and wide FOV 2D image from the sparsely sampled 2D hologram. The incoherent image estimation compensated the insufficient measurements by suppressing the speckle effects and by doubling the MTF support.

## 6.2 Future of Compressive Holography

The computational and optical designs were presented for compressive holography; however, the research is still open for exploration in the computational and optical domains. In the computational perspective, compressive holographic tomography can be improved by sparse basis study. Depending on the prior knowledge of imaging object, joint sparsity basis can be scrutinized for the effective decompressive estimation. For example, a 3D object can be smooth in the axial direction and complicated in the transverse direction. Then the joint sparsity basis can be composed of the curvelet basis [59] in the axial dimension and the TV basis in the transverse dimensions, instead of equally using TV basis in the 3D object space. In addition,

the TwIST algorithm can be replaced by the other non-linear estimator such as the dictionary algorithm [60]. The dictionary algorithm was studied for missing data recovery by using compressive sensing.

In the optical perspective, new designs for a high frequency field measurement can be considered. A multi-angle illumination system may enable single-shot holographic tomography to improve the field measurement by multiplexing the high frequency field bands with a single aperture. The multiplexed field bands may be numerically separated and decompressively contributed to the 3D reconstruction. A multi-wavelength illumination system can also be one method to achieve the high frequency field measurement in k-space. Spectrally sampled coherent illuminations may optically sample the field bands in the k-space. The sampled field bands are computationally designed to reconstruct the 3D datacube by decompressive inference.

# Appendix A

## Aliasing Analysis

We investigate the phase terms of spherical field  $R(u, v; z_r)$  and propagation kernel  $H(f_u, f_v; z_d)$  in the ASM (Eq. 2.4). The phase variation  $\delta\phi_R(u; z_r)$  of the spherical field  $R(u; z_r)$  is calculated at the smallest increment  $\delta u$

$$\delta\phi_R(u; z_r) = \frac{2\pi}{\lambda} \left\{ \sqrt{z_r^2 + (u + \delta u)^2} - \sqrt{z_r^2 + u^2} \right\} \quad (\text{A.1})$$

Using the binomial expansion with the condition that the distance  $z_r$  is larger than the aperture width  $u$ , the phase change is obtained as

$$\delta\phi_R(u; z_r) = \frac{2\pi}{\lambda} \left\{ \frac{2u\delta u + \delta u^2}{2z_r} \right\} = \frac{\pi}{\lambda z_r} 2u\delta u < \pi \quad (\text{A.2})$$

where the term  $\delta u^2$  is negligible in comparison to the other term  $2u\delta u$ . The failure in the inequality causes the aliasing problem, corrupting the phase information in the propagation process. The smallest increment  $\delta u$  is given by the FPA pixel pitch, for instance,  $4.4\mu m$  and the propagation distance  $z_r$  is, for instance, 2 m. The aperture width  $u$  is substituted by the half of the total hologram width, for instance,  $\Delta u/2 = 31.68mm$ , then the maximum phase variation is  $0.2\pi$  satisfying the inequality

condition.

The phase variation  $\delta\phi_H(f_u; z_d)$  of the angular spectrum  $H(u; z_d)$  is calculated at the smallest increment  $\delta f_u$

$$\delta\phi_H(f_u; z_d) = \frac{2\pi}{\lambda} z_d \left\{ \sqrt{1 - \lambda^2(f_u + \delta f_u)^2} - \sqrt{1 - \lambda^2 f_u^2} \right\} \quad (\text{A.3})$$

Using the binomial expansion with the condition that the term  $\lambda^2 f_u^2$  is less than 1, the phase change becomes

$$\delta\phi_H(f_u; z_d) = \frac{2\pi}{\lambda} z_d \lambda^2 \left\{ \frac{2f_u \delta f_u + \delta f_u^2}{2} \right\} = \pi z_d \lambda \frac{1}{\delta u} \frac{1}{\Delta u} < \pi \quad (\text{A.4})$$

where the term  $\delta f_u^2$  is negligible to the term  $2f_u \delta f_u$ . The aperture frequency  $f_u$  is substituted by  $1/2\delta u$  and the smallest increment  $\delta f_u$  is substituted by  $1/\Delta u$ . Then the maximum phase variation is  $4.5\pi$  causing the aliasing problem at the field edges.

In the FAM, we investigate two quadratic phase terms: the inside quadratic phase term is for the diffraction propagation and the outside quadratic phase term is for the global phase factor. The outside and the side quadratic phase terms show the same aliasing conditions with the angular spectrum  $H$  and the spherical field  $R$ , respectively. In conclusion, both the ASM and the FAM are equivalent in the binomial approximation. Considering the use of the binomial expansion in the ASM, the ASM can be suffered more aliasing than the FAM in imaging of far distance and wide FOV.

# Appendix B

## Resolution Analysis

The band volume is the support in the 3D Fourier space of scattering object for sampling the scattered field over a finite aperture [28]. In Fig. B.1, optical measurement is illustrated in the space domain and the k-space domain. The k-space is understood as Fourier transform of the image measured. The aperture size of detector determines the light collection angle  $\phi$ , which is also used for  $NA = n \sin\phi$  (where  $n$  is the refractive index of the medium). The angle  $\phi$  is preserved in the k-space as shown in Fig. B.1 (b). The measurement center  $O$  is obtained by  $k_0 = 2\pi/\lambda$  in the k-space (where  $\lambda$  is the illumination wavelength). The measurement arc is defined by the angle  $\phi$  resulting in the bandwidths of  $\Delta k_x$  and  $\Delta k_z$ . Then the transverse and the axial resolutions of the imaging system are derived by trigonometry,

$$\Delta_x = \frac{2\pi}{\Delta k_x} = \frac{2\pi}{2k_0 NA} = \frac{\lambda}{2NA} \quad (\text{B.1})$$

$$\Delta_z = \frac{2\pi}{\Delta k_z} = \frac{2\pi}{k_0 - k_0 \sqrt{1-NA^2}} = \frac{2\lambda}{NA^2}, \quad (\text{B.2})$$

where  $2\pi$  is used for the k-space analysis. The resolution and the bandwidth follow the reciprocal relationship between the space and the k-space domains. Note the accuracy of the derivation is limited by the binomial approximation.

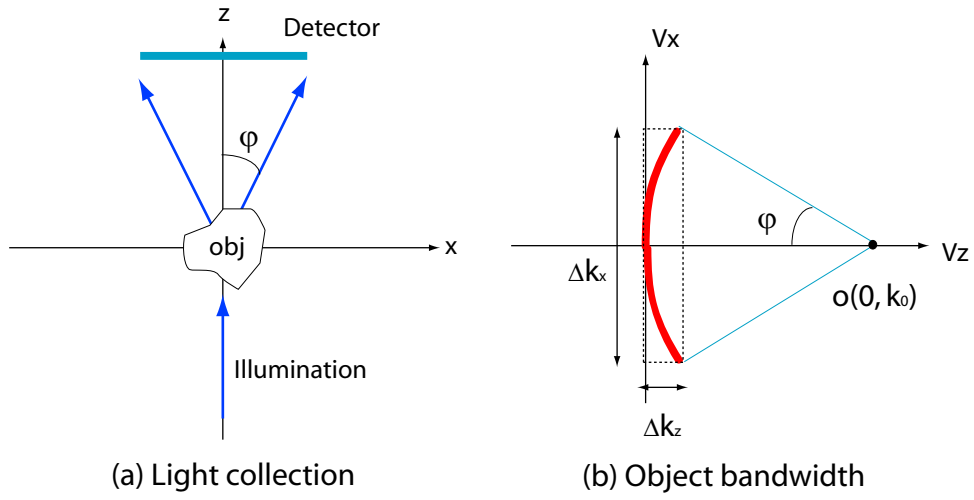


FIGURE B.1: Resolution and bandwidth: (a) light collection in space domain and (b) measured object bandwidth in Fourier domain.

# Appendix C

## Matlab Codes

The main command codes for the Matlab simulations are presented with simple comments. Note that the full simulation codes including the subfunctions are uploaded in the published journal paper (<http://www.opticsinfobase.org/abstract.cfm?uri=ao-50-34-H75>).

Listing C.1: Holographic Tomography

```
close all;
clear all;clc;
addpath( './ Functions' );

%% Paprameters (1)
% data size
nx=64;
ny=64;
nz=5;
% wavelength (um)
lambda=0.633;
% pixel pitch (um)
detector_size=30;
% detector size (um)
sensor_size=nx*detector_size;
% axial spacing (um)
```

```

deltaZ=20*1000;
% distance from detector to first plane (um)
offsetZ=0;
deltaX=detector_size;
deltaY=detector_size;
Nx=nx;
Ny=ny*nz*2;
Nz=1;

%% Object generation (2)
load( 'D48.mat' ); load( 'I48.mat' );
load( 'S48.mat' ); load( 'P48.mat' );
f=zeros( nx , ny , nz );
f (:,:,2)=0.7*D48;
f (:,:,3)=0.5*I48;
f (:,:,4)=1.0*S48;
f (:,:,5)=0.9*P48;
figure ; imagesc( plotdatacube( abs( f ) ) );
title( '3D_object' ); axis image; drawnow;
axis off; colormap( hot ); colorbar;

%% Propagation kernel (3)
[Phase3D_Pupil]=MyMakingPhase3D( nx , ny , nz , lambda , ...
    deltaX , deltaY , deltaZ , offsetZ , sensor_size );
figure ; imagesc( plotdatacube( angle( Phase3D ) ) );
title( 'Phase_of_kernel' ); axis image; drawnow;
axis off; colormap( hot ); colorbar;
% illumination light
E0=ones( nx , ny );
E0=E0.*exp( i .* pi * 0.0 );
% propagation of illumination light
E=MyFieldsPropagation( E0 , nx , ny , nz , Phase3D , Pupil );

%% Field measurement and backpropagation (4)
cEs=zeros( nx , ny , nz );
Es=f.*E;
for i=1:nz
    cEs (:,:, i )=fftshift( fft2( Es (:,:, i ) ) );
end
cEsp=sum( cEs .* Phase3D .* Pupil , 3 );
S=( ifft2( ifftshift( cEsp ) ) );

```

```

% squared field
s=S.*conj(S);
% diffracted field
g=S+f(:,:,2).^2+f(:,:,3).^2+f(:,:,4).^2+f(:,:,5).^2;
% g=S;
figure;imagesc(abs(g));title('Diffracted_field');
axis image; axis off; colormap(hot); colorbar;
g=MyC2V(g(:));
transf=MyAdjointOperatorPropagation...
(g,E,nx,ny,nz,Phase3D,Pupil);
transf=reshape(MyV2C(transf),nx,ny,nz);
figure;imagesc(plotdatacube(abs(transf)));
title('Numerical_backpropagation');axis image;drawnow;
axis off; colormap(hot); colorbar;

%% Propagation operator (5)
% forward propagation operator
A = @(f_twist) MyForwardOperatorPropagation...
(f_twist,E,nx,ny,nz,Phase3D,Pupil);
% backward propagation operator
AT = @(g) MyAdjointOperatorPropagation...
(g,E,nx,ny,nz,Phase3D,Pupil);

%% TwIST algorithm (6)
% twist parameters
tau = 0.01;
piter = 4;
tolA = 1e-6;
iterations = 500;

Psi = @(f,th) MyTVpsi(f,th,0.05,piter,Nx,Ny,Nz);
Phi = @(f) MyTVphi(f,Nx,Ny,Nz);

[f_reconstruct,dummy,obj_twist,...  

 times_twist,dummy,mse_twist]= ...  

 TwIST(g,A,tau,...  

 'AT', AT, ...  

 'Psi', Psi, ...  

 'Phi', Phi, ...  

 'Initialization',2,...  

 'Monotone',1,...  

 'StopCriterion',1,...
```

```
'MaxIterA',iterations ,...
'MinIterA',iterations ,...
'ToleranceA',tolA ,...
'Verbose', 1);

f_reconstruct=reshape(MyV2C(f_reconstruct),nx,ny,nz);
figure;imagesc(plotdatacube(abs(f_reconstruct)));
title('Compressive_reconstruction');axis image;drawnow;
axis off; colormap(hot); colorbar;
```

Listing C.2: Holographic Tomography of Diffuse Objects

```

close all;
clear all;clc;
addpath( './MyFunctions' );

rand( 'state' ,1);
randn( 'state' ,1);

%% Parameters (1)
% data size
nx=64;
ny=64*2;
nz=3;
% wavelength (um)
lambda=[0.633];
% detector pixel pitch (um)
detector_size=50;
% detector size (um)
sensor_size=nx*detector_size;
% distance from detector to first plane (um)
Z=[-50*1000,0,+50*1000];
deltaX=detector_size;
deltaY=detector_size;
mag=1;
ref_index=1;
NA=[lambda/(2*deltaX/mag),lambda/(2*deltaY/mag)];
% number of measurements
num_measure=30;
% Parameter for Tikhonov preconditioning
alpha=0.00001;

%% Object generation (2)
obj=zeros(nx,ny,nz)+0.1;
obj(5:60,32:42,1)=1;
obj(25:35,5:123,2)=1;
obj(5:60,96:106,3)=1;
figure;imagesc(plotdatacube(obj ,nz));axis image;
title (['Intensity_of_object']);drawnow;
axis off;colormap(hot);colorbar;

```

```

%% Propagation kernel (3)
nl=size(lambda,2);
E0=ones(nx,ny);
E0=E0.*exp(1i.*pi*1*ones(nx,ny));
[Phase3D Pupil]=MyMakingPhase3DMultiWaves(nx,ny, ...
    nz,nl,lambda,deltaX,deltaY,Z,NA,mag,ref_index);
figure;
imagesc(plotdatacube(angle(Phase3D.*1))); axis image;
title(['real(propagation_kernel)']);
E=MyFieldsPropagationMultiWaves...
    (E0,nx,ny,nz,nl,Phase3D,Pupil);
axis off; colormap hot; colorbar;

%% Propagation operators (4)
% Forward propagation
A=@(f_twist) MyForwardOperatorPropagationMulti...
    Waves(f_twist,E,nx,ny,nz,nl,Phase3D,Pupil);
% Backward propagation
AT=@(g) MyAdjointOperatorPropagationMulti...
    Waves(g,E,nx,ny,nz,nl,Phase3D,Pupil);

%% Holographic measurement, back-propagation,
%% and averaging (5)
average=zeros(nx*ny*nz,1);

for num=1:num_measure
    f_r=sqrt(obj/2).*randn(nx,ny,nz);
    f_i=sqrt(obj/2).*randn(nx,ny,nz);
    f=f_r+i.*f_i;
    G=reshape(MyV2C(A(MyC2V(f(:)))) ,nx,ny);
    average=average+(abs(MyV2C(AT(MyC2V(G(:)))))).^2;
    figure(99); imagesc(plotdatacube(reshape...
        (average./num,nx,ny,nz),nz));
    axis off; colormap hot; colorbar; drawnow;
    title(['number_of_realization : ',num2str(num)]);
end;
average=average./num_measure;

```

```

f_average=reshape( average(:, nx, ny, nz);

figure; imagesc( plotdatacube(f_average, nz)); axis image;
title([' Average_of_back-propagations_where_number... .
...of_realization_is_ ', num2str(num)]); drawnow;
axis off; colormap(hot); colorbar;
% break

%% Incoherent system matrix (6)
newH=@(delta) AT(A(delta));
Q=MyQ4DeblurringImageSpace(newH, nx, ny, nz);
[pinvQ combQ]=MyCombinedPinvQ4DeblurringImageSpace ...
(Q, alpha);

%% TwIST algorithm (7)
B=@(f_twist) MyFunc4DeblurringImageSpace(f_twist, Q);
C=@(f_twist) MyFunc4DeblurringImageSpace(f_twist, pinvQ);
D=@(f_twist) MyFunc4DeblurringImageSpace(f_twist, combQ);
DT=@(g) MyFunc4DeblurringImageSpace(g, conj(combQ));

tau = 1.5;
piter = 4;
tolA = 1e-6;
iterations = 500;

Psi = @(f, th) MyTVpsi(f, th, 0.05, piter, nx, ny, nz, [1 1 0]);
Phi = @(f) MyTVphi(f, nx, ny, nz, [1 1 0]);

invf=reshape(C(f_average(:)), nx, ny, nz);
figure; imagesc( plotdatacube(invF, nz));
axis image; colorbar;
title([' Tikhonov_inverse_of_averaged_backpropagations' ,...
' where_number_of_realizations_is_ ', num2str(num)]);
axis off; colormap(hot); colorbar;
drawnow;

[f_reconstruct, dummy, obj_twist, ...
times_twist, dummy, mse_twist] = ...
MyTwIST(C(f_average(:)), D, tau, nx, ny, nz, ...

```

```

'AT' , DT, ...
'Psi' , Psi , ...
'Phi' , Phi , ...
'Initialization' , 2 ,...
'Monotone' , 1 ,...
'StopCriterion' , 1 ,...
'MaxIterA' , iterations ,...
'MinIterA' , iterations ,...
'ToleranceA' , tolA ,...
'Verbose' , 1);

```

```

f_reconstruct=reshape( f_reconstruct , nx , ny , nz );
figure ; imagesc( plotdatacube( f_reconstruct , nz ) );
axis image;
title( { 'TwIST-reconstruction' , ...
'where_number_of_realizations_is' , num2str(num) } );
axis off; colormap( hot ); colorbar ;
drawnow;

```

Listing C.3: Sparse Aperture Holography - Coherent Image Estimation

```

close all;
clear all;clc;
addpath( './ Functions' );

% parameters (1)
% data size
nx=2048; ny=2048; nz=1;
% wavelength (um)
lambda=0.633;
% pixels pitch (um)
detector_size=25;
% detector size (um)
sensor_size=nx*detector_size;
% distance between each axial plane (um)
deltaZ=2000*1000;
% distance from detector to first plane (um)
offsetZ=deltaZ;
deltaX=detector_size;
deltaY=detector_size;
Nx=nx;
Ny=ny*nz*2;
Nz=1;

% Object generation (2)
obj=zeros(nx,ny,nz);
obj=phantom(length(obj));
figure; imagesc(plotdatacube(obj ,nz));
title('target-object'); axis image; drawnow;
axis off; colormap(hot); colorbar;

% Sparse aperture generation (3)
%random sparse aperture
sparse=randn(ny ,nx );
threshold=1.0; %1.1
sparse(sparse<threshold)=0;
sparse(sparse>=threshold)=1;
openning=sum(sparse (:)) / (ny*nx)*100;

```

```

figure(); imagesc(sparse); axis image;
title([ 'sparse_aperture--' , num2str(openning) ] );
axis off; colormap(hot); colorbar ;

%% Propagation operator (4)
% Forward propagation
A = @(f_twist) FresnelScalingAngularSpectrumFor ...
    ( f_twist , deltaX , nx , ny , offsetZ , lambda , sparse );
% Backward propagation
AT = @(g) FresnelScalingAngularSpectrumBack ...
    ( g , deltaX , nx , ny , offsetZ , lambda , sparse );

%% Holographic measurement, back-propagation,
%% and averaging (5)
num_measure = 30;
G_avg=0;

for num=1:num_measure
    f_r=sqrt(obj/2).*randn(nx,ny,nz);
    f_i=sqrt(obj/2).*randn(nx,ny,nz);
    f=f_r+i.*f_i;
    G=reshape(MyV2C(A(MyC2V(f(:)))) , nx , ny );
    G_avg=G_avg+G;
    figure(99); imagesc(plotdatacube ...
        (abs(G_avg) , nz )); axis image; colorbar;
    title([ 'number_of_realization:' , num2str(num) ] );
    drawnow;
end;
G_avg=G_avg./ num_measure;

g=MyC2V( G_avg (:));
transf=AT(g);
transf=reshape(MyV2C(transf) , nx , ny , nz );
figure; imagesc(plotdatacube(abs(transf) , nz ));
title( 'Numerical_backpropagation' ); axis image; drawnow;
axis off; colormap(hot); colorbar ;

```

```

%% TwIST algorithm (6)
tau = 0.01;
piter = 4;
tolA = 1e-6;
iterations = 500; %1000

Psi = @(f,th) MyTVpsi(f,th,0.05,piter,Nx,Ny,Nz);
Phi = @(f) MyTVphi(f,Nx,Ny,Nz);

[f_reconstruct,dummy,obj_twist,...  

 times_twist,dummy,mse_twist]= ...  

 TwIST(g,A,tau,...  

 'AT', AT, ...  

 'Psi', Psi, ...  

 'Phi', Phi, ...  

 'Initialization',2,...  

 'Monotone',1,...  

 'StopCriterion',1,...  

 'MaxIterA',iterations,...  

 'MinIterA',iterations,...  

 'ToleranceA',tolA,...  

 'Verbose', 1);

f_reconstruct=reshape(MyV2C(f_reconstruct),nx,ny,nz);
figure;imagesc(plotdatacube(abs(f_reconstruct),nz));
title('Compressive-reconstruction');axis image;drawnow;
axis off; colormap(hot); colorbar;

```

Listing C.4: Sparse Aperture Holography - Incoherent Image Estimation

```
close all;
clear all;clc;
addpath( './ MyFunctions' );
% break

rand('state',1);
randn('state',1);

%% Parameters (1)
nx=2048; ny=2048; nz=1;
% wavelength (um)
lambda=[0.633];
% pixels pitch (um)
detector_size=25;
% detector size (um)
sensor_size=nx*detector_size;
% distance from detector to first plane (um)
Z=[2000*1000];
deltaX=detector_size;
deltaY=detector_size;
% number of measurements
num_measure=30;
% Parameter for Tikhonov preconditioning
alpha=0.00001;

%% Object generation (2)
obj=zeros(nx,ny,nz)+0.1;
obj=phantom(length(obj));
figure; imagesc(plotdatacube(obj,nz)); axis image;
title(['Intensity_of_object']); drawnow;
axis off; colormap(hot); colorbar;

%% Sparse aperture generation (3)
%random sparse aperture
sparse=randn(nx,ny);
threshold=1.0;    %1.1 1.0
sparse(sparse
```

```

sparse(sparse>=threshold)=1;
openning=sum(sparse(:))/(ny*nx)*100;
figure(); imagesc(sparse); axis image;
title(['sparse_aperture = ', num2str(openning)]);
axis off; colormap(hot); colorbar;

%% Propagation operators (4)
% Forward propagation
A = @(f_twist) FresnelScalingAngularSpectrumFor...
    (f_twist, deltaX, nx, ny, Z, lambda, sparse);
% Backward propagation
AT = @(g) FresnelScalingAngularSpectrumBack...
    (g, deltaX, nx, ny, Z, lambda, sparse);

%% Holographic Measurement, back-propagation,
%% and averaging (5)
average=zeros(nx*ny*nz, 1);

for num=1:num_measure
    f_r=sqrt(obj/2).*randn(nx, ny, nz);
    f_i=sqrt(obj/2).*randn(nx, ny, nz);
    f=f_r+i.*f_i;
    G=reshape(MyV2C(A(MyC2V(f(:)))) , nx, ny);
    % G=G+r*(conj(G)+abs(G).^2);
    % G=awgn(G, snr, 'measured');
    average=average+(abs(MyV2C(AT(MyC2V(G(:)))))).^2;
    figure(99); imagesc(plotdatacube(reshape...
        (average./num, nx, ny, nz), nz));
    axis image; colorbar;
    title(['number_of_realization: ', num2str(num)]);
    drawnow;
end;
average=average./ num_measure;
f_average=reshape(average(:, nx, ny, nz));

figure; imagesc(plotdatacube(f_average, nz)); axis image;
title(['Average_of_back-propagations_where_number...
    _of_realization_is ', num2str(num)]); drawnow;

```

```

axis off; colormap (hot); colorbar;

%% Incoherent system matrix (6)
newH=@( delta ) AT(A(delta));
Q=MyQ4DeblurringImageSpace(newH,nx,ny,nz);
[pinvQ combQ]=MyCombinedPinvQ4DeblurringImage...
Space(Q, alpha);

%% TwIST algorithm (7)
B=@( f_twist ) MyFunc4DeblurringImageSpace ...
(f_twist ,Q);
C=@( f_twist ) MyFunc4DeblurringImageSpace ...
(f_twist ,pinvQ );
% forward projection
D=@( f_twist ) MyFunc4DeblurringImageSpace ...
(f_twist ,combQ);
% backward projection
DT=@(g) MyFunc4DeblurringImageSpace ...
(g,permute( conj(combQ) ,[1 2 4 3]));

tau = 0.4; %0.2
piter = 4;
tolA = 1e-6;
iterations = 500;

Psi = @(f ,th) MyTVpsi(f ,th ,0.05 ,piter ,nx ,ny ,nz ,...
[1 1 0]);
Phi = @(f) MyTVphi(f ,nx ,ny ,nz ,[1 1 0]);

[f_reconstruct ,dummy,obj_twist ,...
times_twist ,dummy,mse_twist]= ...
MyTwIST(C( f_average (:)) ,D,tau ,nx ,ny ,nz ,...
'AT' , DT, ...
'Psi' , Psi , ...
'Phi' ,Phi , ...
'Initialization' ,2 ,...
'Monotone' ,1 ,...
'StopCriterion' ,1 ,...

```

```
'MaxIterA',iterations,...  
'MinIterA',iterations,...  
'ToleranceA',tolA,...  
'Verbose', 1);  
  
f_reconstruct=reshape(f_reconstruct ,nx ,ny ,nz );  
figure;imagesc(plotdatacube(f_reconstruct ,nz ));  
title({'TwIST-reconstruction',...  
'where number of realizations is ', num2str(num)});  
axis off;colormap(hot);colorbar;axis image;  
drawnow;
```

# Bibliography

- [1] E. N. Leith and J. Upatnieks, “Reconstructed wavefronts and communication theory,” *J. Opt. Soc. Am.* **52**, 1123–1130 (1962).
- [2] W. Jueptner and U. Schnars, *Digital Holography* (Springer-Verlag, New York, Berlin Heidelberg, 2005).
- [3] D. Gabor, “A new microscopic principle,” *Nature* **161**, 777–778 (1948).
- [4] J. W. Goodman, *Introduction to Fourier optics, 3rd Ed.* (Roberts and Company Publishers, New York, 2005).
- [5] E. J. Candes, J. K. Romberg, and T. Tao, “Stable signal recovery from incomplete and inaccurate measurements,” *Communications on Pure and Applied Mathematics* **59**(8), 1207–1223 (2006).
- [6] D. L. Donoho, “Compressed sensing,” *IEEE Transactions on Information Theory* **52**(4), 1289–1306 (2006).
- [7] M. A. Neifeld and P. Shankar, “Feature-specific imaging,” *Applied Optics* **42**(17), 3379–3389 (2003).
- [8] D. J. Brady, N. Pitsianis, X. Sun, and P. Potuluri, “Compressive sampling and signal inference, US patents,” (2005).
- [9] X. Zhang, E. Y. Lam, and T.-C. Poon, “Reconstruction of sectional images in holography using inverse imaging,” *OPTICS EXPRESS* **16**(22), 17,215–17,226 (2008).
- [10] X. Zhang and E. Y. Lam, “Edge-preserving sectional image reconstruction in optical scanning holography,” *JOURNAL OF THE OPTICAL SOCIETY OF AMERICA A-OPTICS IMAGE SCIENCE AND VISION* **27**(7), 1630–1637 (2010).

- [11] D. J. Brady, K. Choi, D. L. Marks, R. Horisaki, and S. Lim, “Compressive Holography,” *Opt. Express* **17**(15), 13,040–13,049 (2009).
- [12] J. Hahn, S. Lim, K. Choi, R. Horisaki, and D. J. Brady, “Video-rate compressive holographic microscopic tomography,” *Opt. Express* **19**(8), 7289–7298 (2011).
- [13] C. F. Cull, D. A. Wikner, J. N. Mait, M. Mattheiss, and D. J. Brady, “Millimeter-wave compressive holography,” *Appl. Opt.* **49**(19), E67–E82 (2010).
- [14] K. Choi, R. Horisaki, J. Hahn, S. Lim, D. L. Marks, T. J. Schulz, and D. J. Brady, “Compressive holography of diffuse objects,” *Appl. Opt.* **49**(34), H1–H10 (2010).
- [15] L. Denis, D. Lorenz, E. Thiébaut, C. Fournier, and D. Trede, “Inline hologram reconstruction with sparsity constraints,” *Opt. Lett.* **34**(22), 3475–3477 (2009).
- [16] C. Fournier, L. Denis, and T. Fournel, “On the single point resolution of on-axis digital holography,” *J. Opt. Soc. Am. A* **27**(8), 1856–1862 (2010).
- [17] M. M. Marim, M. Atlan, E. Angelini, and J.-C. Olivo-Marin, “Compressed sensing with off-axis frequency-shifting holography,” *Opt. Lett.* **35**, 871–873 (2010).
- [18] M. Marim, E. Angelini, J.-C. Olivo-Marin, and M. Atlan, “Off-axis compressed holographic microscopy in low-light conditions,” *OPTICS LETTERS* **36**(1), 79–81 (2011).
- [19] Y. Rivenson, A. Stern, and B. Javidi, “Compressive Fresnel Holography,” *J. Display Technol.* **6**, 506–509 (2010).
- [20] Y. Rivenson, A. Stern, and J. Rosen, “Compressive multiple view projection incoherent holography,” *Opt. Express* **19**, 6109–6118 (2011).
- [21] Q. Xu, K. Shi, H. Li, K. Choi, R. Horisaki, D. Brady, D. Psaltis, and Z. Liu, “In-line holographic coherent anti-Stokes Raman microscopy,” *OPTICS EXPRESS* **18**(8), 8213–8219 (2010).
- [22] Z. Xu and E. Y. Lam, “Image reconstruction using spectroscopic and hyper-spectral information for compressive terahertz imaging,” *JOURNAL OF THE OPTICAL SOCIETY OF AMERICA A-OPTICS IMAGE SCIENCE AND VISION* **27**(7), 1638–1646 (2010).

- [23] A. F. Coskun, I. Sencan, T.-W. Su, and A. Ozcan, “Lensless wide-field fluorescent imaging on a chip using compressive decoding of sparse objects,” *OPTICS EXPRESS* **18**(10), 10,510–10,523 (2010).
- [24] M. Suezen, A. Giannoula, and T. Durduran, “Compressed sensing in diffuse optical tomography,” *OPTICS EXPRESS* **18**(23), 23,676–23,690 (2010).
- [25] E. J. Candes and M. B. Wakin, “An Introduction To Compressive Sampling,” *IEEE SIGNAL PROCESSING MAGAZINE* pp. 21–30 (March 2008).
- [26] U. Schnars and W. Juptner, *Digital Holography, Digital Hologram Recording, Numerical Reconstruction and Related Techniques* (Springer, 2005).
- [27] U. Schnars and W. P. O. Juptner, “Digital recording and numerical reconstruction of holograms,” *Meas. Sci. Technol.* **13**, R85–R101 (2002).
- [28] D. J. Brady, *Optical Imaging and Spectroscopy* (Wiley, 2009).
- [29] T. Kreis, M. Adams, and W. Juptner, “Methods of digital holography: A comparison,” vol. 3098 of *PROCEEDINGS OF THE SOCIETY OF PHOTONICAL INSTRUMENTATION ENGINEERS (SPIE)*, pp. 224–233 (1997).
- [30] W. U. Z. Bajwa, “New Information Processing Theory and Methods for Exploiting Sparsity in Wireless Systems,” Ph.D. thesis, University of WisconsinMadison (2009).
- [31] A. J. Devaney, “Nonuniqueness in the inverse scattering problem,” *Journal of Mathematical Physics* **19**(7), 15261531 (1978).
- [32] A. J. Devaney, “Geophysical diffraction tomography,” *IEEE Transactions on Geoscience and Remote Sensing GE* **22**, 3–13 (1984).
- [33] L. RUDIN, S. OSHER, and E. FATEMI, “NONLINEAR TOTAL VARIATION BASED NOISE REMOVAL ALGORITHMS,” *PHYSICA D* **60**(1-4), 259–268 (1992).
- [34] J. M. Bioucas-Dias and M. A. T. Figueiredo, “A new twist: Two-step iterative shrinkage/thresholding algorithms for image restoration,” *IEEE Transactions on Image Processing* **16**, 29923004 (2007).
- [35] S. Lim, D. L. Marks, and D. J. Brady, “Sampling and processing for compressive holography [Invited],” *Appl. Opt.* **50**(34), H75–H86 (2011).

- [36] J. Garcia-Sucerquia, W. Xu, S. K.Jericho, P. Klages, M. H. Jericho, and J. Kreuzer, “Digital in-line holographic microscopy,” *Appl. Opt.* **45**, 836–850 (2006).
- [37] D. P. Kelly, B. M. Hennelly, N. Pandey, T. J. Naughton, and W. T. Rhodes, “Resolution limits in practical digital holographic systems,” *Opt. Eng.* **48**, 095,801–13 (2009).
- [38] A. C. Kak and M. Slaney, *Principle of Computerized Tomographic Imaging* (Society for Industrial and Applied Mathematics, 2001).
- [39] D. L. Marks, “A family of approximations spanning the Born and Rytov scattering series,” *Opt. Express* **14**, 8837–8848 (2006).
- [40] J. Chae and S. Nishida, “Integumental ultrastructure and colour patterns in the iridescent copepods of the family Sapphirinidae (Copepoda: Poecilostomatoida),” *Marine Biology* **119**, 205–210 (1994).
- [41] J. W. Goodman, *Statistical Optics* (Wiley Inter-Science, 2000).
- [42] T. K. Moon and W. C. Stirling, *Mathematical Methods and Algorithms for Signal Processing* (Prentice-Hall, 2000).
- [43] J. Tropp, “Just relax: Convex programming methods for identifying sparse signals in noise,” *IEEE TRANSACTIONS ON INFORMATION THEORY* **52**(3), 1030–1051 (2006).
- [44] T. Schulz, “Penalized maximum-likelihood estimation of covariance matrices with linear structure,” *IEEE Transactions on Signal Processing* **45**(12), 30273038 (1997).
- [45] J. W. Goodman, *Speckle Phenomena in Optics - Theory and Applications* (Roberts and Company, 2007).
- [46] C. W. Sherwin, P. Ruina, and R. D. Rawcliffe, “Some early developments in synthetic aperture radar systems,” *IRE Trans. Mil. Electron.* **6**, 111115 (1962).
- [47] L. G. Brown, “A survey of image registration techniques,” *ACM Computing Surveys (CSUR)* **24**, 4 (1992).
- [48] L. Romero and F. Calderon, *A Tutorial on Parametric Image Registration* (I-Tech, 2007).

- [49] J. H. Massig, “Digital off-axis holography with a synthetic aperture,” Opt. Lett. **27**(24), 2179–2181 (2002).
- [50] R. Binet, J. Colineau, and J.-C. Lehureau, “Short-Range Synthetic Aperture Imaging at 633 nm by Digital Holography,” Appl. Opt. **41**(23), 4775–4782 (2002).
- [51] J. R. Fienup and J. J. Miller, “Aberration correction by maximizing generalized sharpness metrics,” J. Opt. Soc. Am. A **20**, 609–620 (2003).
- [52] V. Mico, Z. Zalevsky, P. García-Martínez, and J. García, “Synthetic aperture superresolution with multiple off-axis holograms,” J. Opt. Soc. Am. A **23**(12), 3162–3170 (2006).
- [53] H. Jiang, J. Zhao, J. Di, and C. Qin, “Numerically correcting the joint misplacement of the sub-holograms in spatial synthetic aperture digital Fresnel holography,” Opt. Express **17**(21), 18,836–18,842 (2009).
- [54] B. Javidi, P. Ferraro, S.-H. Hong, S. D. Nicola, A. Finizio, D. Alfieri, and G. Pierattini, “Three-dimensional image fusion by use of multiwavelength digital holography,” Opt. Lett. **30**(2), 144–146 (2005).
- [55] S. T. Thurman and J. R. Fienup, “Phase-error correction in digital holography,” J. Opt. Soc. Am. A **25**, 983–994 (2008).
- [56] A. Kozmat and C. R. Christensen, “Effects of speckle on resolution,” J. Opt. Soc. Am. **66**, 1257–1260 (1976).
- [57] S. Lim, K. Choi, J. Hahn, D. L. Marks, and D. J. Brady, “Image-based registration for synthetic aperture holography,” Opt. Express **19**(12), 11,716–11,731 (2011).
- [58] A. R. Thompson, J. M. Moran, and J. G. W. Swenson, *Interferometry and Synthesis in Radio Astronomy* (Wiley, 2001).
- [59] E. J. Cands and D. L. Donoho, “New tight frames of curvelets and optimal representations of objects with piecewise  $C^2$  singularities,” COMM. ON PURE AND APPL. MATH pp. 219–266 (2002).
- [60] M. Zhou, H. Chen, J. W. Paisley, L. Ren, L. Li, Z. Xing, D. B. Dunson, G. Sapiro, and L. Carin, “Nonparametric Bayesian Dictionary Learning for Analysis of Noisy and Incomplete Images.” IEEE Transactions on Image Processing **21**(1), 130–144 (2012).

# Biography

Se Hoon Lim was born in Seoul, South Korea on December 5, 1978. He attended Yonsei University at Seoul, majoring in the Electrical and Computer Engineering and was a Department Scholar for three semesters. He graduated in 2005 with a Bachelors degree in Electrical and Computer Engineering. His undergraduate thesis was titled by “RGB Photodiodes for CMOS Image Sensor Applications” under Dr. Ilgu Yoon. In the spring of 2005, he took a part-time job in developing an electrical analysis tool for Quantum dots laser with HP4284a under Dr. Won Jun Choi at Korea Institute of Science and Technology. In the fall, Se Hoon came over to the University of Arizona for a Masters degree. He was a research assistant in the Photonic Systems Lab under Dr. Raymond K. Kostuk. His masters thesis was “Field-of-View(FOV) Extender for a Thin Camera System”, which was involved in the Montage project.

In 2007, Se Hoon enrolled in the PhD program in electrical and computer engineering at Duke University. Upon admission, He was offered two fellowships such as Electrical Engineering 1st year fellowship and John T. Chambers fellowship. There he became a member of the Duke Imaging and Spectroscopy Program (DISP) led by Dr. David Brady. He was active in the Optical Society of America (OSA), serving as a journal reviewer. In 2009, he was the 3rd winner of Fitzpatrick Institute of Photonics 9th Annual Meeting Poster Session. Se Hoon will receive his PhD in May 2012.

## Publications

1. **Sehoon Lim**, Daniel L. Marks, and David J. Brady, “*Sampling and processing for compressive holography [Invited]*,” Appl. Opt. 50, H75-H86 (2011).
2. Joonku Hahn, Daniel L. Marks, Kerkil Choi, **Sehoon Lim**, and David J. Brady, “*Thin holographic camera with integrated reference distribution*,” Appl. Opt. 50, 4848-4854 (2011).
3. **Sehoon Lim**, Kerkil Choi, Joonku Hahn, Daniel L. Marks, and David J. Brady, “*Image-based registration for synthetic aperture holography*,” Opt. Express 19, 11716-11731 (2011) .
4. Joonku Hahn, **Sehoon Lim**, Kerkil Choi, Ryoichi Horisaki, and David J. Brady, “*Video-rate compressive holographic microscopic tomography*,” Opt. Express 19, 7289-7298 (2011).
5. Kerkil Choi, Ryoichi Horisaki, Joonku Hahn, **Sehoon Lim**, Daniel L. Marks, Timothy J. Schulz, and David J. Brady, “*Compressive holography of diffuse objects*,” Applied Optics, Vol. 49, Issue 34, pp. H1-H10 (2010).
6. David J. Brady, Kerkil Choi, Daniel L. Marks, Ryoichi Horisaki, and **Sehoon Lim**, “*Compressive holography*,” Opt. Express 17, 13040-13049 (2009).
7. **Sehoon Lim**, and Raymond K. Kostuk, “*Field-of-View extender for a novel camera system*,” In Practical Holography XXI: Materials and Applications, Proc. of SPIE Vol. 6488 in San Jose, CA (2007).

## Conference Presentations

1. “*Sparse Aperture Holography*,” at OSA FIO Meeting in San Jose, CA (2011).
2. “*High Pixel Count Holography*,” at OSA COSI Meeting in Toronto, Canada (2011).

3. “*Experimental Demonstrations of Compressive Holography*,” at OSA Annual Meeting in San Jose, CA (2009).
4. “*Compressive Holography*,” at Duke University FIP Symposium on Frontiers in Photonics, Science and Technology in Durham, NC (2009).
5. “*High-throughput, multiplex aperture-coded Raman spectroscopy for biomedical diagnostics*,” at OSA Spring Optics and Photonics Congress on BIOMED in St. Petersburg, FL (2008).
6. “*Field-of-View extender for a novel camera system*,” In Practical Holography XXI: Materials and Applications, Proc. of SPIE Vol. 6488 in San Jose, CA (2007).